

UNDERSTANDING NON-PRECIOUS METAL CATALYSTS  
FOR THE OXYGEN REDUCTION REACTION  
AND INVESTIGATING CORROSION AND SURFACE PROPERTIES  
OF CARBON-DOPED ALUMINUM ALLOYS

BY

JASON A. VARNELL

DISSERTATION

Submitted in partial fulfillment of the requirements  
for the degree of Doctor of Philosophy in Chemistry  
in the Graduate College of the  
University of Illinois at Urbana-Champaign, 2018

Urbana, Illinois

Doctoral Committee:

Professor Andrew A. Gewirth, Chair  
Professor Catherine J. Murphy  
Professor Kenneth S. Suslick  
Assistant Professor Joaquín Rodríguez-López

## Abstract

The development of sustainable technologies to address the increasing global energy demand, to enable new ways to conserve energy, and to reduce the environmental impact of energy production and consumption is highly desirable. In many cases, a fundamental understanding is crucial for the discovery and improvement of such technologies. In particular, fundamental studies involving electrocatalysis and corrosion can offer promising solutions to some of the most difficult challenges. The first chapter introduces each of these strategies in more detail. The next three chapters of this thesis describe efforts undertaken to understand the active species within non-precious metal catalysts for potential future applications in fuel cells as a replacement for the more costly Pt-based catalysts used today. The final chapter reports on the electrochemical properties of a new type of Al alloy into which carbon has been added via a new processing method. Together, these studies provide important direction for further research and development of sustainable technologies.

Due to the decreasing supply and environmental impact of fossil fuels as a source of energy, the development and utilization of fuel cells as energy conversion devices has increased recently due to their higher theoretical efficiency and lack of harmful byproducts. An additional benefit of fuel cells is that the fuel itself can be generated from renewable energy sources such as wind and solar and stored or transported wherever and whenever it is needed. Despite these desirable features, the efficiency of a fuel cell remains relatively low due to the slow kinetics of the oxygen reduction reaction (ORR). Currently, Pt-based catalysts are used to facilitate the ORR in fuel cells but they are expensive and are still far from reaching the maximum theoretical

efficiency. As a result, significant effort has been given to develop non-precious metal (NPM) catalysts over the past several decades.

Chapter 2 and Chapter 3 describe new methods to clarify the identity of the active species in Fe-based NPM ORR catalysts. In my work gas-phase  $\text{Cl}_2$  and  $\text{H}_2$  treatments are used to alter the Fe species in a NPM catalyst and solution-based treatments with  $\text{H}_2\text{SO}_4$  and  $\text{H}_2\text{O}_2$  are used to remove metal species from the material. Through the use of electrochemical methods, the activity and selectivity of these catalysts before and after treatment is determined and compared. Additionally, surface and bulk characterization using several different methods reveals the catalyst's structure and the chemical species present. These studies show that metallic Fe nanoparticles encapsulated in N-doped carbon are the locus of ORR activity in NPM catalysts.

Chapter 4 describes a mechanistic study utilizing the kinetic isotope effect (KIE) to compare the ORR pathway on NPM catalysts with precious metal catalysts Pt and Pd. The use of KIE in this case is able to provide information on the role of protons ( $\text{H}^+$ ) in the ORR mechanism. This study indicates that there is a KIE observed for a NPM catalyst but a KIE is not observed for Pt or Pd. These findings suggest that NPM catalysts operate via a different pathway than precious metal ones, providing guidance for future catalyst design.

Another method to reduce the use of fossil fuels for transportation is the utilization of Al as a light-weight building material. Currently, Al is protected from corrosion using chromate conversion coating in which the Al parts are treated in chromic acid solutions to create a passivation layer. However, chromic acid is highly toxic and alternative strategies for corrosion protection are needed. One potential solution is the formation of "covetic" Al alloys by adding carbon to molten Al and applying a high voltage and current to the mixture. Previous work has demonstrated an improvement in the mechanical properties of covetics prepared via this process.

Chapter 5 describes an electrochemical investigation of Al coveitics relating to their corrosion and surface properties. Electrochemical methods are used to understand the corrosion potential and rate of corrosion on several materials and surface characterization is performed to interrogate the surface properties. These studies reveal that the corrosion potential of the covetic is shifted to higher potential, which is explained by significant differences in the surface structure of the covetic as compared to the parent material. Specifically, changes in grain size and chemical species on the surface of the covetic material contribute to its corrosion behavior.



## Acknowledgements

First and foremost, I would like to thank my advisor, Professor Andy Gewirth. I am grateful for his continued support throughout graduate school and for the positive atmosphere I experienced as a member of his research group. His high expectations and attention to detail, as well as his humor and encouragement, played a crucial role in my development as a scientist and as a person. I would also like to thank my thesis committee members for their support: Professor Catherine Murphy, Professor Thomas Rauchfuss, Professor Kenneth Suslick, and Professor Joaquín Rodríguez-López. Their contributions to my research through thoughtful discussions, constructive questions, and opportunities to collaborate helped enrich my experience while a member of the Chemistry department at UIUC.

I would also like to thank several collaborators without whose efforts and input my work would have not been possible. Professor Chuck Schulz was kind enough to measure countless Mössbauer spectra of the various samples I prepared. Dr. Tim Fister measured X-ray spectra for some of the same samples and assisted in the exploration of new experiments conducted at the beamline. Professor Anatoly Frenkel and Dr. Janis Timoshenko helped analyze and make sense of the X-ray spectra that we collected. Dr. Rick Haasch measured the XPS spectra of numerous samples and allowed me to assist and learn in the process. Dr. Kiran Subedi analyzed and re-analyzed many ICP samples and worked closely with me to improve the results. I was also fortunate to have the chance to collaborate with Mete Bakir and Professor Iwona Jasiuk who reached out to us for help studying and understanding “covetics”. This gave me the chance to explore a new area of materials science outside of my previous research focus. I am grateful for all of the time these collaborators spent with me on my various projects.

I would also like to thank all of the members of the Gewirth Group who overlapped with me during my time in graduate school. In particular, Edmund Tse who was my mentor and close collaborator during my early years in the group. The knowledge and experience that he passed on to me and his enthusiastic willingness to help were crucial in the early-going of my projects. I greatly enjoyed all of the time we spent working together from even the most tedious of experiments to the more exciting and adventurous ones as well as the many scientific and non-scientific discussions that we had along the way. I would like to thank Angie DiAscro for all of the adventures and discussions that we had in graduate school as well. I was fortunate to have the chance to mentor two undergraduate students, Jimmy Sotiropoulos and Therese Brown, whose scientific contributions and fun, easy-going personalities made it a pleasure to work with them in the lab. Additionally, I would like to thank the following list of Gewirth Group members for helping make my graduate school experience extremely rewarding: Chris Barile, Elizabeth Barile, Adele Pacquette, Justin Oberst, Jen Esbenshade, Kevin Schmitt, Thao Hoang, Yeyoung Ha, Owen Liu, Bruno Nicolau, Kimberly Bassett, MJ Shin, Ryan Rooney, Kim Ta, Yeong-Hui Seo, Maria Philip, Ruixian Zhang, Stephanie Chen, Teng Zhang, Heng-Liang Wu, Kim See, Lingzi Sang, Annie Esposito, Chris Bandas-Rivera, and Ken Madsen.

Many other people also impacted me on my journey. I would especially like to thank my housemates from the “Vine House” for their support and friendship during our time together in graduate school: Evi Llabani, Keong Yong, Rob Hicklin, Jake Hicklin, Jonathan Eller, Adam DiCaprio, and Matt Kottwitz. Through our cookouts, dinners, TV nights, Super Bowl parties, road trips, and other escapades they provided the fun and excitement that made my time in Champaign-Urbana even more memorable and enjoyable. I am also grateful for all of the other friends that I made during graduate school and for the good times we had together.

I greatly appreciate my colleagues in the Chemistry department who provided opportunities for me to think about other scientific challenges or to work on other research projects outside of my main area expertise and to enjoy the process of learning along the way. I would also like to thank my undergraduate research advisor Professor David Weitz at Harvard University for allowing to join his lab to begin my research career and Anderson Shum who served as my mentor while he was a graduate student there. I would like to thank Dr. Tushar Bera who served as my advisor during a research internship at Infineum, USA and who has continued to be supportive of me during graduate school and as I move forward in my career.

Finally, I would like to express my eternal gratitude to my family who has supported me in graduate school and throughout my life, in all of my endeavors. Especially my parents, Bill and Debbie, without whom I would not be who, or where, I am today. From an early age they encouraged me to excel and pursue my passions and they provided me with every opportunity that they could to do so along the way. My dad made science a part of my life at home and in school and for as long as I can remember I wanted to pursue a PhD in Chemistry just like he had done many years before. I am also grateful for the support of my brother, Brian, and sister, Kelly, both of whom are also currently pursuing education or careers involving science and chemistry to varying degrees.

*~To my colleagues, friends, and family who have supported me along the way, and especially to my father who inspired me to become a chemist, I am forever grateful~*

## Table of Contents

Chapter 1:	Introduction: The Development of Sustainable Technologies.....	1
Chapter 2:	Identification of Carbon-Encapsulated Iron Nanoparticles as Active Species in Non-Precious Metal Oxygen Reduction Catalysts .....	11
Chapter 3:	Revealing the Role of the Metal in Non-Precious Metal Catalysts for Oxygen Reduction via Selective Removal of Fe .....	68
Chapter 4:	Elucidating Proton Involvement in the Rate-Determining Step for Pt/Pd-Based and Non-Precious Metal Oxygen Reduction Reaction Catalysts Using the Kinetic Isotope Effect.....	93
Chapter 5:	Investigating the Corrosion Behavior and Mechanical Properties of Al-Alloy “Covetics” .....	124

## Chapter 1

### Introduction: The Development of Sustainable Technologies

#### 1.1 The Changing Energy Landscape

In recent decades, the energy demand in the U.S. and world-wide has increased rapidly. To meet this growing demand, fossil fuels continue to be the main source of the energy that is produced. In 2017 global CO<sub>2</sub> emissions continued to increase to historically high levels.<sup>1</sup> In some countries such as the U.S. there has been a general decrease in the amount of energy produced from coal in favor of cleaner sources, such as natural gas. Additionally, the use of renewable energy sources- hydroelectric, geothermal, solar, wind, and biomass- accounted for more than 10% of the energy produced in the U.S in 2017 continuing a trend towards a larger reliance on clean and renewable energy.<sup>2</sup> Despite these efforts to utilize renewable energy technologies in order to lessen our global reliance on fossil fuels, many challenges remain in developing and improving new technologies to make a significant impact.<sup>3</sup> In order for emerging technologies to be viable, they must become cost-competitive with traditional sources of energy. Additionally, the intermittent nature of energy sources such as hydro, wind, and solar requires the development of strategies to distribute and store energy as it is produced. Due to the challenges associated with altering energy production, methods to decrease energy demand by increasing the efficiency of energy consumption are also receiving significant attention. Together, the development of cleaner energy sources to replace fossil fuels as well as efforts to conserve energy via higher efficiency can help us ensure that the global energy demand is met and that CO<sub>2</sub> emissions associated with fossil fuels can be reduced in the future.

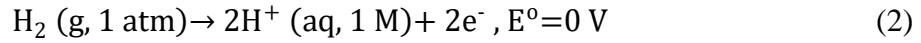
## 1.2 Fuel Cells and the Importance of Oxygen Reduction Reaction Electrocatalysis

As energy is produced and consumed it is often converted from one form to another. These transformations are necessary in many cases where the energy needs to be stored or transported before it is consumed. A common energy conversion device is the internal combustion engine which converts chemical energy into mechanical energy as gasoline is burned to drive the pistons in the engine and power a vehicle. However, the efficiency of a combustion engine is severely limited by the Carnot cycle. Using H<sub>2</sub> as the fuel source, an internal combustion engine achieves a thermodynamic efficiency of only 10-20%.<sup>4</sup> Fuel cells are another type of energy conversion device which offer a much higher theoretical efficiency greater than 90%.<sup>5,6</sup> However, different types of fuel cells suffer from other challenges that limit their application. Solid oxide fuel cells are operated at high temperature where durability remains an issue. Low-temperature fuel cells such as polymer electrolyte membrane (PEM), alkaline, and direct methanol operate near room temperature but are subject to slow kinetics and poisoning over time. Due to a combination of these issues, the actual efficiency of a fuel cell is well below the theoretical value, typically around 40-50%.<sup>7</sup>

The efficiency of a fuel cell is partially determined by the efficiency of the individual electrochemical reactions occurring at the electrodes. In order to facilitate these reactions, energy input in the form of electrochemical overpotentials detracts from the overall efficiency of the system. The efficiency can be determined by Equation 1 where  $\eta_{\text{anode}}$  is the overpotential at the anode,  $\eta_{\text{cathode}}$  is the overpotential at the cathode, and  $\Delta E^0$  is the difference between the formal potentials of the reactions at the anode and cathode.

$$\zeta = 1 - \frac{\eta_{\text{anode}} + \eta_{\text{cathode}}}{\Delta E^0} \quad (1)$$

In a typical PEM FC utilizing H<sub>2</sub> as a fuel source (**Fig. 1.1**), the reactions occurring on the anode and cathode are the hydrogen oxidation reaction (HOR, Eq. 1) and the oxygen reduction reaction (ORR, Eq. 2) respectively.



The overpotential for the HOR ( $\eta_{\text{anode}}$ ) is typically small for commercial catalysts and therefore plays a minor role in decreasing the efficiency of an operating fuel cell. On the other hand, the overpotential for the ORR ( $\eta_{\text{cathode}}$ ) in a fuel cell is between 0.3 and 0.6 V which greatly lowers the efficiency from the theoretical values above 90% to the values below 50% which are typically observed.

The large overpotential for the ORR observed for the existing catalysts results from the slow kinetics associated with breaking the strong O=O double bond (498 kJ/mol).<sup>7</sup> Even with the best Pt-based catalysts a significant overpotential remains along with the issues of relatively high Pt-loading and catalyst durability.<sup>8,9</sup> Due to these issues, as well as the cost of Pt-based catalysts, substantial effort has been devoted to finding viable alternatives. In nature, examples of ORR catalysts involving Fe and Cu are common. Cytochrome C oxidase, a transmembrane protein found in the mitochondria, and the family of multi-copper oxidases, especially laccase, are able to facilitate the ORR with a low overpotential utilizing sites involving multiple Fe and/or Cu atoms. Therefore, these natural systems are widely used as inspiration for the development of non-precious metal (NPM) catalysts that are able to reduce oxygen at low overpotential.<sup>7,10-12</sup> While efforts to utilize Cu as a catalyst have been met with limited success,



the development of Fe-based catalysts has made significant progress over the past several decades and so Fe catalysts continue to attract substantial attention today.

Beginning in 1964, with Jasinski's discovery that Co-phthalocyanines could catalyze the ORR at a reduced overpotential, the study of NPM catalysts to replace Pt-based systems has been heavily pursued.<sup>13</sup> Similar to the heme-based systems found in nature, these macrocyclic metal complexes, where the central metal atom is coordinated by N, became one of the central focuses in NPM catalyst research. Researchers later discovered that subjecting these complexes to high temperature treatments could further reduce the ORR overpotential and also increase the stability of the catalysts.<sup>14-16</sup> However, as a result of pyrolysis the catalyst precursors were typically destroyed leading to the formation of new metal species within the final catalyst material. Eventually, new precursors were found that could be more easily obtained and were not as expensive as the metal-macrocycles.<sup>17-24</sup> Among all NPM catalysts, the main requirements are a source of metal (Fe or Co), a source of N (from organic ligand or polymer), and a source of carbon (added directly as a support or resulting from pyrolysis of other precursors). As the pyrolysis treatment occurs, the precursors react to form new metal species and generate the active sites. Typically, several different metal species are produced and due to this catalyst heterogeneity the direct identification of the active site is a significant challenge.

Since the initial reports describing the activity of metal-macrocycles and pyrolyzed catalysts, countless efforts have been devoted to understanding the structure and identifying the active sites in pyrolyzed NPM catalysts made from a wide variety of precursors. Recently, some progress has been made to synthesize catalysts or otherwise produce modified catalysts with a preponderance of certain metal species presumed to be the active site.<sup>12,25,26</sup> But despite these efforts, a general consensus regarding the active site structure has not been reached within the

scientific community and multiple possibilities for the active site are currently proposed in the literature. Additionally, information on the mechanism of the ORR on NPM catalysts is currently lacking. Thus, further clarification of the active site and ORR mechanism for NPM catalysts is needed in order to provide guidance for the development of new designs and synthetic methods able to produce improved NPM catalysts for the ORR.

### **1.3 Lightweight Building Materials Based on Aluminum Alloys**

Another important approach to help mitigate the effects of a changing energy landscape is to design more energy-efficient devices that require less energy to operate. A common approach is the use of lightweight building materials, especially for transportation applications, to replace heavier materials that have been previously used. Such light-weighting strategies are able to reduce the weight of the vehicle in order to increase the fuel economy. Al has become a popular building material due to its light weight, high strength, and chemical resistance. Due to its desirable properties, it has been widely utilized for building airplane fuselages and in recent years has become increasingly employed in the production of automobiles. One current drawback to the use of Al in manufacturing is the necessity for surface treatments to prevent corrosion. Most Al parts fabricated today are passivated via chromate conversion coating, which involves soaking the Al parts in baths containing chromic acid.<sup>27</sup> The use of chromic acid, which contains hexavalent chromium, is hazardous for workers and extremely toxic in the environment. Due to increasing regulations on the use of chromic acid, the development of alternative methods to increase the corrosion resistance for Al is highly desirable.<sup>28</sup>

Attempts to improve the properties of Al alloys by the addition of carbon have been widely explored. Typically, a powder of the alloy is combined with a carbon material via a number of different processes including physical mixing and the application of high temperature

and/or pressure.<sup>29-36</sup> In these cases, the resulting material is a composite mixture of carbon particles within the alloy because of the low solubility of C in Al.<sup>37</sup> For those processes involving temperatures above 600 °C an aluminum carbide phase is also sometimes observed. The mechanical properties of the composite materials produced by the methods previously mentioned are typically different from those of the original Al alloy. Therefore such processing methods allow for the production of potentially useful materials.

Recently a new manufacturing method for carbon-enriched Al alloys was reported. Developed by Third Millennium Materials, LLC the process, which has been called the “electrocharging-assisted process”, involves the blending of carbon particles into a molten Al alloy and simultaneous application of a high current and voltage.<sup>38,39</sup> The resulting material is believed to contain direct bonds between carbon structures and the Al atoms in the alloy which are formed via the ionization of carbon. These materials have thus become known as “covetics” for the proposed mix of covalent and metallic bonding. Initial studies of covetics demonstrated that the mechanical properties were improved from the parent alloy including observations of higher strength and increased hardness.<sup>39-41</sup> Additionally, the possibility of enhanced resistance to oxidation and corrosion has been suggested for covetics.<sup>42,43</sup> Previous work on a non-covetic material showed that graphene could be used to protect a Cu surface from oxidation and more recently, a similar result was observed for Cu covetics.<sup>44-46</sup> To date an investigation of the corrosion behavior of covetics has not been reported. However, previous work studying the structure and corrosion of Al alloys showed that the presence of secondary phases in the alloy can have a noticeable effect on the corrosion properties of the material.<sup>47,48</sup>

## 1.4 Figure

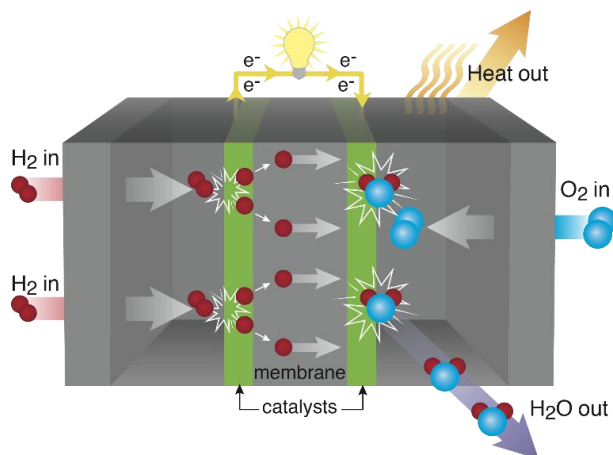


Figure 1.1 Schematic of a H<sub>2</sub> PEM fuel cell showing the reactions occurring at the anode (HOR) and cathode (ORR) during fuel cell operation.

## 1.5 References

- (1) *Global Energy & CO<sub>2</sub> Status Report 2017*, International Energy Agency, 2018.
- (2) *Monthly Energy Review March 2018*, U.S. Energy Information Administration, 2018.
- (3) Stram, B. N. *Energy Policy* **2016**, 96, 728.
- (4) *Handbook of Fuel Cells: Fundamentals, Technology, Applications*; W. Vielstich, A. L., H. Gasteiger, Ed.; John Wiley and Sons: Chichester, U.K., 2003.
- (5) Lutz, A. E.; Larson, R. S.; Keller, J. O. *Int. J. Hydrogen Energy* **2002**, 27, 1103.
- (6) Kartha, S. a. G., *P. Phys. Today* **1994**, 47, 54.
- (7) Gewirth, A. A.; Thorum, M. S. *Inorg. Chem.* **2010**, 49, 3557.
- (8) Wang, Y.-J.; Zhao, N.; Fang, B.; Li, H.; Bi, X. T.; Wang, H. *Chem. Rev.* **2015**, 115, 3433.
- (9) Nie, Y.; Li, L.; Wei, Z. *Chem. Soc. Rev.* **2015**, 44, 2168.

- (10) Cracknell, J. A.; Vincent, K. A.; Armstrong, F. A. *Chem. Rev.* **2008**, *108*, 2439.
- (11) Thorseth, M. A.; Tornow, C. E.; Tse, E. C. M.; Gewirth, A. A. *Coord. Chem. Rev.* **2013**, *257*, 130.
- (12) Gewirth, A. A.; Varnell, J. A.; DiAscro, A. M. *Chem. Rev.* **2018**, *118*, 2313.
- (13) Jasinski, R. *Nature* **1964**, *201*, 1212.
- (14) van Veen, J. A. R.; Colijn, H. A. *Ber. Bunsen Ges. Phys. Chem.* **1981**, *85*, 700.
- (15) van Veen, J. A. R.; van Baar, J. F.; Kroese, K. J. *J. Chem. Soc., Faraday Trans. 1 F* **1981**, *77*, 2827.
- (16) Bagotzky, V. S.; Tarasevich, M. R.; Radyushkina, K. A.; Levina, O. A.; Andrusyova, S. I. *J. Power Sources* **1978**, *2*, 233.
- (17) Lalande, G.; Côté, R.; Guay, D.; Dodelet, J. P.; Weng, L. T.; Bertrand, P. *Electrochim. Acta* **1997**, *42*, 1379.
- (18) Faubert, G.; Côté, R.; Guay, D.; Dodelet, J. P.; Dénès, G.; Poleunis, C.; Bertrand, P. *Electrochim. Acta* **1998**, *43*, 1969.
- (19) Gupta, S.; Tryk, D.; Bae, I.; Aldred, W.; Yeager, E. *J Appl Electrochem* **1989**, *19*, 19.
- (20) Meng, H.; Larouche, N.; Lefèvre, M.; Jaouen, F.; Stansfield, B.; Dodelet, J.-P. *Electrochim. Acta* **2010**, *55*, 6450.
- (21) Proietti, E.; Jaouen, F.; Lefèvre, M.; Larouche, N.; Tian, J.; Herranz, J.; Dodelet, J.-P. *Nat. Commun.* **2011**, *2*, 416.
- (22) Médard, C.; Lefèvre, M.; Dodelet, J. P.; Jaouen, F.; Lindbergh, G. *Electrochim. Acta* **2006**, *51*, 3202.
- (23) Wu, G.; More, K. L.; Johnston, C. M.; Zelenay, P. *Science* **2011**, *332*, 443.

- (24) Zitolo, A.; Goellner, V.; Armel, V.; Sougrati, M. T.; Mineva, T.; Stievano, L.; Fonda, E.; Jaouen, F. *Nat. Mater.* **2015**, *14*, 937.
- (25) Wu, G. *Frontiers in Energy* **2017**, *11*, 286.
- (26) Shao, M.; Chang, Q.; Dodelet, J.-P.; Chenitz, R. *Chem. Rev.* **2016**, *116*, 3594.
- (27) Burleigh, T. D. In *Handbook of Aluminum* 2003; Vol. 2, p 421.
- (28) Twite, R. L.; Bierwagen, G. P. *Progress in Organic Coatings* **1998**, *33*, 91.
- (29) Liao, J.; Tan, M.-J. *Powder Technology* **2011**, *208*, 42.
- (30) Bartolucci, S. F.; Paras, J.; Rafiee, M. A.; Rafiee, J.; Lee, S.; Kapoor, D.; Koratkar, N. *Materials Science and Engineering: A* **2011**, *528*, 7933.
- (31) Bastwros, M.; Kim, G.-Y.; Zhu, C.; Zhang, K.; Wang, S.; Tang, X.; Wang, X. *Composites Part B: Engineering* **2014**, *60*, 111.
- (32) Jeyasimman, D.; Sivaprasad, K.; Sivasankaran, S.; Narayanasamy, R. *Powder Technology* **2014**, *258*, 189.
- (33) Zhao, L.; Lu, H.; Gao, Z. *Advanced Engineering Materials* **2015**, *17*, 976.
- (34) Jeon, C.-H.; Jeong, Y.-H.; Seo, J.-J.; Tien, H. N.; Hong, S.-T.; Yum, Y.-J.; Hur, S.-H.; Lee, K.-J. *International Journal of Precision Engineering and Manufacturing* **2014**, *15*, 1235.
- (35) Laha, T.; Agarwal, A.; McKechnie, T.; Seal, S. *Materials Science and Engineering: A* **2004**, *381*, 249.
- (36) Laha, T.; Chen, Y.; Lahiri, D.; Agarwal, A. *Composites Part A: Applied Science and Manufacturing* **2009**, *40*, 589.
- (37) Qiu, C.; Metselaar, R. *J. Alloys Compd.* **1994**, *216*, 55.

- (38) Shugart, J. V.; Scherer, R. C.; Penn, R. L.; U.S. Patent US20120244033 A1: 2012.
- (39) Salamanca-Riba, L.; Isaacs, R.; Mansour, A. N.; Hall, A.; Forrest, D. R.; LeMieux, M. C.; Shugart, J. *Proceedings of Nanotech Conference and Expo 2012*. **2012**.
- (40) Forrest, D. R.; Jasiuk, I.; Brown, L.; Joyce, P.; Mansour, A.; Salamanca-Riba, L. *Nanotech 2012* **2012**.
- (41) Brown, L.; Joyce, P.; Forrest, D.; Wolk, J. *Proceedings of the SAMPE Fall Technical Conference, Ft. Worth, TX, 17-20 October 2011* **2011**.
- (42) Knych, T.; Kwaśniewski, P.; Kiesiewicz, G.; Mamala, A.; Kawecki, A.; Smyrak, B. *Metallurgical and Materials Transactions B* **2014**, *45*, 1196.
- (43) Jablonski, P. D. *U.S. DOE Advanced Manufacturing Office Program Review Meeting* **2015**.
- (44) Isaacs, R. A.; Zhu, H.; Preston, C.; Mansour, A.; LeMieux, M.; Zavalij, P. Y.; Jaim, H. M. I.; Rabin, O.; Hu, L.; Salamanca-Riba, L. G. *Applied Physics Letters* **2015**, *106*, 193108.
- (45) Tian, J.; Cao, H.; Wu, W.; Yu, Q.; Guisinger, N. P.; Chen, Y. P. *Nano Lett.* **2012**, *12*, 3893.
- (46) Isaacs, R. A.; Jaim, H. M. I.; Cole, D. P.; Gaskell, K.; Rabin, O.; Salamanca-Riba, L. G. *Carbon* **2017**, *122*, 336.
- (47) Cogan, S. F.; Gayle, F. W.; Klein, J. D.; Cocks, F. H.; Shepard, M. L. *Journal of Materials Science* **1978**, *13*, 2687.
- (48) Li, J.; Dang, J. *Metals* **2017**, *7*, 84.

## Chapter 2

### Identification of Carbon-Encapsulated Iron Nanoparticles as Active Species in Non-Precious Metal Oxygen Reduction Catalysts

Reprinted from Varnell, J.A., Tse, E.C.M., Schulz, C.E., Fister, T.T., Haasch, R.T., Timoshenko, J., Frenkel, A.I., Gewirth, A.A, *Nat. Commun.* 2016, 12582. Published 2016 Nature Publishing Group under license CC BY 4.0.

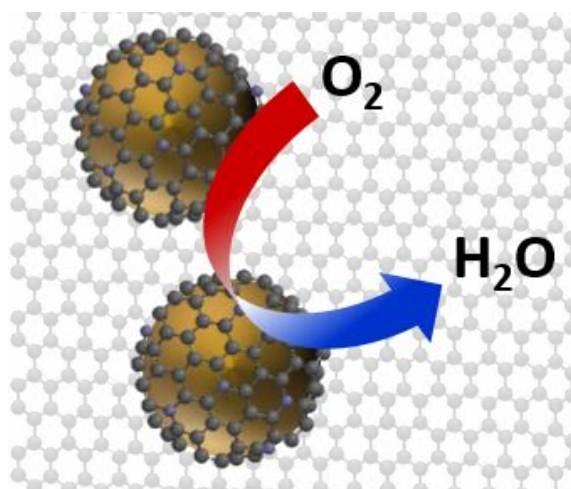


Figure 2.1 Cartoon depiction of the catalytically-active species identified in this work.

### 2.1 Introduction

Fuel cells (FCs) offer a highly efficient method to convert chemical energy into electrical energy. Despite their advantages, FCs currently require the use of Pt-alloy catalysts for the oxygen reduction reaction (ORR), which makes such devices cost-prohibitive for many applications.<sup>1,2</sup> For this reason, non-precious metal (NPM) ORR catalysts have been intensely



investigated, following the discovery of the ORR activity of Co phthalocyanines as early as 1964.<sup>3</sup> Pyrolysis of Fe or Co-containing porphyrins and phthalocyanines affords catalysts of enhanced stability and activity.<sup>4-6</sup> Many other N-containing materials, when pyrolyzed in the presence of Fe salts, also exhibit promising activity.<sup>7-12</sup> Specifically, N-rich polymers such as polyaniline, lead to catalysts with ORR activity approaching that of Pt in acid.<sup>13-16</sup> However, progress toward making enhanced ORR materials is inhibited due to the lack of understanding regarding the ORR active site.

Elucidating the nature of the catalytic center in NPM ORR catalysts is challenging due to the heterogeneity introduced during the high-temperature synthesis which is also retained during ORR operation. Studies utilizing metal-binding ligands such as  $\text{CN}^-$  suggest that the activity in these catalysts is metal-centered.<sup>17-19</sup> Two models for the active site are suggested. The first model consists of a metal particle encapsulated by a carbon shell.<sup>20,21</sup> However, this model does not accommodate the requirement for nitrogen.<sup>5,7,22</sup> A second model invokes a porphyrin-like  $\text{FeN}_4$  (or  $\text{FeN}_{2+2}$ ) structure.<sup>23-26</sup> Studies of ORR-active materials show the presence of both metallic Fe and Fe-N species.<sup>16,24,27,28</sup> ORR catalysts containing a preponderance of either type of site have been recently synthesized, with catalysts featuring  $\text{FeN}_4$  species exhibiting the highest activity to date.<sup>26,29-31</sup> However, the active species in the vast majority of reported NPM catalysts remains unknown due to the heterogeneity present.

Efforts to permanently deactivate a NPM ORR catalyst in order to locate the source of ORR activity have been unsuccessful. Treating the catalyst with strong acid does not remove all of the Fe metal and in fact leads to a more active catalyst.<sup>8,23,27,32-34</sup> The residual metal is assumed to be inactive for ORR, but the results are not definitive. Selective poisoning which could identify specific centers responsible for ORR activity is also problematic. NPM ORR

catalysts exhibit a high tolerance to most anions such as  $F^-$ ,  $SCN^-$ ,  $N_3^-$ , and phosphate.<sup>13,17,18</sup> Both pyrolyzed and unpyrolyzed NPM ORR catalysts are insensitive to CO and while the inhibitory effect of  $CN^-$  has been demonstrated, it can be removed by simply placing the  $CN^-$ -exposed catalyst in fresh electrolyte without  $CN^-$ .<sup>18,35,36</sup> In contrast, the poisoning of the biological Fe heme-based ORR catalyst cytochrome *c* oxidase with CO has been observed.<sup>37,38</sup> The inconsistency in these results leaves room for further clarification into the active species found in the many pyrolyzed and unpyrolyzed ORR catalysts described in literature, including the role of the  $FeN_4$  site in pyrolyzed NPM catalysts due to the lack of poisoning that has been observed in some cases.<sup>37,38</sup> Interestingly, high-temperature treatments with  $H_2S$ ,  $H_2$ , and  $NH_3$  have all increased NPM catalyst activity.<sup>10,25,26,32,39</sup> It has been noted that at high temperatures,  $NH_3$  would likely be decomposed to  $N_2$  and  $H_2$ .<sup>25</sup> These conditions are reducing, but the chemical basis for this enhancement remains unclear.<sup>32</sup> We hypothesized that a high-temperature treatment in an oxidizing atmosphere such as  $Cl_2$  might be able to deactivate an NPM catalyst. Such treatments are used to oxidize and remove metallic impurities from carbon materials via the formation and sublimation of volatile metal chlorides.<sup>40-43</sup>

In this paper we report the effects of high-temperature  $Cl_2$  and  $H_2$  treatments on a NPM ORR catalyst and show that a reproducible deactivation and reactivation of the catalyst are achieved via the respective treatments. Additionally, we show that the heterogeneity of the catalyst is decreased by treatment with  $Cl_2$  and  $H_2$ , which allows for the direct characterization of the species present in the deactivated and reactivated catalysts. Mössbauer spectroscopy, X-ray absorption near edge structure (XANES) and extended X-ray absorption fine structure (EXAFS), and X-ray photoelectron spectroscopy (XPS) reveal the changes induced by the  $Cl_2$  and  $H_2$  treatments and clarify the nature of the ORR-active species.

## 2.2 Results

### 2.2.1 Effect of Cl<sub>2</sub> and H<sub>2</sub> Treatments on ORR Activity

For our work we used a polyaniline-derived catalyst due to their reported high activity and stability which we denote as the “as-prepared” catalyst.<sup>14</sup> We subjected the as-prepared catalyst material to a high-temperature treatment with Cl<sub>2</sub> at 900 °C. The “Cl<sub>2</sub>-treated” catalyst was subsequently treated with H<sub>2</sub> at 900 °C leading to the “H<sub>2</sub>-treated” catalyst.

**Figure 2.2** shows cyclic voltammetry on a rotating disk electrode (RDE) to evaluate the ORR activity of the three catalysts studied. The Cl<sub>2</sub> treatment resulted in a negative shift of the ORR onset by ca. 170 mV. Additionally, an increase in peroxide formation from 1.6% to 5.0% was observed after the Cl<sub>2</sub> treatment using a rotating ring-disk electrode (RRDE) (**Fig. 2.3 and Table 2.1**). These results indicate that the active site is poisoned or destroyed by the Cl<sub>2</sub> treatment. After the H<sub>2</sub> treatment, the ORR activity of the as-prepared catalyst was completely recovered, showing a similar onset potential and low peroxide yield. Repeated treatments with Cl<sub>2</sub> and H<sub>2</sub> on a single batch of as-prepared catalyst revealed that the observed effects are highly controllable (**Fig. 2.4**).

In order to explain the observed deactivation and reactivation of the NPM material, we used inductively coupled plasma optical emission spectroscopy (ICP-OES) to measure the Fe content in the as-prepared, Cl<sub>2</sub>-treated, and H<sub>2</sub>-treated materials (**Table 2.2**). Although the Fe content was decreased by the Cl<sub>2</sub> treatment, some Fe remained and was never completely removed, similar to previous attempts to demetalate the catalyst<sup>8,28</sup>. This result suggests that the form of the Fe present affects the observed ORR activity and not the total Fe content. The oxidizing nature of the Cl<sub>2</sub> treatment favors the formation of oxidized Fe species while the reducing nature of the H<sub>2</sub> treatment causes the formation of reduced Fe species. In addition, the

presence of Cl in the Cl<sub>2</sub>-treated catalyst was observed using elemental analysis (**Table 2.2**). Survey XPS spectra are shown in **Figure 2.5** which also indicate the presence of Cl in the Cl<sub>2</sub>-treated sample. **Figure 2.6** shows the high resolution scans taken in the C 1s region, which show no change in the surface carbon species present before and after the Cl<sub>2</sub> and H<sub>2</sub> treatments.

To see the effects of the treatment temperature, we treated the as-prepared catalyst with Cl<sub>2</sub> at 600 °C and observed that no deactivation occurred (**Fig. 2.7**), consistent with a prior report which found slight ORR activity enhancement following treatment with Cl<sub>2</sub> at 650 °C.<sup>8</sup> **Figure 2.8** shows the XPS survey spectrum of the catalyst following 600 °C Cl<sub>2</sub> treatment which indicates the presence of Cl similar to the 900 °C Cl<sub>2</sub>-treated catalyst. This suggests that the presence of Cl is not responsible for the large deactivation that was observed following Cl<sub>2</sub> treatment at 900 °C on the as-prepared catalyst.

In order to see if the deactivation observed following the Cl<sub>2</sub> treatment at 900 °C was related to the presence of Fe, we synthesized the catalyst without Fe and carried out the same gas treatments at 900 °C. **Figure 2.9** shows the electrochemical activity of the metal-free catalyst before and after treatment with Cl<sub>2</sub> and H<sub>2</sub>. The overall activity of the metal-free catalyst is significantly lower than the catalyst containing Fe and only a small deactivation and reactivation of the metal-free catalyst was observed. **Figures 2.10 and 2.11** show the XPS survey spectra and C 1s region for the metal-free catalyst which displays the same presence of Cl after Cl<sub>2</sub>-treatment and the removal of Cl with the H<sub>2</sub>-treatment that were observed for the Fe-based catalyst. Because of the small effect observed after Cl<sub>2</sub> treatment and the low initial activity of the metal-free catalyst, the presence of the metal in the Fe-containing catalyst must contribute to the higher activity and large deactivation that were observed. In order to discover the nature of the Fe species in the as-prepared and treated catalysts, we utilized several additional methods to

further examine each catalyst and determine the species responsible for the appreciable ORR activity.

### 2.2.2 Mössbauer Spectroscopy

We evaluated the as-prepared and treated catalysts using Mössbauer spectroscopy (**Fig. 2.12**). Assignments for each of the signals observed for the three spectra are given in **Table 2.3** based on previous literature. The Mössbauer spectrum of the as-prepared catalyst (**Fig. 2.12a**) shows FeN<sub>4</sub> species along with Fe<sub>3</sub>C and  $\alpha$ -Fe in the form of both magnetically-split (mag) and superparamagnetic (spm) species, consistent with previous literature.<sup>16</sup> The presence of both oxidized and reduced Fe species in the as-prepared catalysts inhibits identification of the active Fe species. The spectrum of the Cl<sub>2</sub>-treated catalyst (**Fig. 2.12b**) shows a small amount of Fe<sub>x</sub>N and superparamagnetic  $\alpha$ -Fe, with a significantly smaller absorption area than for the as-prepared and H<sub>2</sub>-treated catalyst. The spectrum of the H<sub>2</sub>-treated catalyst (**Fig. 2.12c**) shows only reduced Fe species including the magnetically-split signal of  $\alpha$ -Fe and a singlet from superparamagnetic  $\alpha$ -Fe with additional contributions from Fe<sub>3</sub>C. Noticeably absent in the H<sub>2</sub>-treated catalyst is the signature of any Fe-N species including FeN<sub>4</sub> and Fe<sub>x</sub>N.

The small absorption area observed for the Cl<sub>2</sub>-treated catalyst is not caused by the removal of Fe from the catalyst, because after H<sub>2</sub>-treatment (without the addition of Fe), the absorption area is relatively large. This indicates that the Fe species present after the Cl<sub>2</sub> treatment are not tightly bound to the carbon matrix and are not in the form of large crystallites. Such species would be undetectable by Mössbauer spectroscopy since the recoil-free absorption requires the Fe atoms to be fixed in a solid lattice.<sup>44</sup>

Additionally, we performed Mössbauer spectroscopy on the catalyst treated with Cl<sub>2</sub> at 600 °C and a catalyst that was first treated with Cl<sub>2</sub> at 900 °C and then with H<sub>2</sub> at 600 °C. Both

of these treated catalysts exhibited similar activity of the as-prepared catalyst as shown in **Figures 2.7 and 2.13** and their Mössbauer spectra reveal the presence of reduced Fe species (**Fig. 2.14 and 2.15 and Table 2.4**). These results indicate that Cl<sub>2</sub> treatment at 600 °C, does not remove all of the reduced Fe present and therefore does not alter the activity of the catalyst. Similarly, the higher activity of the samples treated with H<sub>2</sub> at 600 °C and the presence of regenerated reduced Fe show that these species can be correlated to the changes in activity that we have observed. Since the Cl<sub>2</sub> treatment at 600 °C also introduces Cl into the surface of the catalyst as demonstrated by XPS in **Figure 2.8** the lack of a deactivation at 600 °C indicates that the presence of Cl on the surface of the catalyst does not cause the deactivation observed with Cl<sub>2</sub> at 900 °C. Cl is removed by the H<sub>2</sub> treatment at 600 °C as shown in **Figure 2.16**, but the simultaneous reduction of Fe species is responsible for the reactivation.

The magnetic nature of the samples was further investigated using vibrating sample magnetometry (VSM) (**Fig. 2.17**). Superparamagnetic Fe species are present in the as-prepared and H<sub>2</sub>-treated catalysts, as indicated by the sigmoidal curve and lack of a ferromagnetic hysteresis. In the Cl<sub>2</sub>-treated catalyst, the superparamagnetic signal is diluted by the presence of paramagnetic Fe species. **Figure 2.18** displays the electron paramagnetic resonance (EPR) spectra which indicate the presence of paramagnetic species in the as-prepared and Cl<sub>2</sub>-treated catalysts but not in the H<sub>2</sub>-treated catalyst. In all EPR spectra superparamagnetic Fe species contribute a broad background signal.

### 2.2.3 X-ray Absorption Spectroscopy

Fe K-edge EXAFS and XANES spectra were used to determine the local bonding environment of the Fe in each sample. **Figure 2.19a** shows the normalized XANES spectra for the catalysts studied and standards with insets displaying the structural models of the standards

that are used. The spectra of the as-prepared and the H<sub>2</sub>-treated catalysts both show strong metallic character, resembling the spectrum of metal Fe foil. The spectrum of the Cl<sub>2</sub>-treated catalyst shows Fe in a higher oxidation state with a structure very similar to hydrated FeCl<sub>3</sub> (FeCl<sub>3</sub>·xH<sub>2</sub>O).<sup>45</sup> **Figures 2.19b and 2.19c** show the corresponding Fe K-edge EXAFS data in *k*-space and after their Fourier transform to *R*-space. It is evident that in the Cl<sub>2</sub>-treated catalyst the interatomic distances are shorter, compared to the as-prepared and H<sub>2</sub>-treated catalysts, and the nearest neighbors of Fe in the Cl<sub>2</sub>-treated catalyst are relatively light elements, similar to those in FeCl<sub>3</sub>·xH<sub>2</sub>O. These conclusions follow from the lower *R*-space peak distances (**Fig. 2.19c**), and the fact that EXAFS oscillations are peaked at lower values of wavenumber *k* (**Fig. 2.19b**), respectively. In the H<sub>2</sub>-treated catalyst EXAFS spectra show strong similarity to Fe foil that hints on the bcc structure of the former. Lower amplitudes of EXAFS oscillations for the H<sub>2</sub>-treated catalyst with respect to those of metallic foil reveal reduced coordination numbers and/or enhanced structural disorder. One can thus expect that metallic Fe is in a disordered and nanostructured form in H<sub>2</sub>-treated catalyst.

Quantitative analysis of EXAFS data in the Cl<sub>2</sub>- and H<sub>2</sub>-treated catalysts was performed by non-linear least square fitting of theoretical EXAFS spectra to the data in *R*-space, using FEFFIT program.<sup>46</sup> Theoretical photoelectron scattering amplitudes and phases were calculated using ab-initio FEFF8.5 code.<sup>46,47</sup> First coordination shell fitting was performed for the Cl<sub>2</sub>-treated catalyst, while advanced multiple-shell analysis was used for the H<sub>2</sub>-treated catalyst. Data and best fits are displayed in **Figure 2.20**. A summary of the best fit values of structural parameters are given in **Table 2.5**. For the Cl<sub>2</sub>-treated sample the coordination numbers of Fe with O and Cl were found to be 2±1 and 4±1, respectively, and the Fe-Cl distance was obtained

to match that of  $\text{FeCl}_3 \cdot x\text{H}_2\text{O}$ . These values indicate the presence of hydrated  $\text{FeCl}_3$  and lack of metallic Fe in the sample following the  $\text{Cl}_2$  treatment.

For the  $\text{H}_2$ -treated catalyst we find that bcc model provides a good fit, in support of our preliminary conclusions from examination of the raw data. The coordination numbers for the first two nearest neighbor Fe-Fe shells for the  $\text{H}_2$ -treated catalyst were obtained to be  $5.7 \pm 0.8$  and  $3 \pm 2$ , respectively, i.e., significantly smaller than the corresponding values for bulk bcc Fe (8 and 6, respectively). This indicates that the Fe is present in the nanoparticle form.<sup>48</sup> From the best fit values of the coordination numbers of the first few shells, the nanoparticle size can be estimated, assuming particular structure and shape.<sup>48</sup> Assuming the bcc-type structure and cubic shape, the particle size in the  $\text{H}_2$ -treated sample is calculated to be approximately 1.0–1.5 nm (**Fig. 2.21**). This finding is consistent with other recent reports on Fe-based electrocatalysts.<sup>33,49</sup> The values of the mean-square relative displacement (MSRD) for Fe-Fe pairs were slightly larger for the  $\text{H}_2$ -treated catalyst compared to Fe foil, indicating the presence of larger structural disorder, which is expected in small particles.

In order to further evaluate the size and disorder of the Fe nanoparticles in the as-prepared and  $\text{H}_2$ -treated catalysts we used transmission electron microscopy (TEM) and scanning transmission electron microscopy (STEM). **Figures 2.22 and 2.23** show TEM and STEM images of all catalysts studied respectively. Fe nanoparticles ranging from 10 to 30 nm are observed in the as-prepared and  $\text{H}_2$ -treated samples while in the  $\text{Cl}_2$ -treated sample no nanoparticles are seen, but evidence of the graphitic carbon shells previously formed around Fe nanoparticles are visible. Additionally, we carried out fitting of the VSM data for the as-prepared and  $\text{H}_2$ -treated samples using the Langevin function for superparamagnetic particles giving a third measurement of particle size (**Fig. 2.24**).<sup>33</sup> For the as-prepared catalyst the average



particle size from fitting was 3.22 nm, while the average particle size for the H<sub>2</sub>-treated catalyst was 3.80 nm. Powder XRD indicated the presence of reduced Fe species in the as-prepared and H<sub>2</sub>-treated catalysts, however the signal from the carbon support prevented further analysis of the XRD data (**Fig. 2.25**).

The discrepancy in the size of the Fe particles for the as-prepared and H<sub>2</sub>-treated catalysts as measured using TEM/STEM, EXAFS, and VSM can be explained by the size ranges that each technique is able to sample and indicates a high degree of heterogeneity and, possibly, disorder among the reduced Fe species that are observed. Similar results have been obtained in a recent study using EXAFS and (S)TEM on a material with heterogeneous particle sizes which showed that these techniques complement and not contradict each other.<sup>50</sup> Additionally, disagreement between TEM and VSM has been reported previously for two types of NPM ORR catalysts possibly due to granularity in the particles observed by TEM and by the presence of disordered Fe-phases within the observed particles which are non-magnetic.<sup>33</sup>

#### **2.2.4 X-ray Photoelectron Spectroscopy**

In order to determine the role of N in the Fe-containing and metal-free catalysts used in our study we carried out high resolution XPS in the N 1s region. In recent work on NPM and metal-free catalysts the direct involvement of N species during ORR, especially pyridinic N and Fe-N, has been implicated.<sup>27,51,52</sup> The resulting spectra for the Fe-containing catalyst are shown in **Figure 2.26** and the spectra for the metal-free catalyst are shown in **Figure 2.27**. For both the Fe-containing and metal-free catalysts oxydic, graphitic, pyrrolic, and/or pyridinic N species were observed as assigned from previous literature and given in **Table 2.6**.<sup>24,27</sup> Following Cl<sub>2</sub> treatment and H<sub>2</sub> treatment the bands associated with pyridinic species decreased slightly but no major changes in N speciation occurred. The fact that there were no major changes in N

speciation following the  $\text{Cl}_2$  and  $\text{H}_2$  treatments suggests that the type of N species that is present does not explain any of the changes in ORR activity that we have observed. Therefore, it is likely that the active site in these catalysts does not involve N or Fe-N moieties. Graphitic N is the dominant species in all of the catalysts that we studied, which indicates that N is doped into the graphitic carbon that surrounds and protects the Fe nanoparticles. The presence of graphitic N in active NPM ORR catalysts is observed in other work.<sup>16,27,33</sup>

### 2.3 Discussion

Mössbauer and XAS show that in the as-prepared catalyst, a combination of  $\text{FeN}_4$  and reduced Fe species are present in agreement with previous reports, which makes the direct characterization of the active species difficult.<sup>16,28,34</sup> Through the use of a  $\text{Cl}_2$  treatment we show that the metallic Fe and  $\text{FeN}_4$  species are converted into dispersed  $\text{FeCl}_3 \cdot x\text{H}_2\text{O}$  which is reformed into reduced Fe species by the  $\text{H}_2$  treatment as shown in **Figure 2.28**. The absence of  $\text{FeN}_4$  sites in the  $\text{H}_2$ -treated catalyst indicates that these sites are not required for the observed ORR activity. In order to confirm that metal centered sites are not involved in the ORR we carried out selective poisoning experiments using KCN similar to previous work by our group.<sup>18</sup> **Figure 2.29** shows CVs in the absence and presence of  $\text{CN}^-$  which confirm that the behavior of the as-prepared,  $\text{Cl}_2$ -treated, and  $\text{H}_2$ -treated catalysts is very different from that of unpyrolyzed Fe phthalocyanine. The lack of a significant poisoning effect supports our observation that  $\text{FeN}_4$  species are not the active species in the catalysts we studied. XPS in the N1s region shows oxydic, graphitic, pyrrolic, and/or pyridinic N in all of the catalysts studied, with only minor changes in the relative amounts of each species further indicating that N speciation does not play a major role in determine the ORR activity before and after the  $\text{Cl}_2$  and  $\text{H}_2$  treatments. From these results we conclude that a reduced Fe phase, in the form of small superparamagnetic nanoparticles which

are encapsulated by thin layers of N-doped carbon, can be linked to the ORR activity of the H<sub>2</sub>-treated catalyst. We note that although we show FeN<sub>4</sub> are not required for ORR activity, FeN<sub>4</sub> centers may be active in other systems.<sup>26,31</sup>

If FeN<sub>4</sub> species are not the locus of ORR activity in the H<sub>2</sub>-treated material, the question remains as to the role of N in ORR catalyst preparation. To address this question, we omitted aniline during synthesis to make a N-free version of the as-prepared catalyst. The resultant N-free material displayed minimal ORR activity compared to the as-prepared catalyst made with aniline as shown in **Figure 2.30**. Interestingly, the N-free catalyst is ferromagnetic indicating the presence of larger Fe particles which are capable of forming magnetic domains as shown in **Figure 2.31**. Powder XRD on the N-free catalyst shows that all of the Fe present is in the form of Fe-oxides (magnetite and hematite), which are inactive toward the ORR (**Fig. 2.32**). Elemental analysis of the N-free catalyst shows that the material contains virtually no C or N suggesting that the presence of the polymeric N species is required to prevent the complete removal of C during pyrolysis (**Table 2.7**). The association of Fe with N and N with C in the catalyst during pyrolysis must play an important role in promoting the formation of the carbon-encapsulated Fe nanoparticles that are observed. The initial coordination of Fe to N should help to form the small superparamagnetic Fe particles within the carbon support. One possible explanation for this observation is that the N species function as nucleation sites for the formation of small superparamagnetic Fe particles. Another explanation is that the use of polymeric N-containing precursors helps to template and form small Fe particles during synthesis. In this way, the recent results reported utilizing extremely low Fe loading to achieve highly active Fe-based NPM catalysts could be explained by the formation of extremely small Fe

nanoparticles or Fe clusters which are contained within the carbon support and function as the active species.<sup>26,31</sup>

There are also other possible explanations for the role of N not excluded by this work. The formation of basic N sites, which tune the surface functionality, could increase the activity of the catalyst.<sup>52</sup> Additionally, density functional theory (DFT) calculations suggest that N-incorporation decreases the work function at the surface of the carbon-encapsulated nanoparticle helping to facilitate ORR.<sup>29</sup> It is possible that the incorporation of N may contribute to the enhanced ORR activity of NPM catalysts through one or more different effects. More work is needed in order to identify the specific roles of N in both the formation of catalytic sites during synthesis and possible participation of N species in the active sites during ORR.

In order to investigate the possibility of the formation of new active species during ORR the as-prepared and H<sub>2</sub>-treated catalysts were investigated during and after operation. The electrochemical activity was unchanged during operation as observed by CV (**Fig. 2.33**). XPS obtained after ORR operation exhibits a decrease in pyridinic N and an increase in pyrrolic N while the oxydic and graphitic N remain (**Fig. 2.34**). This result again suggests that the pyridinic N species are not required for ORR. Vibrating sample magnetometry (VSM) performed before and after ORR operation shows a decrease in the magnetization due to the dissolution of unprotected surface species while the signature of small superparamagnetic particles is maintained (**Fig. 2.35**). In order to mitigate any effects from putative dissolved Fe, both catalysts were run in electrolyte solution containing up to 100 mM of ZnClO<sub>4</sub> and MnClO<sub>4</sub>. The excess of Zn and Mn, which are ORR inactive metals, should fill the vacant N sites and prevent any dissolved Fe from coordinating. Using CV, no effect on the ORR activity was observed with either Zn or Mn in the electrolyte (**Fig. 2.36**). Together, the electrochemical tests along with XPS

and VSM show that there were no new Fe or Fe-N species formed during operation and suggest that the Fe particles encapsulated by C and graphitic N are responsible for the observed activity and stability of NPM catalysts.

*In situ* XAS studies of other NPM ORR catalysts show the stability of the protected Fe particles from oxidation as well as the absence of the formation of FeN<sub>4</sub> structures.<sup>29,30</sup> EXAFS reports that Fe particles encapsulated by carbon stored in ambient conditions for over 2 years are not oxidized.<sup>53</sup> The lack of FeN<sub>4</sub> sites and the encapsulation of Fe particles could possibly help to explain the puzzling observation that CO does not poison pyrolyzed NPM ORR catalysts.<sup>35</sup> The absence of strong sensitivity to small molecule poisons can be explained by the electronic interaction of the active species with molecular O<sub>2</sub>. In this case the donation of electron density from the Fe particle to the carbon shell allows for efficient ORR catalysis. This model for shell-encapsulated Fe nanoparticles has been implicated in the hydrogen evolution reaction (HER) where DFT suggests that electron density is donated from the Fe particle to individual atoms in the graphitic shell.<sup>49,54</sup> DFT calculations have also been used to explain the catalytic activity of encapsulated Fe particles for the ORR which are present in many NPM ORR catalysts.<sup>29</sup> Furthermore, recent work has shown the important role of N-doping in enhancing the catalytic activity of carbon-encapsulated Fe nanoparticles.<sup>30</sup>

In summary, we utilized a purification process with Cl<sub>2</sub> and H<sub>2</sub> treatments to produce active ORR catalysts with catalytic centers of improved definition. Two clear conclusions can be drawn: (i) FeN<sub>4</sub> sites are not required to generate an active ORR catalyst and (ii) reduced Fe species protected by carbon are active catalytic species for the ORR. We showed that Fe particles encapsulated by graphitic C and N present in the H<sub>2</sub>-treated catalyst exhibit the same ORR activity as the as-prepared catalyst which we identify as the active species. Our findings reveal

that synthetic methods favoring the formation of a large number of small Fe particles encapsulated by N-doped carbon will lead to the discovery of improved NPM ORR catalysts.

## 2.4 Experimental Methods

*Preparation of Catalyst Material-* Synthesis of the Fe-based NPM ORR catalyst was carried out following the procedure described in previous literature.<sup>13-15</sup> Carbon black (Ketjenblack EC 300J) was treated in 0.1 M HCl for 24 hours and then in 70% HNO<sub>3</sub> at 80 °C for 8 hours before being filtered and dried in an oven at 80 °C overnight. In a large round bottom flask 2.5 mL of aniline was dispersed in 500 mL of 2.0 M HCl. The mixture was cooled in an ice bath until it was below 10 °C, at which point 10 g of FeCl<sub>3</sub> and 5 g of ammonium peroxydisulfate were added. After stirring for 3 hours, 0.4 g of the treated carbon support was added and mixed for 48 hours. The suspension was evaporated at 80 °C until dry and the resulting solid material was ground using a mortar and pestle into a fine powder. The powder was placed in a tube furnace and pyrolyzed under flowing N<sub>2</sub> at 900 °C for 1 hour. The sample was then ground a second time and leached in 500 mL of 0.5 M H<sub>2</sub>SO<sub>4</sub> at 80 °C for 8 hours followed by a second pyrolysis under flowing N<sub>2</sub> at 900 °C for 3 hours. The resulting material was labeled as “as-prepared” catalyst.

*Cl<sub>2</sub> and H<sub>2</sub> Treatments-* Warning: Cl<sub>2</sub> is highly corrosive and toxic. H<sub>2</sub> is flammable and explosion may occur. For the Cl<sub>2</sub> treatment the “as-prepared” catalyst material was placed in a tube furnace and heated under an inert Ar atmosphere to 900 °C, at which point Cl<sub>2</sub> (Matheson, 99.999%) was flowed over the catalyst for 30 minutes. The treated sample was then allowed to cool to room temperature under Ar and labeled as “Cl<sub>2</sub>-treated”. For the H<sub>2</sub> treatment, the Cl<sub>2</sub>-treated catalyst was heated to 900 °C under Ar, at which point a 50:50 mixture of Ar and H<sub>2</sub> was flowed over the catalyst for 30 minutes before cooling to room temperature under Ar. The

resulting material was labeled as “H<sub>2</sub>-treated”. The same treatment under pure Ar resulted in only partial recovery of catalyst activity (**Fig. 2.37**) and significant removal of Cl (**Table 2.8**). To study temperature effects the same procedure was carried out using Cl<sub>2</sub> at 600 °C on the as-prepared catalyst and a H<sub>2</sub> treatment at 600 °C was carried out on the Cl<sub>2</sub>-treated (900 °C) catalyst. We note that treatment above 900 °C resulted in activity loss, even under Ar (**Fig. 2.38**) so treatments above 900 °C were not used.

*Electrochemical Activity Measurements-* The ORR activity of the prepared samples was measured using a rotating disk electrode (RDE) and a rotating ring-disk electrode (RRDE) in a 3-compartment electrochemical cell. Aqueous electrolyte solutions were prepared using Milli-Q purified water (>18 MΩ cm) and HClO<sub>4</sub> (70 wt %, Fisher). Solutions were sparged with either Ar or O<sub>2</sub> for 30 minutes prior to each experiment. Catalyst inks were prepared by dispersing 5 mg of catalyst powder in 175 μL of EtOH and 47.5 μL of 5% Nafion solution (Sigma Aldrich) using sonication. In all tests, 5 μL of the catalyst ink was drop-cast onto a glassy carbon (GC) electrode (A=0.196 cm<sup>2</sup>) and allowed to dry under a stream of N<sub>2</sub>. The GC disk was polished sequentially with 0.25 and 0.05 μm diamond polish (Buehler) and sonicated in water before use. For RRDE experiments the Pt ring was electrochemically polished prior to each experiment by cycling the electrode in dilute HNO<sub>3</sub> solution. The ring potential was held at 1.23 V vs. RHE during RRDE experiments to efficiently oxidize peroxide to oxygen. RDE and RRDE electrodes were attached to an MSR<sub>X</sub> rotator (Pine Instruments) and rotated at 1600 rpm during all experiments. Cyclic voltammetry was carried out using a CH Instruments 760 D Electrochemical Workstation (Austin, TX) at room temperature with a “no-leak” Ag/AgCl (3 M KCl) reference electrode (EDAQ) separated from the working electrode by a Luggin capillary. A carbon rod counter electrode was separated from the working electrode by a glass frit. All potentials were

converted to RHE by measuring the open-circuit potential of a Pt wire working electrode in H<sub>2</sub> saturated electrolyte immediately following catalyst testing.

*Physical Characterization-* Mössbauer measurements were performed on a constant acceleration spectrometer (Knox College) at 300 K. X-ray absorption spectroscopy was carried out at sector 9 BM at the Advanced Photon Source at Argonne National Lab with a beam cross section of 2.6 × 0.75 mm. Samples were studied *ex situ* by pressing the catalyst powder into a pellet. All measurements were recorded in transmission mode using a double-crystal Si (111) monochromator run at 50% detuning and ion chamber detectors filled with a mixture of He/N<sub>2</sub>. X-ray photoelectron spectroscopy was performed using a Kratos AXIS Ultra spectrometer with a monochromatic Al K $\alpha$  (1486.6eV) X-ray source. All binding energies were referenced to graphitic carbon at 284.5 eV. Vibrating sample magnetometry was performed at 300 K using the Magnetic Property Measurement System (Quantum Design) with the sample placed in a plastic capsule and inserted into a brass rod. Electron paramagnetic resonance spectra were recorded on a Varian E-line 12" Century Series X-band CW spectrometer. Powder XRD was performed using a Siemens/Bruker D5000 diffractometer with Cu K- $\alpha$  radiation ( $\lambda=0.15418$  nm). Inductively coupled plasma optical emission spectroscopy (ICP-OES) was carried out on a PerkinElmer 2000DV ICP-OES. Sample powders were digested using 4 mL HNO<sub>3</sub>, 1 mL HCl, and 1 mL HF in a commercial microwave digestion until the solution became clear and no solids remained present. TEM was performed on a JEOL 2010 TEM with a LaB<sub>6</sub> filament at 200 kV and STEM was performed using a JEOL 2010F STEM with a Schottky field emitter at 200 kV.

*Methods for EXAFS Data Analysis-* FEFFIT program<sup>46</sup> was used to analyze EXAFS data in hydrated iron (III) chloride (FeCl<sub>3</sub>·xH<sub>2</sub>O) and Cl<sub>2</sub>-treated catalyst. We obtained theoretical photoelectron scattering amplitudes and phases from ab-initio calculations with FEFF8.5 code<sup>47</sup>



for  $\text{FeCl}_3 \cdot 6\text{H}_2\text{O}$  model (see inset in **Fig. 2.19a**).<sup>45</sup> For FEFF calculations the complex exchange-correlation Hedin-Lundqvist potential and default values of muffin-tin radii as provided within the FEFF8.5 code were employed. Fitting was carried out in  $R$ -space. Fourier transforms (FTs) were carried out in the range from  $k_{\min} = 2.0 \text{ \AA}^{-1}$  to  $k_{\max} = 11.0 \text{ \AA}^{-1}$ . The  $R$ -range used in the analysis was from  $1.0 \text{ \AA}$  to  $2.4 \text{ \AA}$ .

The composition of the first coordination shell in  $\text{FeCl}_3 \cdot x\text{H}_2\text{O}$  and  $\text{Cl}_2$ -treated catalyst was modeled with two contributions from (i) Cl atoms and (ii) lighter atoms (C, N or O). Because EXAFS analysis cannot discriminate between these three latter backscatters, we represented them all in our calculations by Fe-O pair. Analysis of  $\text{FeCl}_3 \cdot x\text{H}_2\text{O}$  was performed first. We assumed that Fe-Cl coordination number in this case is the same as in  $\text{FeCl}_3 \cdot 6\text{H}_2\text{O}$ , and is equal to 2. Fe-O coordination number, corrections to the model Fe-O and Fe-Cl distances, and the corresponding MSRD factors were allowed to vary in the fits. Additional fitting variable was the correction  $\Delta E$  to the photoelectron energy origin  $E_0$ . The best fit value of the  $\Delta E$  was obtained to be close to 0. Amplitude reduction factor  $S_0^2$  was found to be approximately equal to 0.85. Both the  $\Delta E$  and  $S_0^2$  values were subsequently fixed at these values for analysis of the  $\text{Cl}_2$ -treated catalyst. The fitting parameters were the corrections to the model Fe-O and Fe-Cl distances, their corresponding MSRD values, as well as the corresponding Fe-O and Fe-Cl coordination numbers. The reduced  $\chi^2$  values were ca. 78 for  $\text{FeCl}_3 \cdot x\text{H}_2\text{O}$  and ca. 94 for  $\text{Cl}_2$ -treated NPM catalyst material. The obtained values for Fe-Cl interatomic distances for  $\text{FeCl}_3 \cdot x\text{H}_2\text{O}$  and  $\text{Cl}_2$ -treated NPM catalyst material were obtained to be similar, but the coordination numbers were found to be different (**Table 2.5**).

For the  $\text{H}_2$ -treated catalyst multiple-scattering analysis was performed using FEFFIT and FEFF8.5 codes. FTs were carried out in the range from  $k_{\min} = 3.0 \text{ \AA}^{-1}$  up to  $k_{\max} = 12.5 \text{ \AA}^{-1}$ . The

$R$ -range used in the analysis was from 0.8 Å to 5.2 Å. The bcc structure model was used to generate theoretical amplitudes and phases for all paths included in the fit. We included the nearest single-scattering (SS) and the most important multiple-scattering (MS) paths: linear double and triple scattering paths and double-scattering (DS) paths within the first coordination shell. To reduce the number of independent fitting parameters, all half path lengths  $R_i$  of all the (SS and MS) paths used in the fit were constrained to be  $R_i = r_i (1+\epsilon)$ , where  $r_i$  is the corresponding value for a model bcc structure and  $\epsilon$  is an isotropic lattice expansion/contraction parameter. MSRD factors and coordination numbers for SS contributions were fitted independently. Coordination numbers, distances and disorder parameters in collinear multiple-scattering paths were constrained to be related to those in the corresponding single scattering paths.<sup>48</sup>

For the analysis of EXAFS data for the foil, additional two fitting parameters were included:  $S_0^2$  and  $\Delta E_0$ . Their best values of 0.67 and 0.7 eV, respectively, obtained for Fe foil data, were then fixed in fits of the data for H<sub>2</sub>-treated NPM catalyst material. The reduced  $\chi^2$  values were ca. 635 for Fe foil and ca. 609 for the H<sub>2</sub>-treated NPM catalyst material.

**Figure 2.21** displays calculated behaviors of the first two coordination numbers of Fe-Fe pairs as a function of nanoparticle size, corresponding to cubic shape and bcc structure of the model particles. The corresponding best fit values for the H<sub>2</sub>-treated NPM catalyst, together with their error bars, are shown as well. The intercepts of the experimental values and model curves define the region of sizes where experiment and model agree. For the two coordination shells, these regions overlap in the 1.0–1.5 nm range, which indicates that the Fe particles are, on the average, of 1.0–1.5 nm in size.<sup>48</sup>

*Method for VSM Fitting-* VSM data was fit using the Langevin function for superparamagnetic particles given by:

$$\frac{M}{M_{sat}} = L\left(\frac{M_s V H}{k_B T}\right) \quad (1)$$

where  $M$  is equal to the magnetization ( $\text{emu g}^{-1}$ ),  $M_{sat}$  is equal to the saturation magnetization ( $\text{emu g}^{-1}$ ),  $M_s$  is equal to the spontaneous magnetization determined for Fe using the magnetic moment of an Fe atom in metallic Fe ( $2.2 \mu_B$ ) and the volume of a BCC Fe unit cell ( $\text{emu cm}^{-3}$ ),  $V$  is equal to the volume of a particle ( $\text{cm}^3$ ),  $H$  is equal to the applied magnetic field,  $k_B$  is the Boltzmann constant ( $\text{cm}^2 \text{g s}^{-2} \text{K}^{-1}$ ), and  $T$  is the temperature (K).  $L(x) = \coth(x) - 1/x$  is the Langevin function. Average particle diameter was calculated by determining the value of  $V$  for each sample and assuming spherical Fe particles.

## 2.5 Figures and Tables

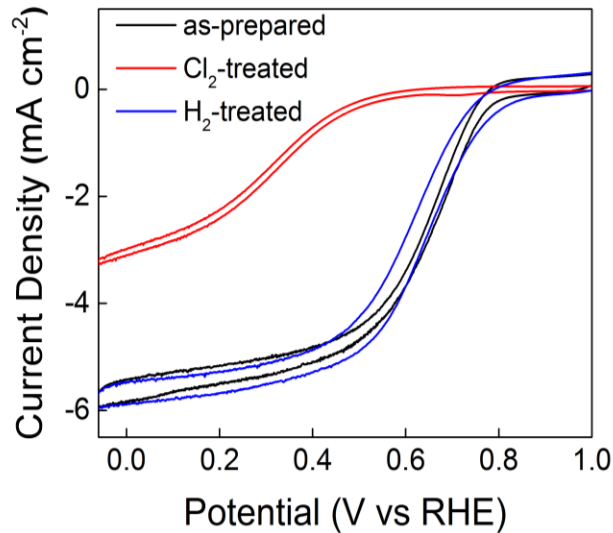


Figure 2.2 Cyclic voltammograms of ORR on as-prepared,  $\text{Cl}_2$ -treated, and  $\text{H}_2$ -treated catalysts in 0.1 M  $\text{HClO}_4$ .

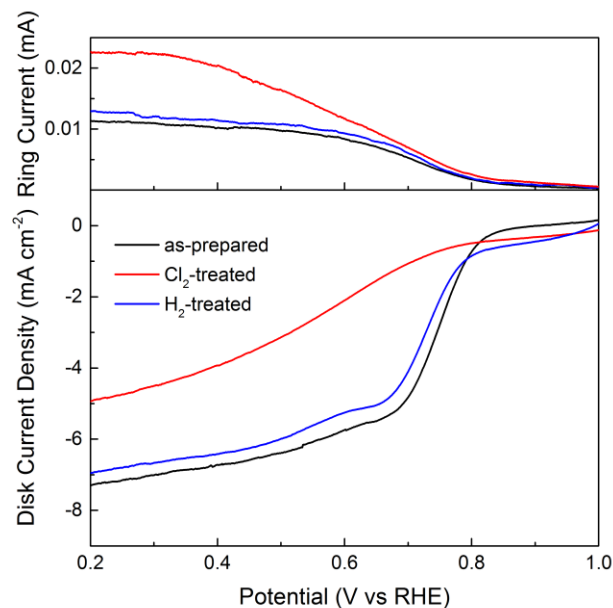


Figure 2.3 Linear sweep voltammograms and corresponding rotating ring disk electrode data for the as-prepared, Cl<sub>2</sub>-treated, and H<sub>2</sub>-treated catalysts recorded in 0.1 M HClO<sub>4</sub> with Pt ring held at 1.23 V vs RHE.

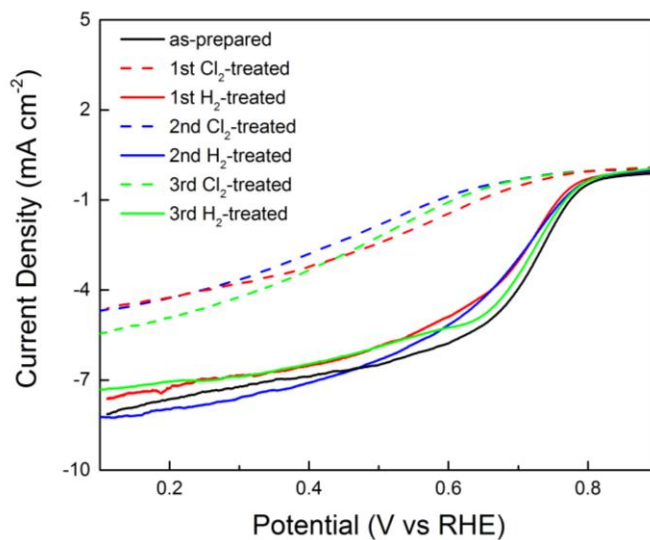


Figure 2.4 Cyclic voltammograms for several repeated treatments of Cl<sub>2</sub> and H<sub>2</sub> on a single batch of as-prepared catalyst in 0.1 M HClO<sub>4</sub>. All Cl<sub>2</sub> and H<sub>2</sub> treatments were carried out at 900 °C for 30 minutes.

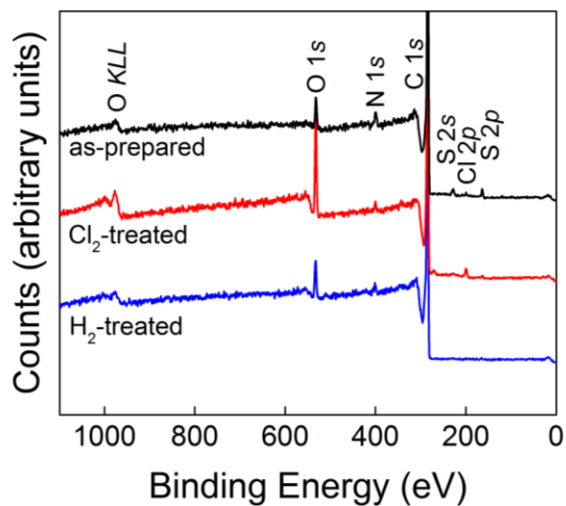


Figure 2.5 Spectra of as-prepared,  $\text{Cl}_2$ -treated, and  $\text{H}_2$ -treated catalysts showing the surface species present on each catalyst studied.

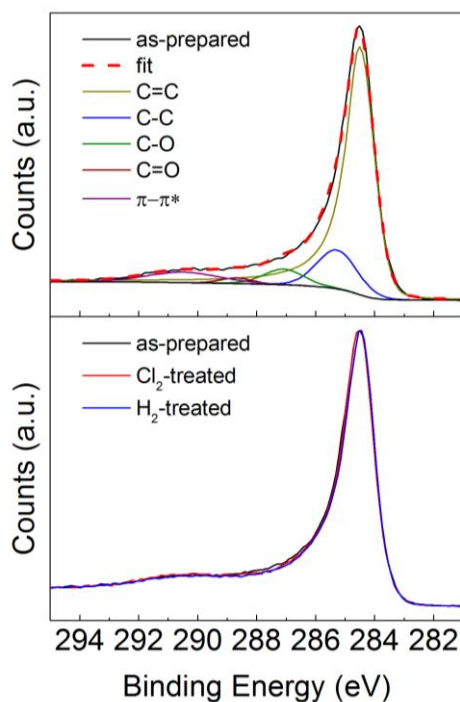


Figure 2.6 C 1s XPS spectra for Fe catalysts with peak fitting for the as-prepared catalyst and overlay of intensity normalized spectra for the as-prepared,  $\text{Cl}_2$ -treated, and  $\text{H}_2$ -treated catalysts. The main signal from the carbon black was fitted to the lineshape of graphitic  $\text{sp}^2$ -type carbon.

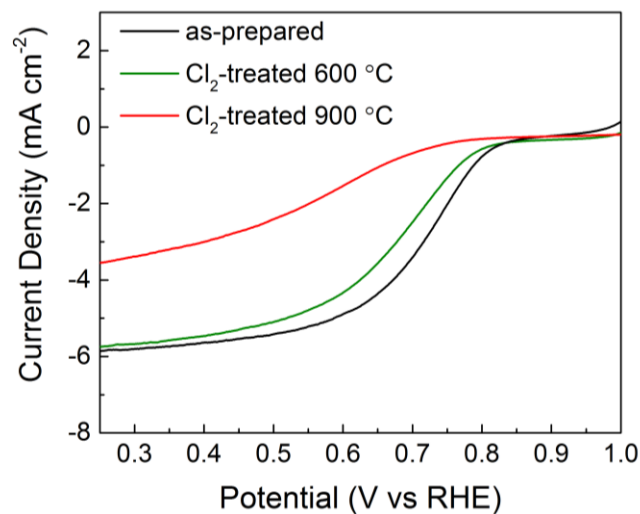


Figure 2.7 Cyclic voltammograms showing the ORR activity of the as-prepared catalyst before and after 600 °C and 900 °C Cl<sub>2</sub> treatment recorded in 0.1 M HClO<sub>4</sub>.

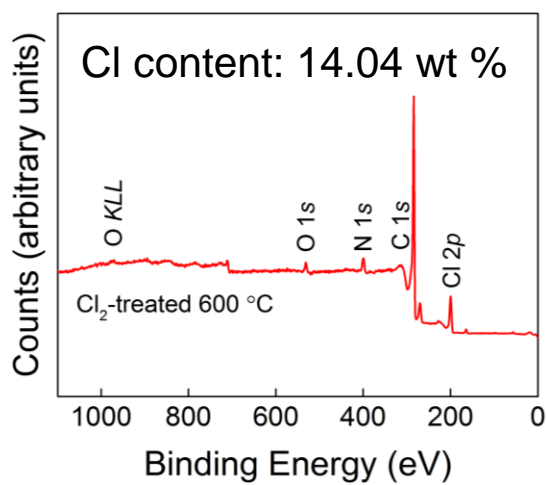


Figure 2.8 XPS survey spectrum of 600 °C Cl<sub>2</sub> treatment. The Cl content was determined from elemental analysis.

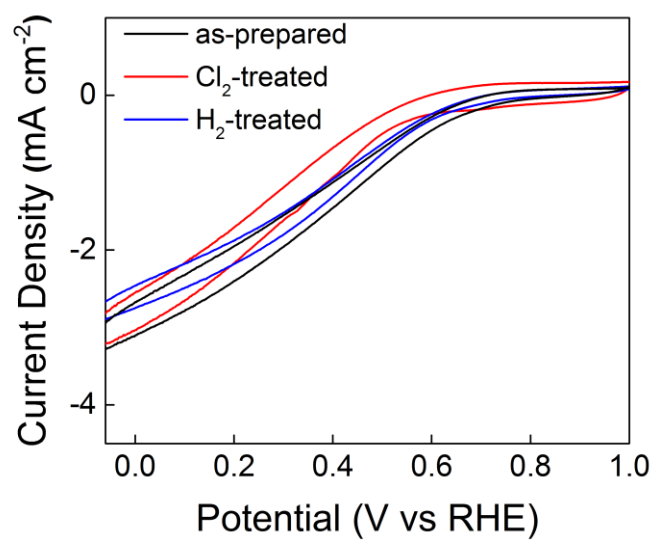


Figure 2.9 Cyclic voltammograms of ORR on metal-free as-prepared, Cl<sub>2</sub>-treated, and H<sub>2</sub>-treated catalysts in 0.1 M HClO<sub>4</sub>.

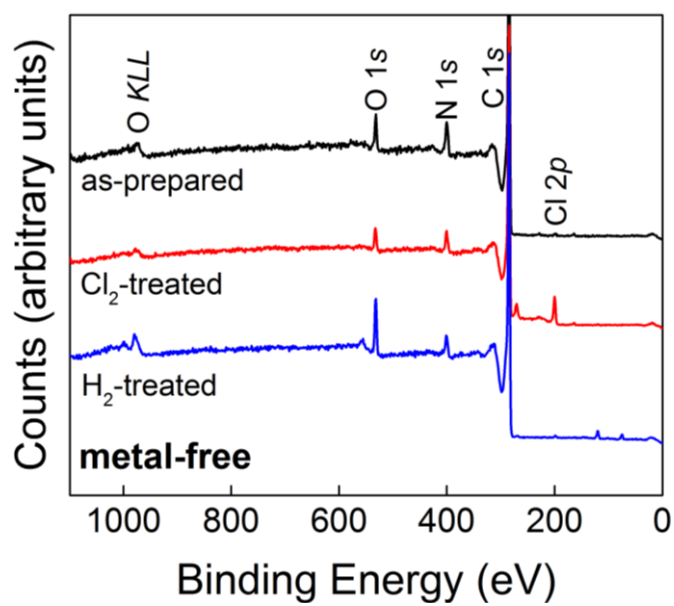


Figure 2.10 XPS survey spectra for metal-free catalysts studied in this work.

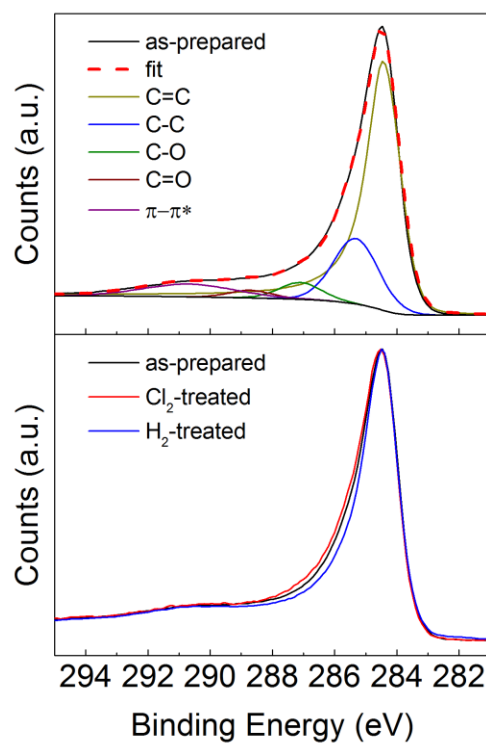


Figure 2.11 C 1s XPS spectra for metal-free catalysts with peak fitting for the as-prepared catalyst and overlay of intensity normalized spectra for the as-prepared, Cl<sub>2</sub>-treated, and H<sub>2</sub>-treated catalysts. The carbon black was fitted to the lineshape of graphitic sp<sup>2</sup>-type carbon.



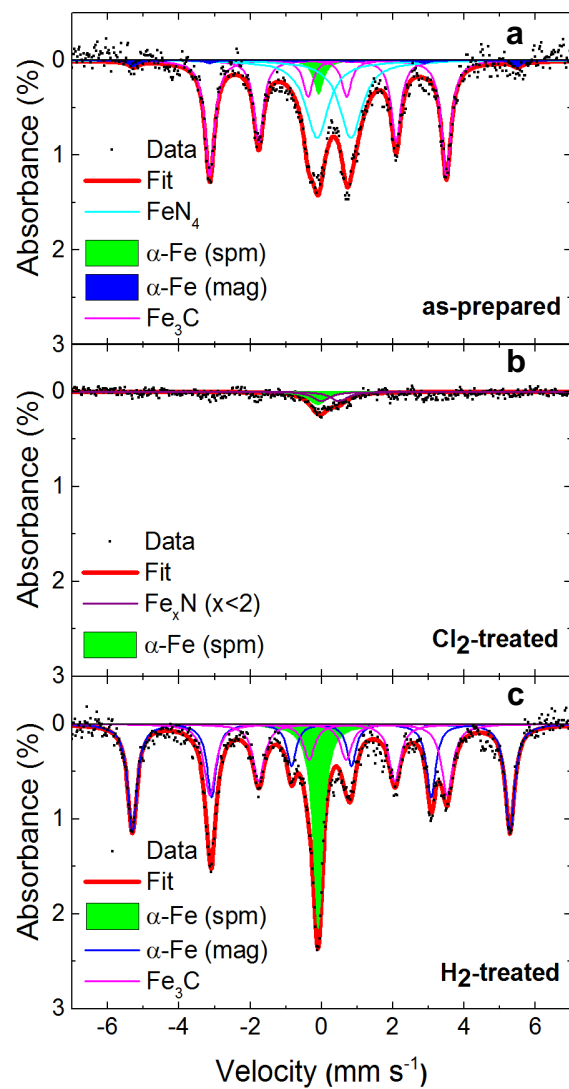


Figure 2.12 Mössbauer spectra and peak fitting of as-prepared (a), Cl<sub>2</sub>-treated (b), and H<sub>2</sub>-treated (c) catalysts at 300 K.

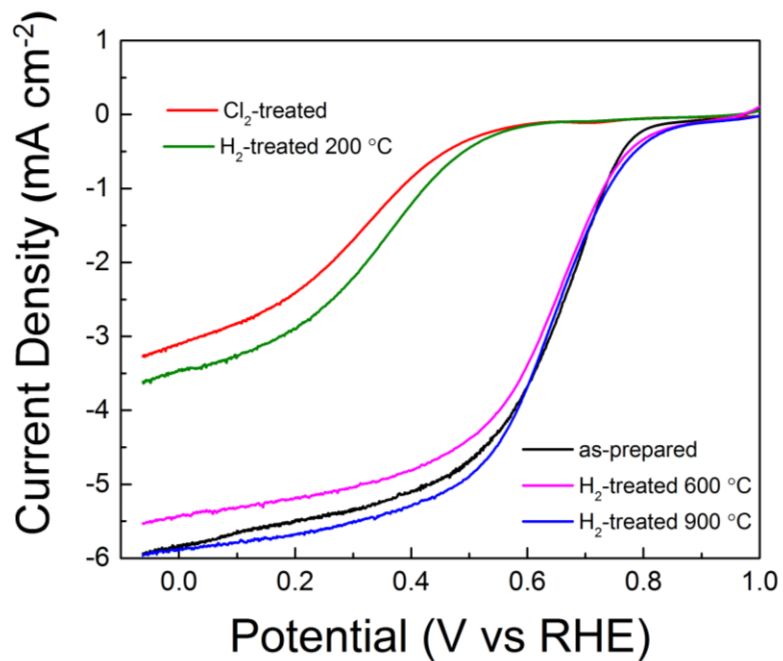


Figure 2.13 Cyclic voltammograms of catalyst treated with Cl<sub>2</sub> at 900 °C followed by treatment with H<sub>2</sub> at increasing temperatures.

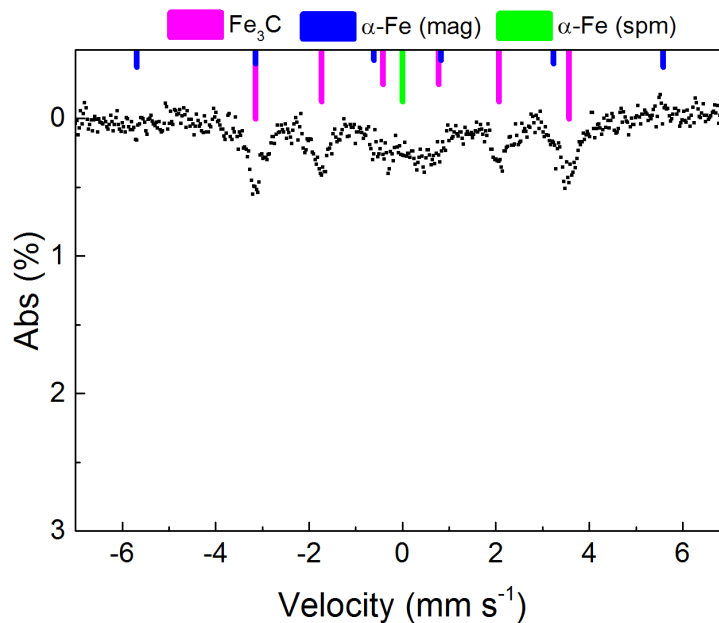


Figure 2.14 Mössbauer spectrum of sample treated with  $\text{Cl}_2$  at  $600\text{ }^\circ\text{C}$  for 30 minutes with peak locations for reduced Fe species:  $\text{Fe}_3\text{C}$ ,  $\alpha\text{-Fe (mag)}$  and  $\alpha\text{-Fe (spm)}$ . Treatment with  $\text{Cl}_2$  at  $600\text{ }^\circ\text{C}$  does not remove all reduced Fe species present in the as-prepared catalyst. The smaller absorption area signifies that only the exposed Fe is removed. We note that similar results treating with  $\text{Cl}_2$  at  $650\text{ }^\circ\text{C}$  have been previously observed.<sup>8</sup>

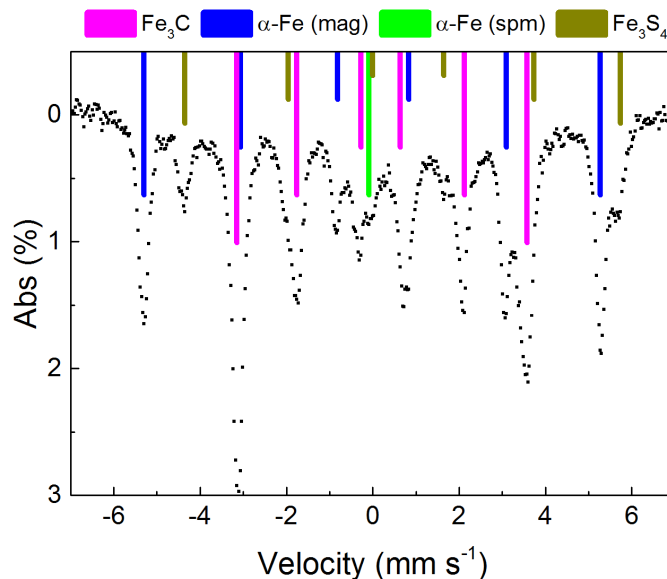


Figure 2.15 Mössbauer spectrum of sample treated with H<sub>2</sub> at 600 °C for 30 minutes following Cl<sub>2</sub> treatment at 900 °C with peak locations for reduced Fe species: Fe<sub>3</sub>C, α-Fe (mag) and α-Fe (spm). Additionally, a new species identified as Fe<sub>3</sub>S<sub>4</sub> is present with fitting parameters given in **Table 2.4** which has been reported in previous literature.<sup>16</sup> It is evident that the presence of this Fe<sub>3</sub>S<sub>4</sub> has no effect on catalyst activity. Treatment with H<sub>2</sub> at 600 °C effectively reduces the Fe present in the Cl<sub>2</sub>-treated catalyst to reform the reduced Fe species present in the as-prepared catalyst and catalyst treated with H<sub>2</sub> at 900 °C.

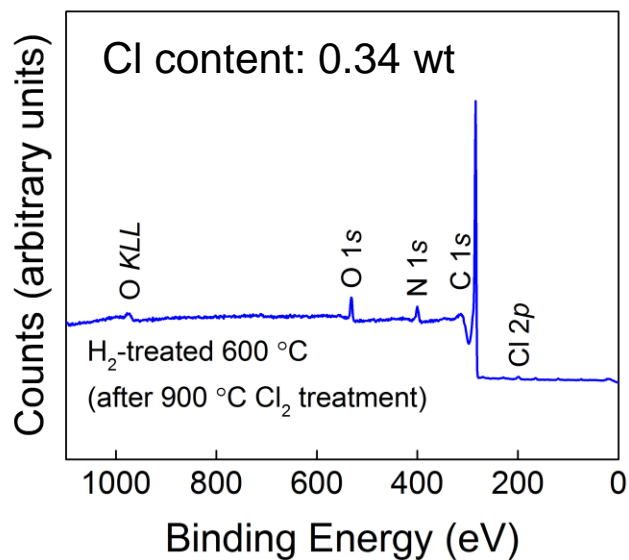


Figure 2.16 XPS survey spectrum for sample treated with H<sub>2</sub> at 600 °C. The Cl content was determined from elemental analysis.

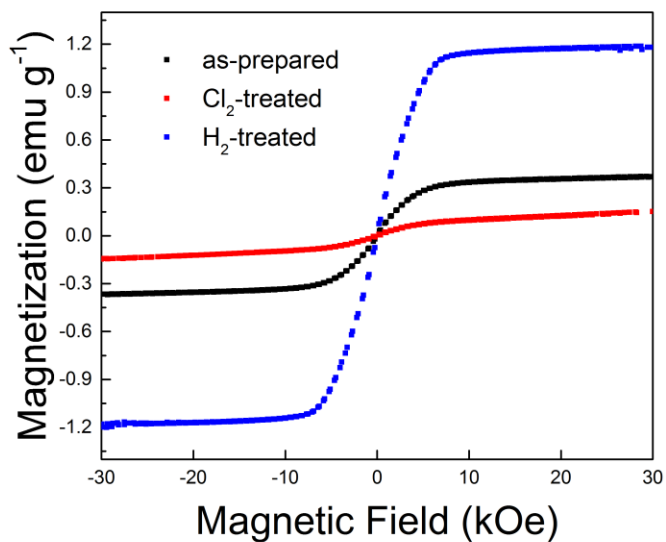


Figure 2.17 Vibrating sample magnetometry data at 300 K showing the magnetization of the catalyst materials. A sigmoidal shape and lack of central hysteresis indicates the presence of superparamagnetic species. A diagonal shape indicates the presence of paramagnetic species.

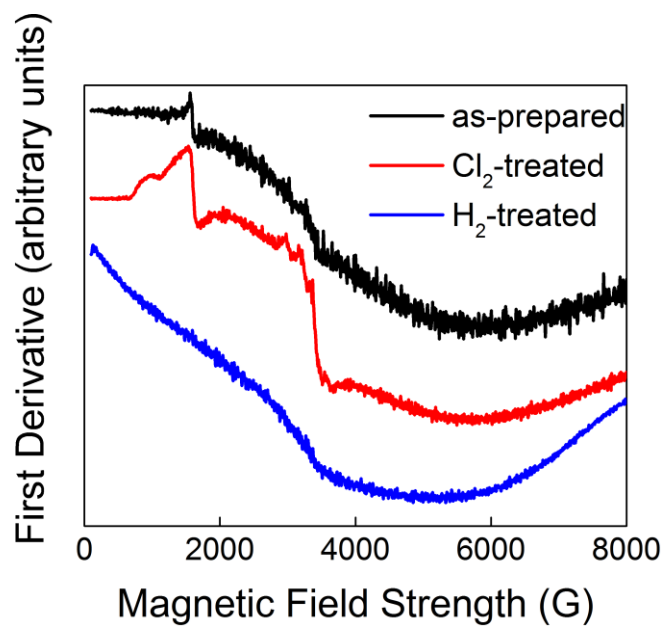


Figure 2.18 X-band EPR spectra recorded at 77 K for catalysts. The features at low field strength indicate the presence of paramagnetic species. The broad background indicates the presence of superparamagnetic or ferromagnetic particles. Microwave frequencies of 9.2782 GHz, 9.2848 GHz, and 9.2818 GHz were used for the as-prepared, Cl<sub>2</sub>-treated, and H<sub>2</sub>-treated respectively.

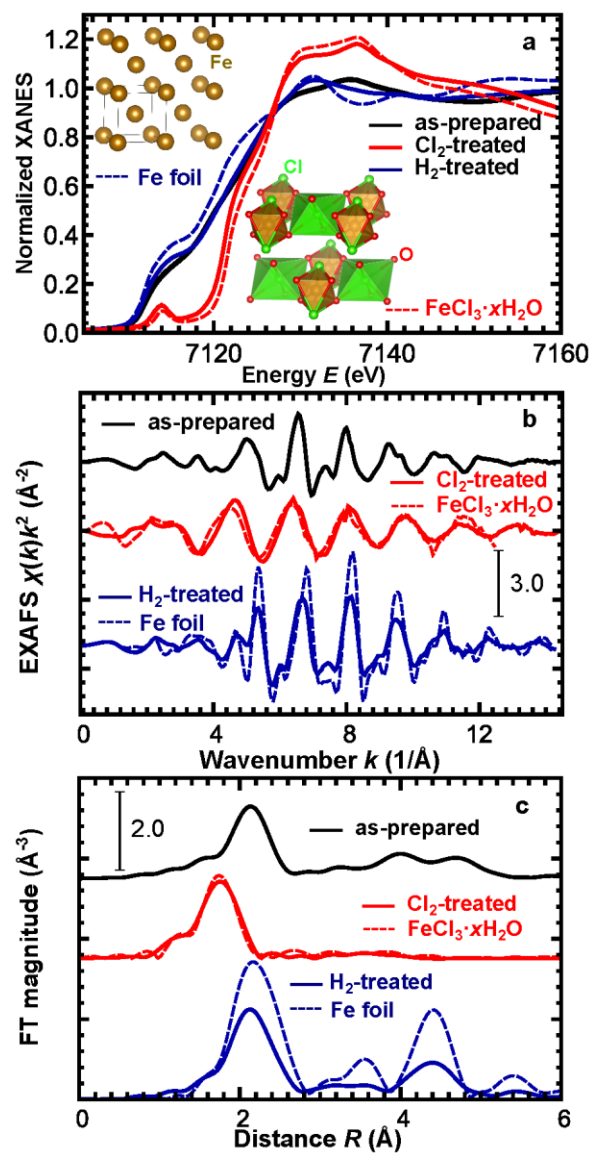


Figure 2.19 XANES (a), EXAFS (b) and Fourier transforms (FTs) of EXAFS (c). Dashed lines show spectra for reference materials: Fe foil (bcc structure) and hydrated Fe (III) chloride ( $\text{FeCl}_3 \cdot x\text{H}_2\text{O}$ ). Structures of reference materials are shown in the insets of panel (a).

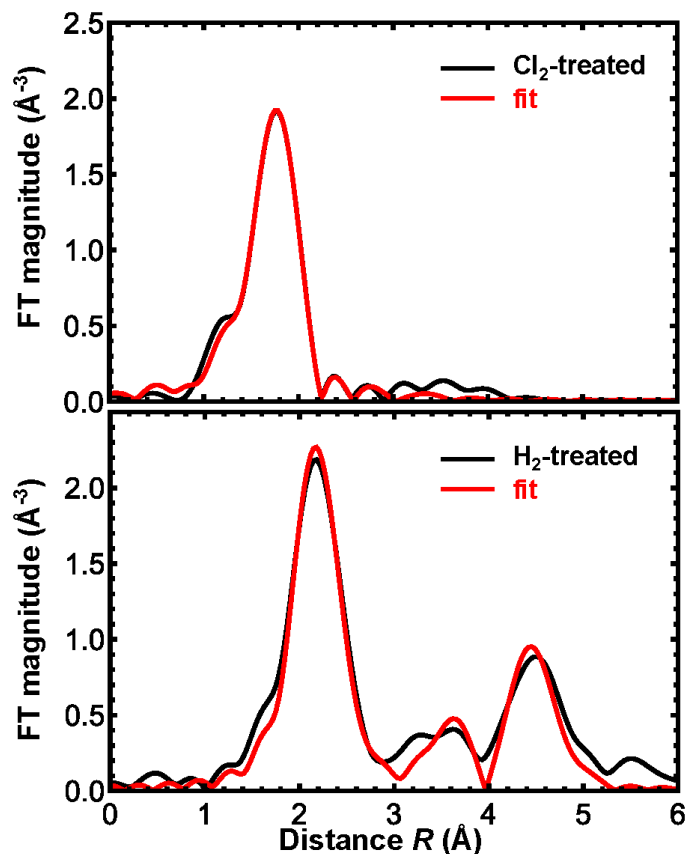


Figure 2.20 Fourier transforms of experimental EXAFS spectra and best fit results.



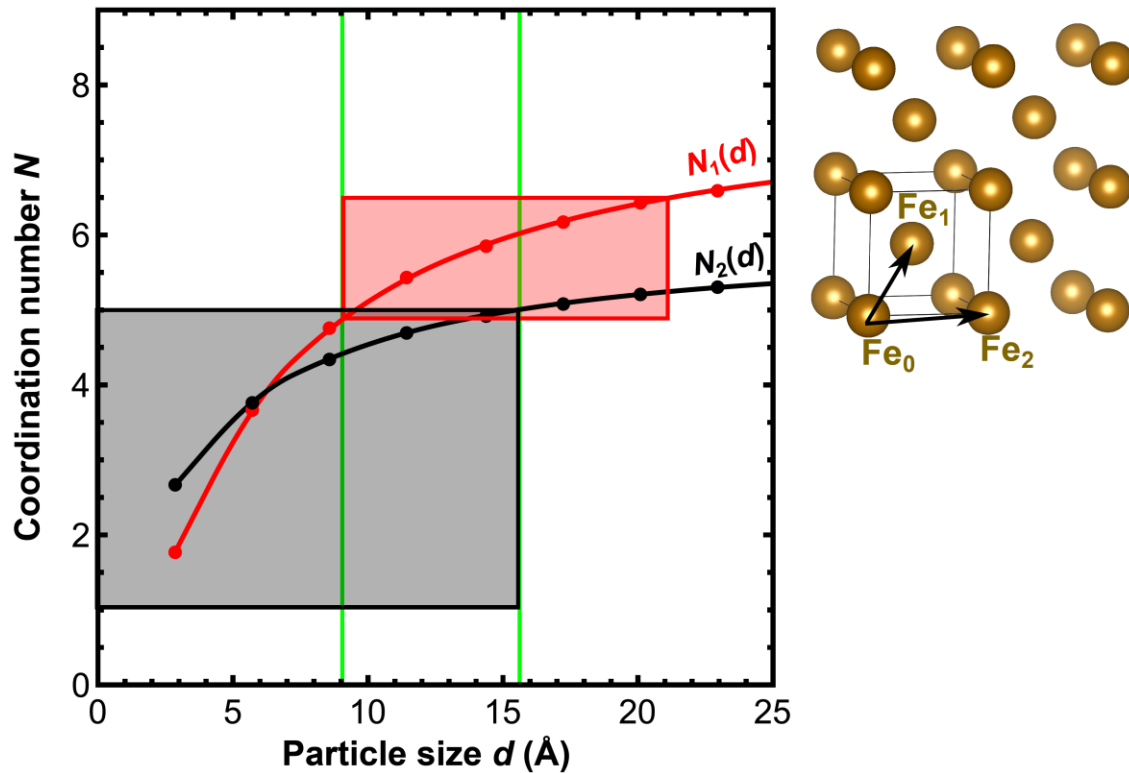


Figure 2.21 Red and black dots and solid lines show calculated dependencies of coordination numbers  $N_1(d)$  and  $N_2(d)$  on particle size  $d$  for cubic particles with bcc-type Fe structure (see schematic picture on the right). Vertical positions and heights of filled rectangles correspond to the best fit values for coordination numbers  $N_1$  (red) and  $N_2$  (black) and their uncertainties for  $H_2$ -treated material. The area between two vertical green lines shows the range of particle sizes, consistent with the values for  $N_1$  and  $N_2$ , obtained from fit.

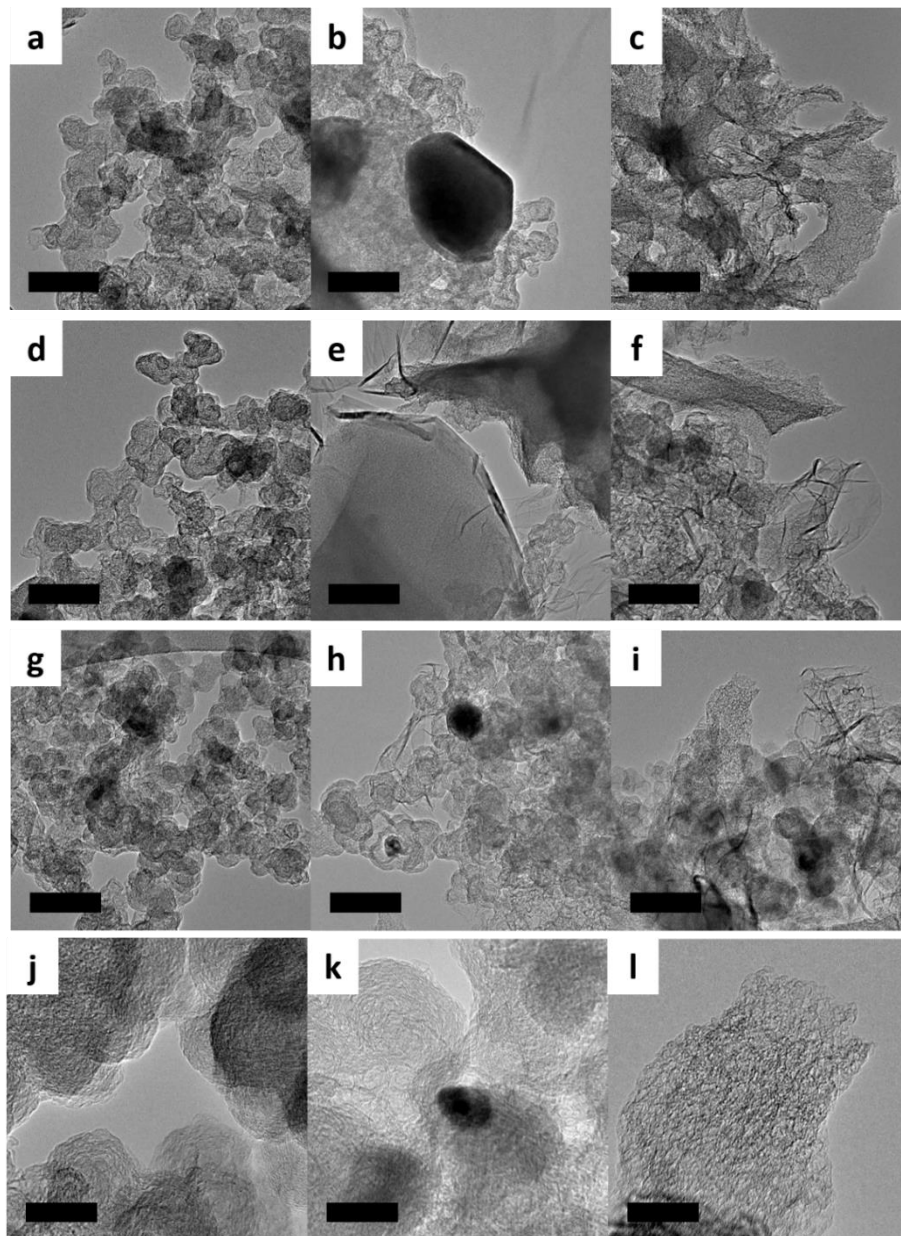


Figure 2.22 Representative TEM images of the as-prepared (a-c),  $\text{Cl}_2$ -treated (d-f), and  $\text{H}_2$ -treated (g-l) catalysts. All catalysts examined show the presence of the carbon support particles c.a. 50 nm in diameter and amorphous carbon regions. The as-prepared and  $\text{H}_2$ -treated catalysts contain carbon encapsulated Fe nanoparticles (b, h, k) while the  $\text{Cl}_2$ -treated catalyst shows evidence of hollow/fractured layered carbon regions (e) indicating Fe nanoparticle removal. Scale bars (a-i) 100 nm (j-l) 20 nm.

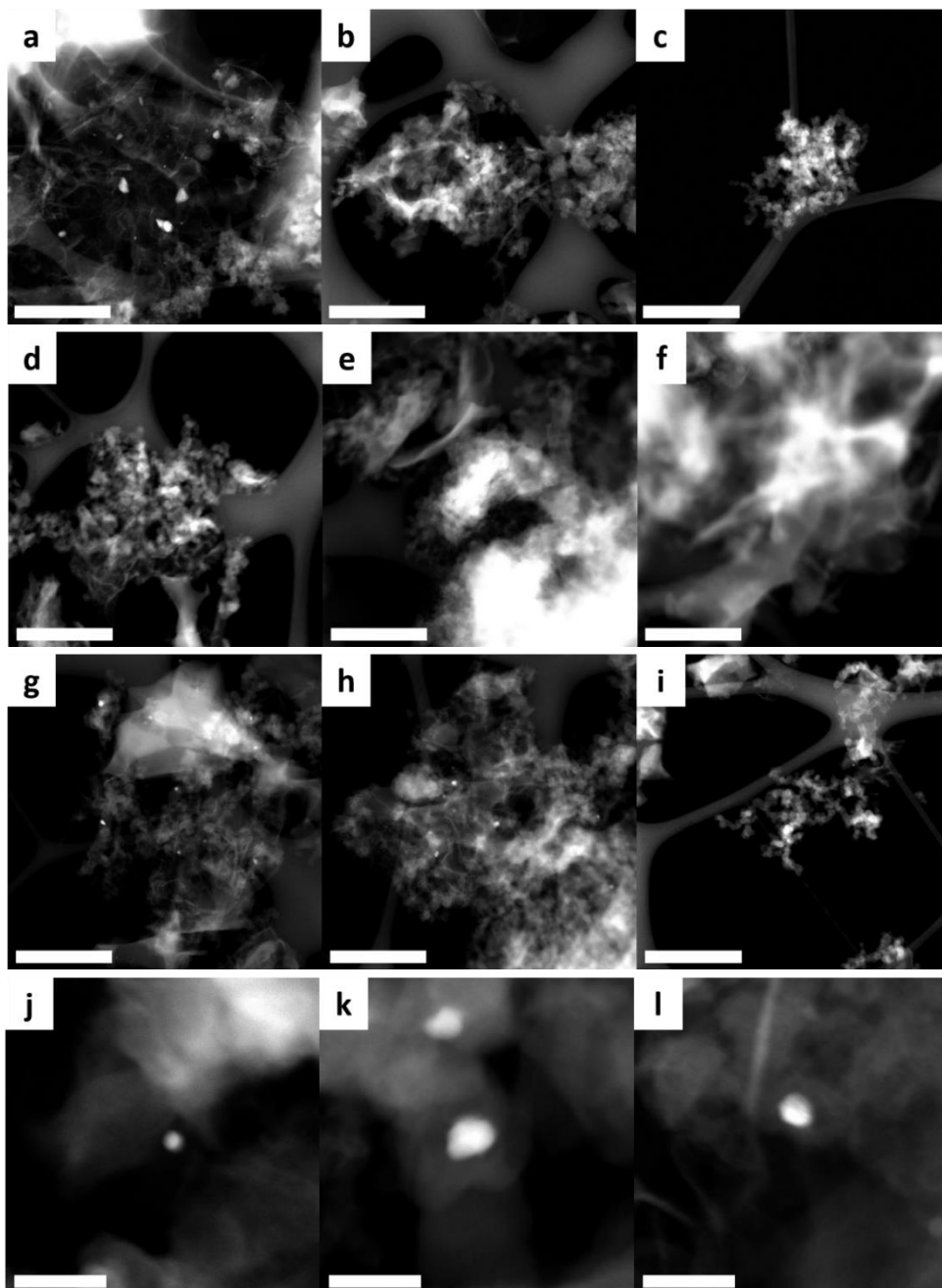


Figure 2.23 Representative STEM images of the as-prepared (a-c),  $\text{Cl}_2$ -treated (d-f), and  $\text{H}_2$ -treated (g-l) catalysts. In the as-prepared and  $\text{H}_2$ -treated catalysts the presence of Fe nanoparticles is observed with the particle size in the  $\text{H}_2$ -treated catalyst around 5-25 nm. In the  $\text{Cl}_2$ -treated catalyst the presence of brighter regions caused by stronger diffraction is observed, possibly from  $\text{FeCl}_3$  regions. Scale bars (a-i) 500 nm (j-l) 50 nm.

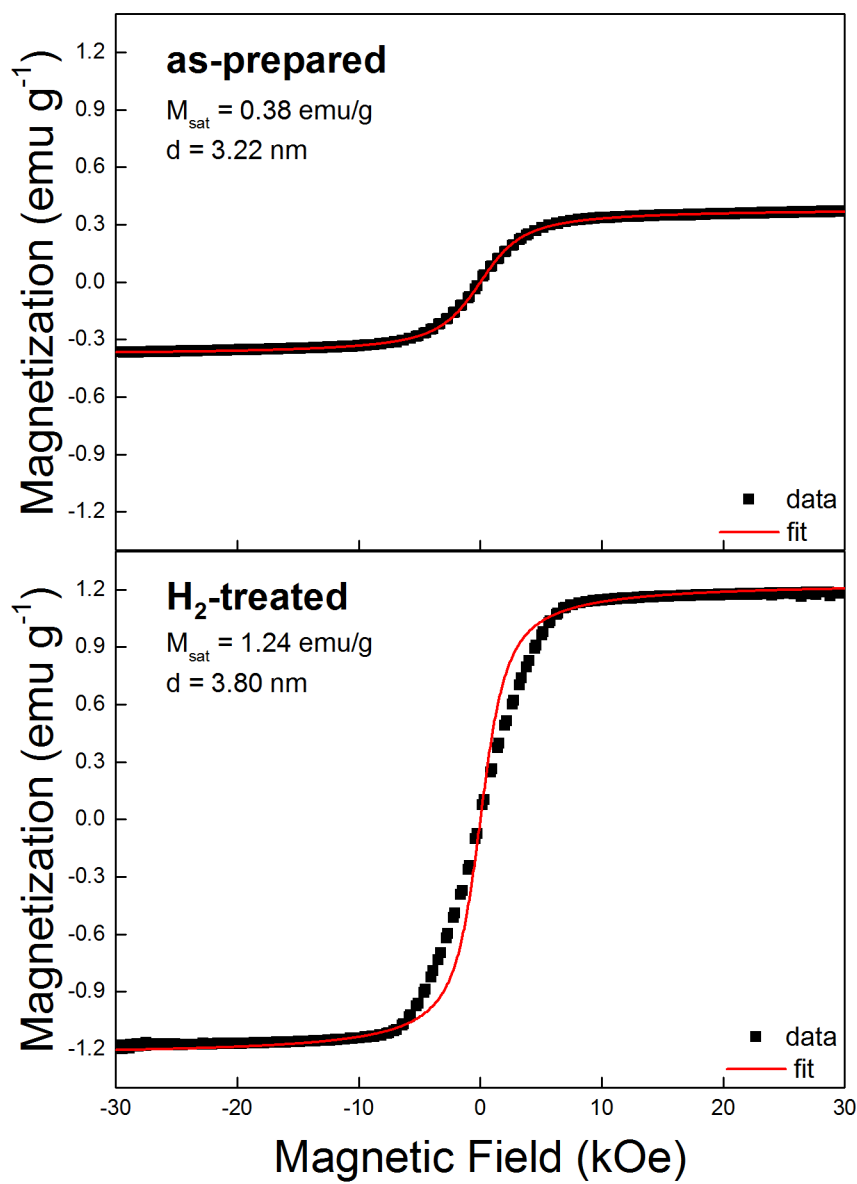


Figure 2.24 Vibrating sample magnetometry (VSM) fitting for the as-prepared and H<sub>2</sub>-treated catalyst materials.

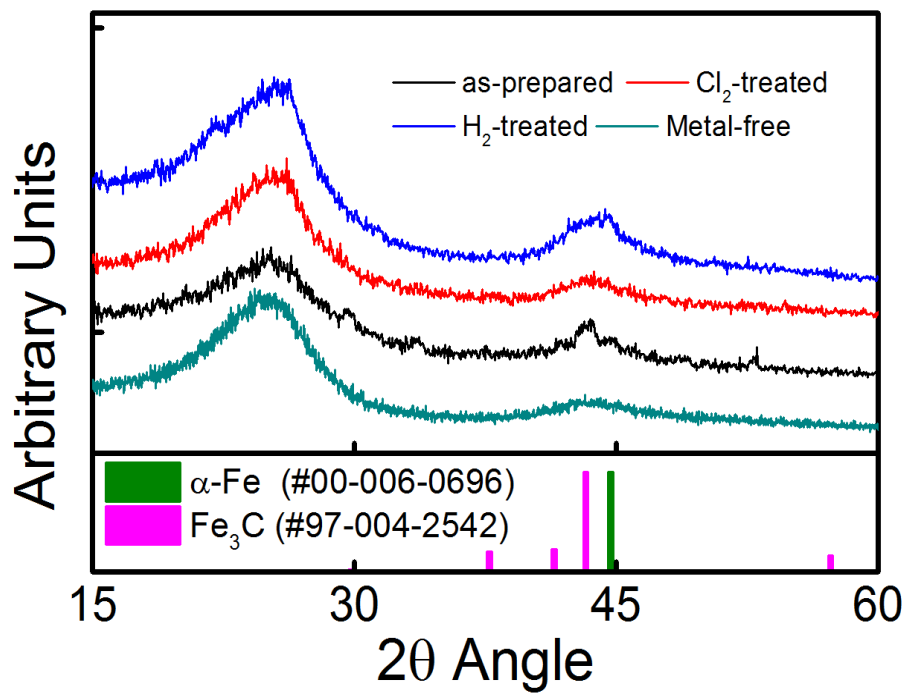


Figure 2.25 Powder XRD of as-prepared and treated Fe-containing catalysts and as-prepared metal-free catalyst. Strong signal from carbon support is observed with small peaks from disordered Fe species observed in the as-prepared and H<sub>2</sub>-treated catalysts.

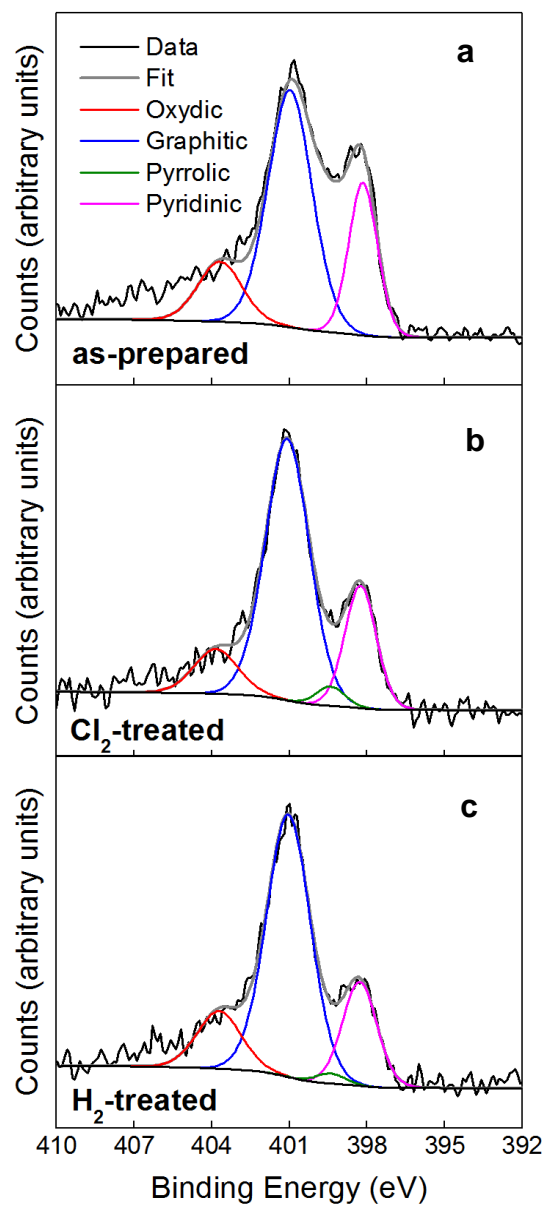


Figure 2.26 N 1s XPS spectra and peak fitting of as-prepared, Cl<sub>2</sub>-treated, and H<sub>2</sub>-treated catalysts showing the presence of oxydic (red), graphitic (blue), pyrrolic (green), and pyridinic (pink) N species.

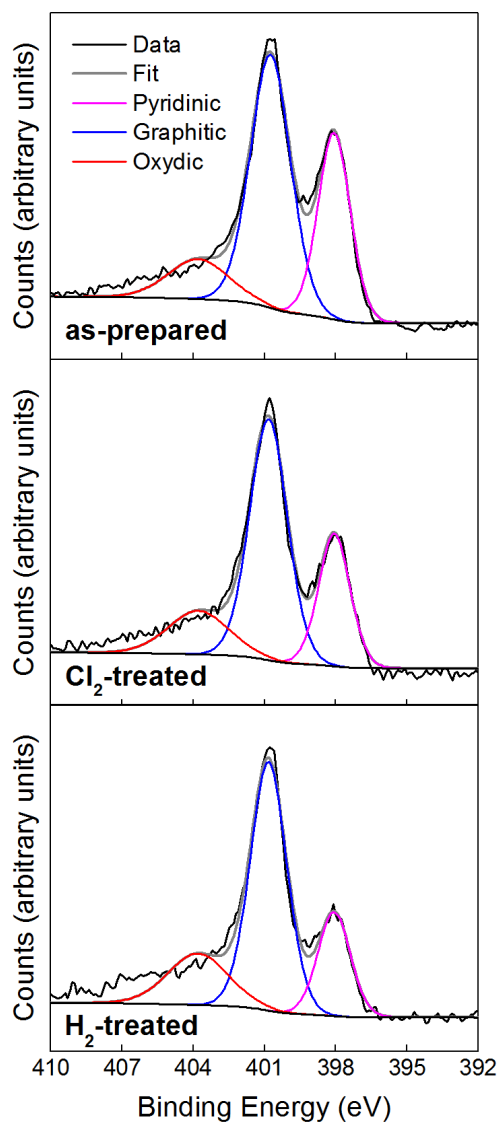


Figure 2.27 N 1s XPS spectra and peak fitting of as-prepared, Cl<sub>2</sub>-treated, and H<sub>2</sub>-treated metal-free catalysts.

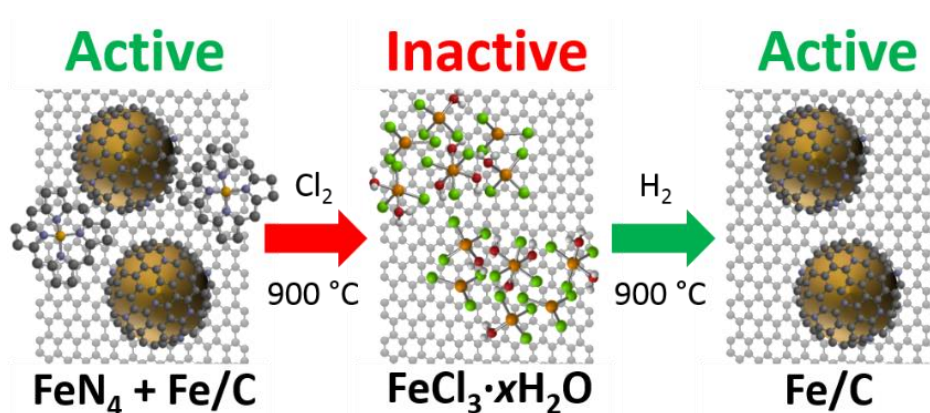


Figure 2.28 Fe species identified in each catalyst demonstrating the selective removal of FeN<sub>4</sub> sites and formation of encapsulated Fe nanoparticles in the H<sub>2</sub>-treated catalyst.

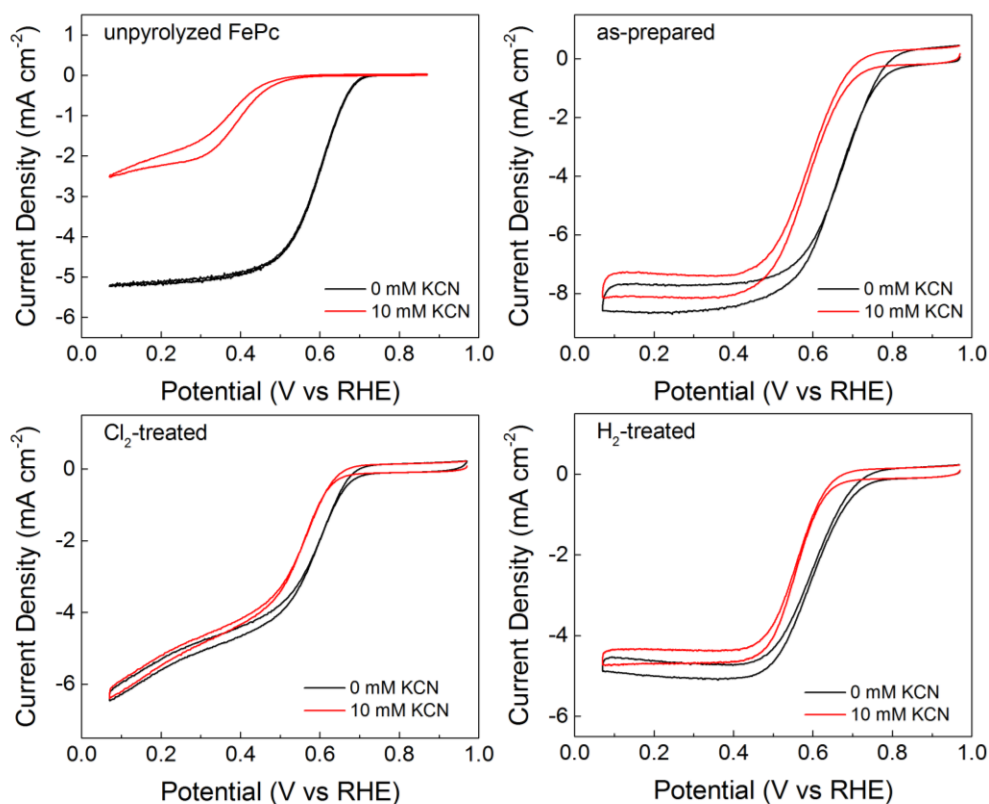


Figure 2.29 Cyclic voltammograms demonstrating the poisoning of ORR activity for all catalysts with 10 mM KCN in 0.1 M NaOH.



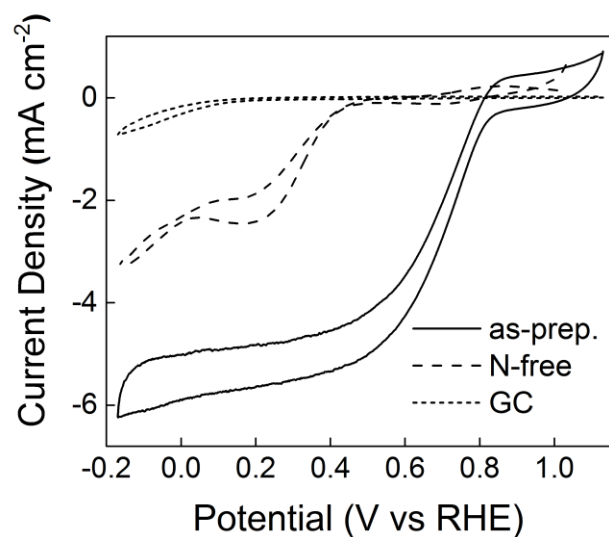


Figure 2.30 Cyclic voltammograms of ORR on as-prepared catalyst, N-free catalyst, and glassy carbon in 0.1 M HClO<sub>4</sub>.

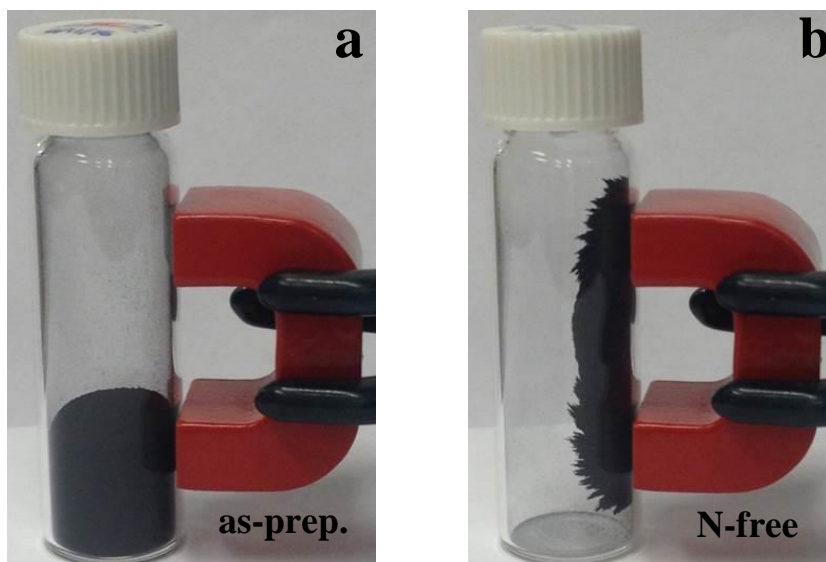


Figure 2.31 As-prepared (a) and N-free (b) catalysts in the presence of a magnetic field. The strong magnetic property of the N-free catalyst indicates that it is composed of material capable of forming large magnetic domains. In the as-prepared catalyst, the absence of magnetic domains indicates that it contains small, reduced Fe particles encapsulated within the carbon.

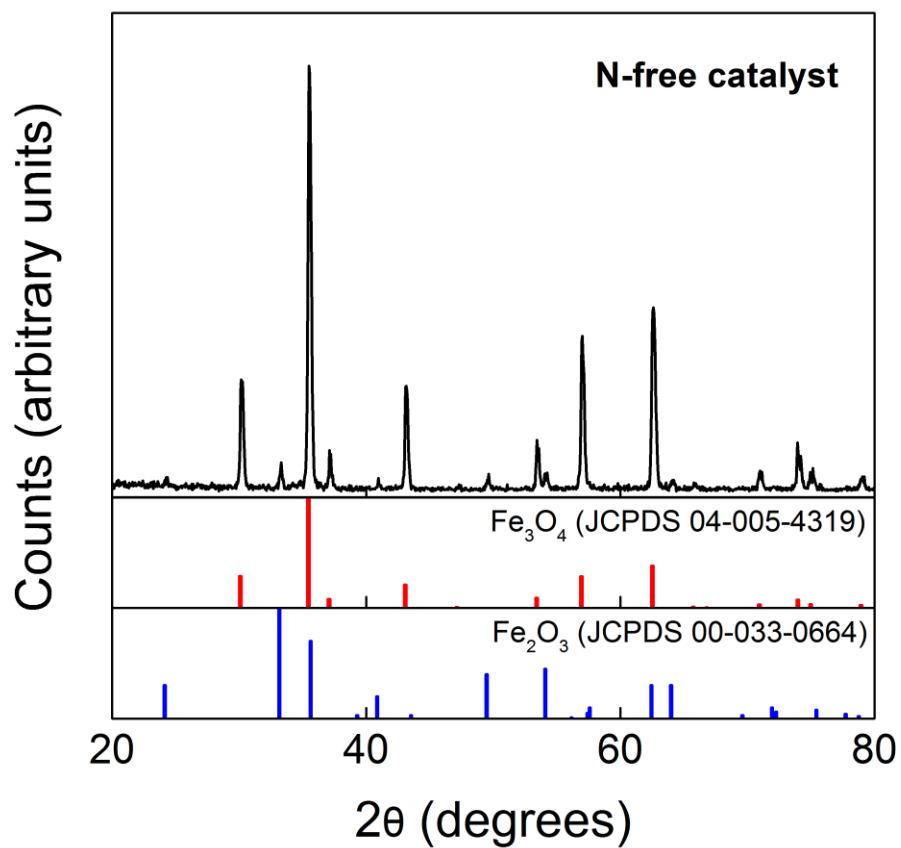


Figure 2.32 Powder XRD of N-free catalyst. Diffraction bands are assigned to magnetite ( $\text{Fe}_3\text{O}_4$ ) and hematite ( $\text{Fe}_2\text{O}_3$ ). Average crystallite size is  $49.7 \pm 1.6$  nm using FWHM.

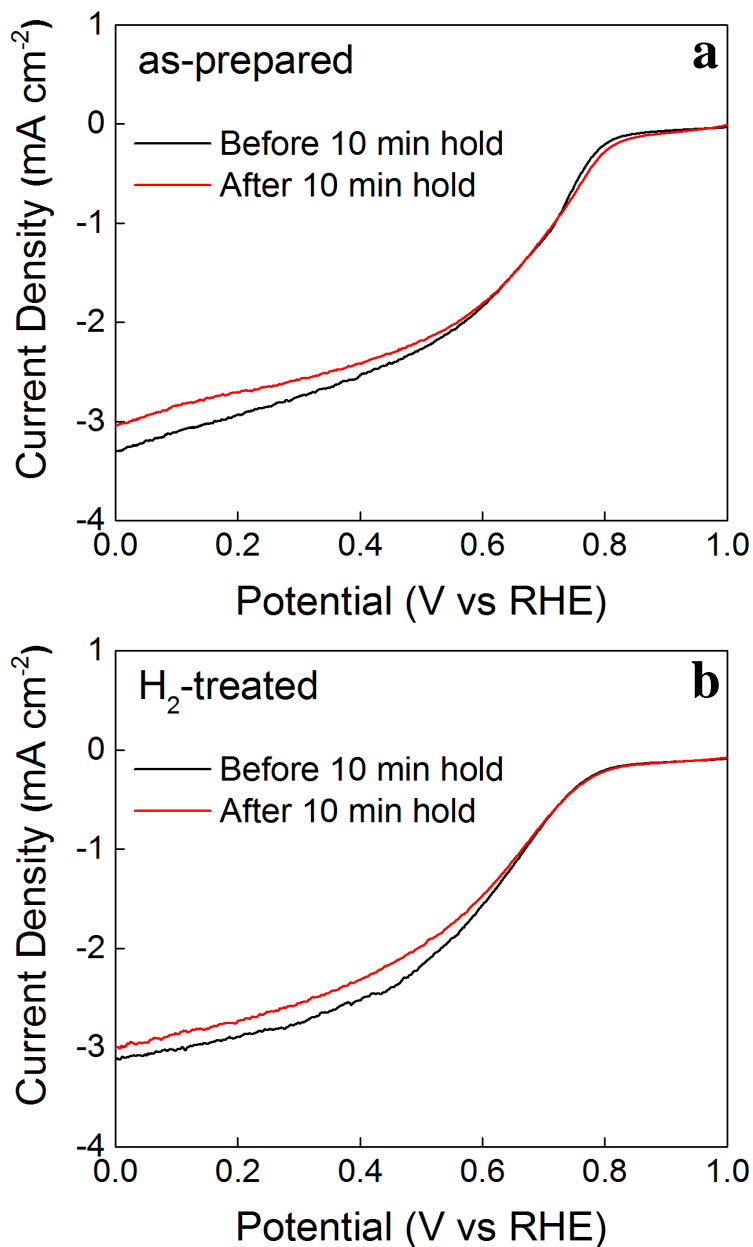


Figure 2.33 Cyclic voltammograms of ORR on as-prepared (a) and H<sub>2</sub>-treated (b) catalysts before and after a potential hold at 0.2 V vs RHE in 0.1 M HClO<sub>4</sub>. Results indicate that ORR activity is not significantly altered during and following operation at oxygen reducing potential. A small decrease in current was observed due to the possible loss of catalyst material or a small number of active species while rotating.

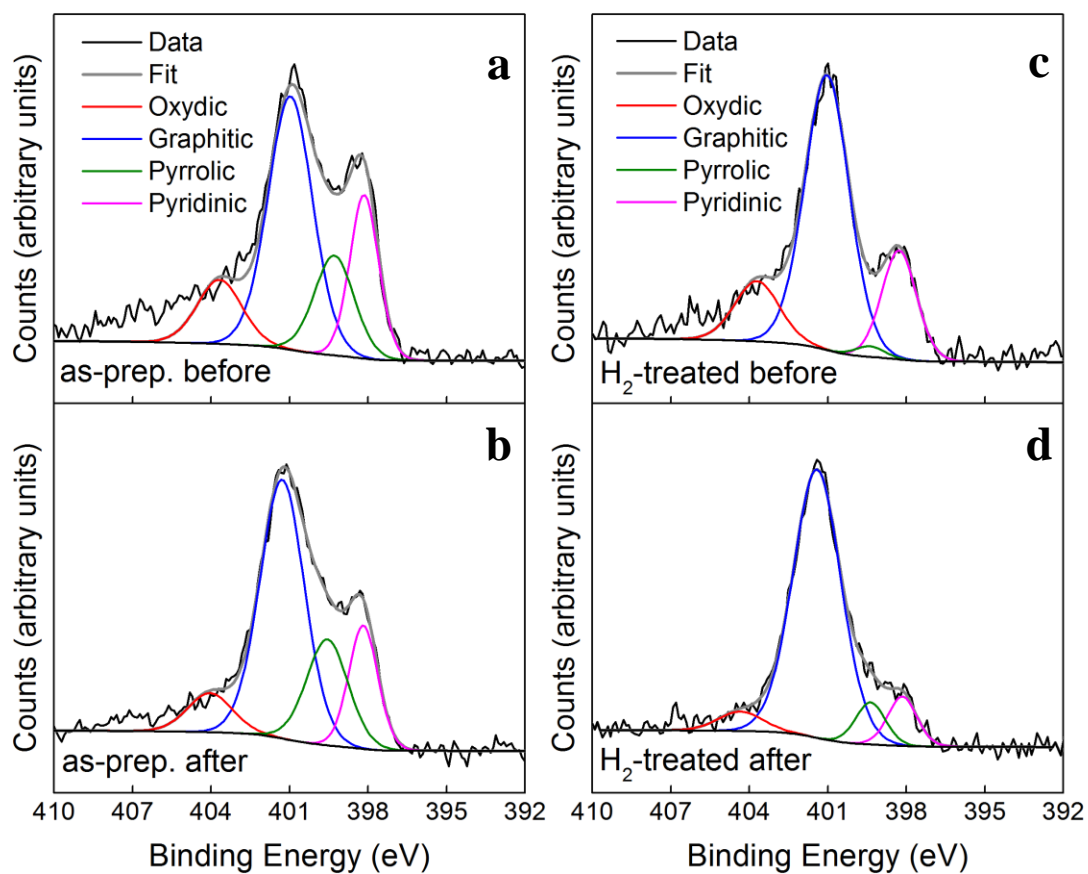


Figure 2.34 N 1s spectra of the as-prepared catalyst (left) and H<sub>2</sub>-treated catalyst (right) before (a, c) and after (b, d) a potential hold at 0.2 V versus RHE for 10 minutes in 0.1 M HClO<sub>4</sub>.

Changes in the pyrrolic and pyridinic bands indicate that these species do not actively participate in the ORR as no significant changes in activity were observed during operation using cyclic voltammetry.

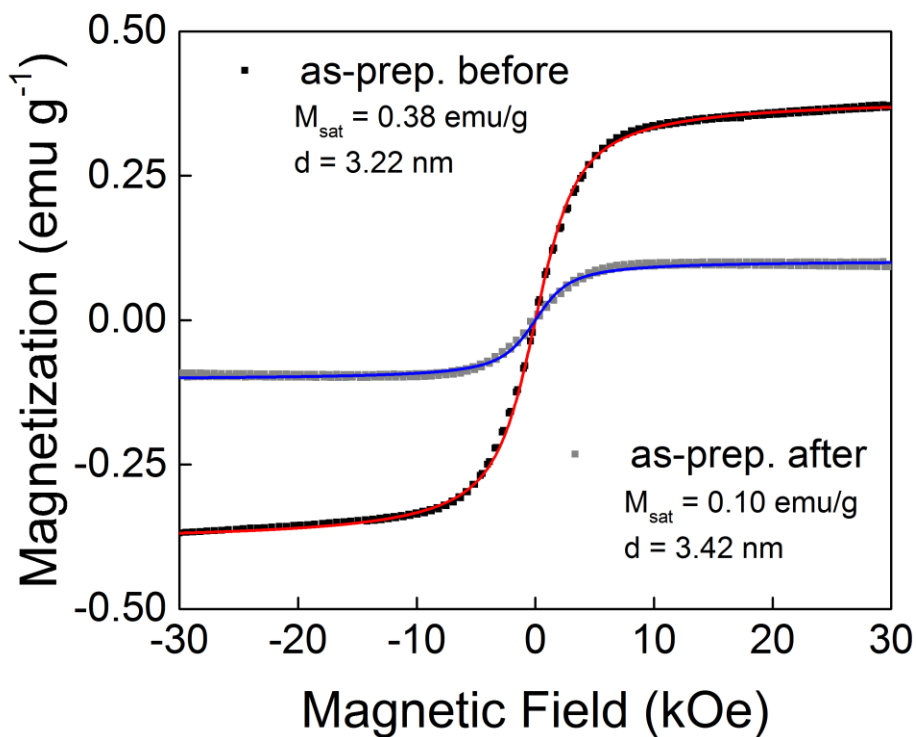


Figure 2.35 VSM data for the as-prepared catalyst before and after a potential hold at 0.2 V versus RHE for 10 minutes in 0.1 M HClO<sub>4</sub>. The decrease in magnetization observed results from the dissolution of metallic species at the surface which are inactive for ORR. After operation the sigmoidal signal of superparamagnetic species is still present indicating that some particles are encapsulated and protected by carbon. Data was fitted using the Langevin equation for superparamagnetic materials to give particle size.

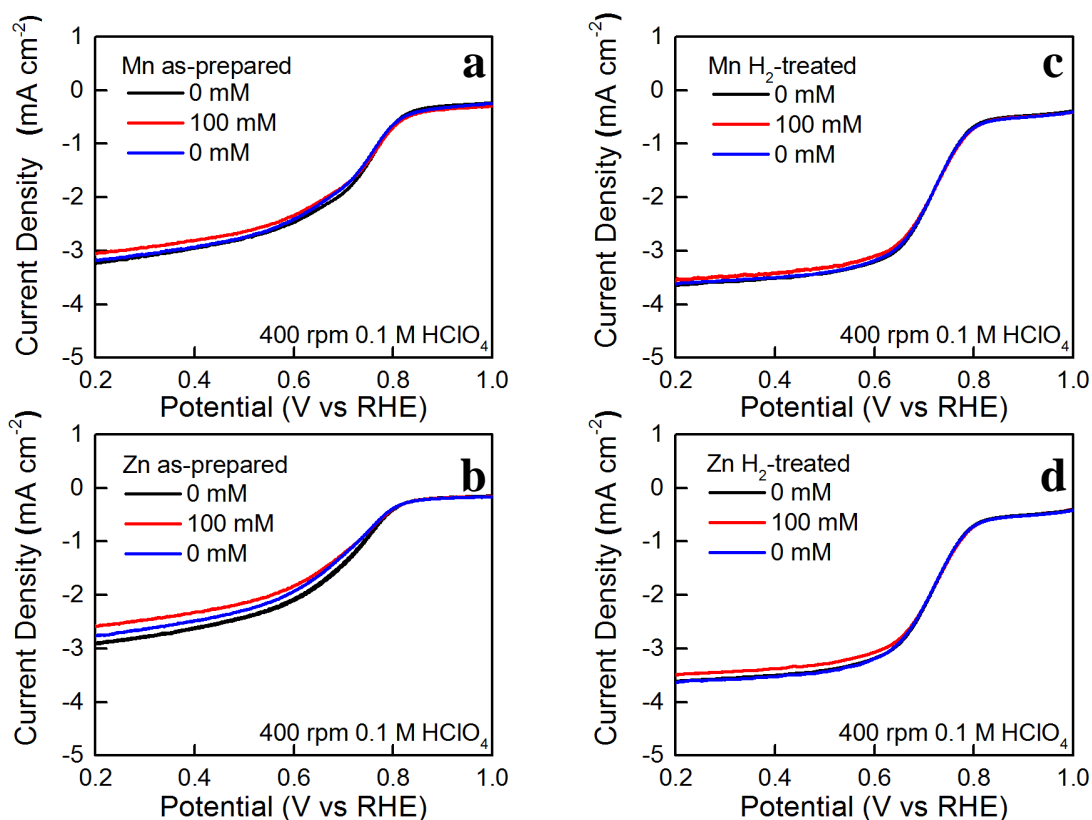


Figure 2.36 Linear sweep voltammograms of ORR on as-prepared (a-b) and H<sub>2</sub>-treated catalysts (c-d) in 0.1 M HClO<sub>4</sub> before and after addition of 100 mM ZnClO<sub>4</sub> or MnClO<sub>4</sub> and after rinsing and introducing fresh electrolyte absent Zn and Mn. In order to eliminate the possibility of a new active form of the catalyst being formed upon introduction of the catalyst to the electrolyte ORR inactive metals were introduced into solution. The high concentration of these metal ions should prevent putative dissolved Fe from coordinating to the catalyst surface, perhaps at pyridinic N sites. This result, in addition to the evidence that FeN<sub>4</sub> sites are not present in the H<sub>2</sub>-treated catalyst, proves that Fe species formed during operation cannot be the source of ORR activity in the catalysts studied. Small changes in the diffusion limited current were observed due to the decrease in solubility of oxygen in solutions with high salt concentration and from the possible loss of catalyst material or a small number of active species while rotating.<sup>55</sup>

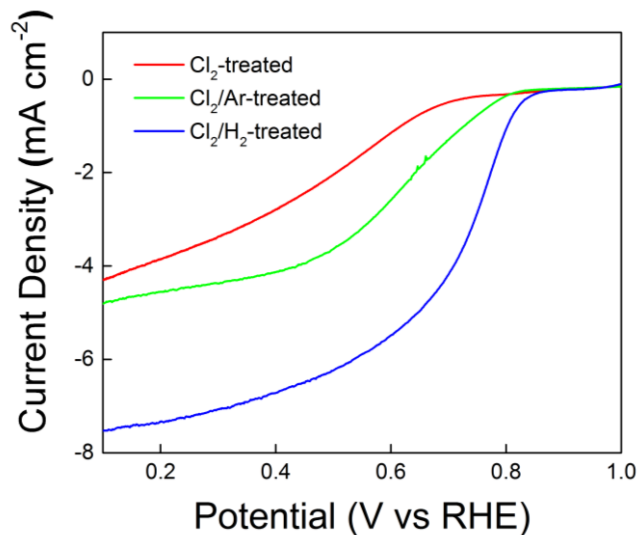


Figure 2.37 Cyclic voltammograms for control treatment of Cl<sub>2</sub>-treated catalyst with Ar at 900 °C. An increase in activity was observed, however complete recovery of catalyst activity is only observed when using H<sub>2</sub>. This demonstrates the need for a reducing treatment to restore activity.

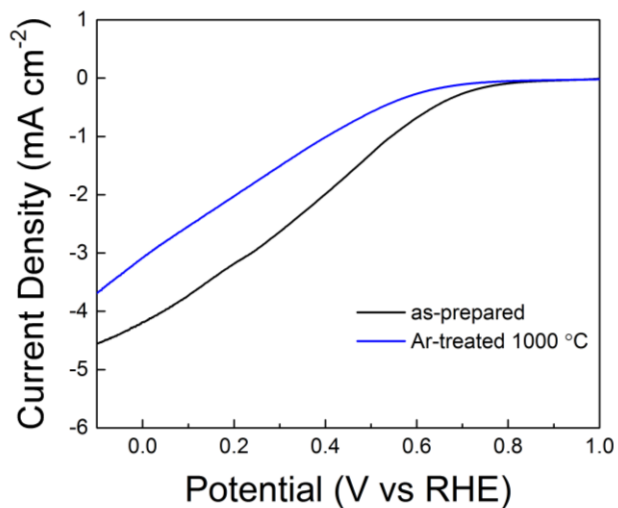


Figure 2.38 Cyclic voltammograms for the control treatment of as-prepared catalyst in Ar at 1000 °C. Deactivation of the catalyst was observed which is attributed to the destruction of the active species due to the temperature above that used during catalyst synthesis. In order to prevent similar effects, gas treatments were carried out at 900 °C and below.

Table 2.1 Catalyst selectivity for the reduction of oxygen.

<b>Sample</b>	<b>H<sub>2</sub>O<sub>2</sub>% (0.3 V vs RHE)</b>
as-prepared	1.59
Cl <sub>2</sub> -treated	4.95
H <sub>2</sub> -treated	1.83

Table 2.2 Fe content determined using ICP-OES, Cl content using ion selective electrode, and N content from CHN analysis. Note that the wt% of Fe in the H<sub>2</sub>-treated sample is greater than in the other samples in part due to a decrease in total mass cause by the removal of Cl and etching of C during the treatment.

<b>Sample</b>	<b>Fe (wt%)</b>	<b>Cl (wt%)</b>	<b>N (wt%)</b>
as-prepared	1.61	0.15	3.39
Cl <sub>2</sub> -treated	0.72	8.12	2.15
H <sub>2</sub> -treated	2.07	0.06	2.49



Table 2.3 Values of Mössbauer fitting obtained for sample spectra for isomer shift ( $\delta_{iso}$ ), quadrupole splitting ( $\Delta E_Q$ ), internal magnetic field ( $\Delta H_{int}$ ) and full-width at half-max (fwhm). Assignments were made by comparing to previous work.






Component	Color	$\delta_{iso}/$ $\text{mm s}^{-1}$	$\Delta E_Q/$ $\text{mm s}^{-1}$	$\Delta H_{int}/$ <b>T</b>	fwhm/ $\text{mm s}^{-1}$	Assignment	Ref.
Doublet 1		0.34	0.95	-	0.8825	FeN <sub>4</sub> / FeN <sub>2+2</sub>	16,23,24,26,27,34,39,56
Doublet 2		0.12	0.32	-	0.3653	Fe <sub>x</sub> N x < 2	23,39,57,58
Sextet 1		0.18	-	19.2	0.4744	Fe <sub>3</sub> C	16,26,56,59
Sextet 2		0.00	-	32.9	0.4579	$\alpha$ -Fe	26,27
Singlet 1		-0.10	-	-	0.4176	spm $\alpha$ -Fe	16,24,27,34,39,59

Table 2.4 Values of Mössbauer fitting for isomer shift ( $\delta_{iso}$ ) and internal magnetic field ( $\Delta H_{int}$ ) for Fe<sub>3</sub>S<sub>4</sub> observed in sample treated with H<sub>2</sub> at 600 °C.


Component	Color	$\delta_{iso}/$ $\text{mm s}^{-1}$	$\Delta H_{int}/$ <b>T</b>	Assignment	Ref.
Sextet		0.8	31.0	Fe <sub>3</sub> S <sub>4</sub>	16

Table 2.5 Best fit structural parameters obtained from the analysis of EXAFS data. Interatomic distances  $R$ , MSD factors  $\sigma^2$  and coordination numbers for the nearest coordination shells for NPM material after  $\text{Cl}_2$  (top) and  $\text{H}_2$  (bottom) treatments and for reference materials. In the parentheses the uncertainty of the last digit is given.

	$R_0$ (Å)	$R_{\text{Cl}}$ (Å)	$\sigma_0^2$ (Å <sup>2</sup> )	$\sigma_{\text{Cl}}^2$ (Å <sup>2</sup> )	$N_0$	$N_{\text{Cl}}$
<b>FeCl<sub>3</sub>·xH<sub>2</sub>O</b>	2.09(5)	2.22(1)	0.002(3)	0.002(3)	1.6(9)	2
<b>Cl<sub>2</sub>-treated</b>	2.2(1)	2.22(2)	0.005(3)	0.005(3)	2(1)	4(1)
	$R_1$ (Å)	$R_2$ (Å)	$R_3$ (Å)	$R_4$ (Å)	$R_5$ (Å)	
<b>Iron foil</b>	2.47(1)	2.85(1)	4.03(1)	4.73(1)	4.94(1)	
<b>H<sub>2</sub>-treated</b>	2.48(1)	2.87(1)	4.05(1)	4.75(1)	4.97(1)	
	$\sigma_1^2$ (Å <sup>2</sup> )	$\sigma_2^2$ (Å <sup>2</sup> )	$\sigma_3^2$ (Å <sup>2</sup> )	$\sigma_4^2$ (Å <sup>2</sup> )	$\sigma_5^2$ (Å <sup>2</sup> )	
<b>Iron foil</b>	0.004(1)	0.005(1)	0.007(2)	0.010(1)	0.004(1)	
<b>H<sub>2</sub>-treated</b>	0.005(1)	0.007(5)	0.014(6)	0.006(4)	0.012(4)	
	$N_1$	$N_2$	$N_3$	$N_4$	$N_5$	
<b>Iron foil</b>	8	6	12	24	8	
<b>H<sub>2</sub>-treated</b>	5.7(8)	3(2)	12(6)	9(6)	3(3)	

Table 2.6 N 1s XPS fitted peak locations and assignment of N species. Range reflects peak locations for all samples shown in this work.

<b>Peak Location</b>	<b>Species Assignment</b>
403.7 – 404.3	Oxydic
401.0 – 401.4	Graphitic
399.3 – 399.6	Pyrrolic
398.1 – 398.3	Pyridinic

Table 2.7 CHN elemental analysis of N-free catalyst material.

<b>Sample</b>	<b>C (wt%)</b>	<b>H (wt%)</b>	<b>N (wt%)</b>
N-free	0.05	0.00	0.03

Table 2.8 A comparison of Cl removal using treatment with either H<sub>2</sub> or Ar at 900 °C for 30 min.

<b>Sample</b>	<b>Cl content (wt%)</b>
as-prepared	0.96
Cl <sub>2</sub> -treated	9.34
Cl <sub>2</sub> /Ar-treated	1.49
Cl <sub>2</sub> /H <sub>2</sub> -treated	0.75

## 2.6 References

- (1) Stamenkovic, V. R.; Fowler, B.; Mun, B. S.; Wang, G.; Ross, P. N.; Lucas, C. A.; Marković, N. M. *Science* **2007**, *315*, 493.
- (2) Gewirth, A. A.; Thorum, M. S. *Inorg. Chem.* **2010**, *49*, 3557.
- (3) Jasinski, R. *Nature* **1964**, *201*, 1212.
- (4) van Veen, J. A. R.; van Baar, J. F.; Kroese, K. J. *J. Chem. Soc., Faraday Trans. 1 F* **1981**, *77*, 2827.
- (5) Gojković, S. L.; Gupta, S.; Savinell, R. F. *J. Electroanal. Chem.* **1999**, *462*, 63.
- (6) Scherson, D.; Tanaka, A. A.; Gupta, S. L.; Tryk, D.; Fierro, C.; Holze, R.; Yeager, E. B.; Lattimer, R. P. *Electrochim. Acta* **1986**, *31*, 1247.
- (7) Lalande, G.; Côté, R.; Guay, D.; Dodelet, J. P.; Weng, L. T.; Bertrand, P. *Electrochim. Acta* **1997**, *42*, 1379.
- (8) Faubert, G.; Côté, R.; Guay, D.; Dodelet, J. P.; Dénès, G.; Poleunis, C.; Bertrand, P. *Electrochim. Acta* **1998**, *43*, 1969.
- (9) Gupta, S.; Tryk, D.; Bae, I.; Aldred, W.; Yeager, E. *J Appl Electrochem* **1989**, *19*, 19.
- (10) Meng, H.; Larouche, N.; Lefèvre, M.; Jaouen, F.; Stansfield, B.; Dodelet, J.-P. *Electrochim. Acta* **2010**, *55*, 6450.
- (11) Proietti, E.; Jaouen, F.; Lefèvre, M.; Larouche, N.; Tian, J.; Herranz, J.; Dodelet, J.-P. *Nat. Commun.* **2011**, *2*, 416.
- (12) Médard, C.; Lefèvre, M.; Dodelet, J. P.; Jaouen, F.; Lindbergh, G. *Electrochim. Acta* **2006**, *51*, 3202.

- (13) Li, Q.; Wu, G.; Cullen, D. A.; More, K. L.; Mack, N. H.; Chung, H. T.; Zelenay, P. *ACS Catal.* **2014**, *4*, 3193.
- (14) Wu, G.; Chen, Z.; Artyushkova, K.; Garzon, F. H.; Zelenay, P. *ECS Trans.* **2008**, *16*, 159.
- (15) Wu, G.; More, K. L.; Johnston, C. M.; Zelenay, P. *Science* **2011**, *332*, 443.
- (16) Ferrandon, M.; Kropf, A. J.; Myers, D. J.; Artyushkova, K.; Kramm, U.; Bogdanoff, P.; Wu, G.; Johnston, C. M.; Zelenay, P. *J. Phys. Chem. C* **2012**, *116*, 16001.
- (17) Oberst, J. L.; Thorum, M. S.; Gewirth, A. A. *J. Phys. Chem. C* **2012**, *116*, 25257.
- (18) Thorum, M. S.; Hankett, J. M.; Gewirth, A. A. *J. Phys. Chem. Lett.* **2011**, *2*, 295.
- (19) Tylus, U.; Jia, Q.; Strickland, K.; Ramaswamy, N.; Serov, A.; Atanassov, P.; Mukerjee, S. *J. Phys. Chem. C* **2014**, *118*, 8999.
- (20) Faubert, G.; Lalande, G.; Côté, R.; Guay, D.; Dodelet, J. P.; Weng, L. T.; Bertrand, P.; Dénès, G. *Electrochim. Acta* **1996**, *41*, 1689.
- (21) Lalande, G.; Faubert, G.; Côté, R.; Guay, D.; Dodelet, J. P.; Weng, L. T.; Bertrand, P. *J. Power Sources* **1996**, *61*, 227.
- (22) Faubert, G.; Côté, R.; Dodelet, J. P.; Lefèvre, M.; Bertrand, P. *Electrochim. Acta* **1999**, *44*, 2589.
- (23) Kramm, U. I.; Herranz, J.; Larouche, N.; Arruda, T. M.; Lefevre, M.; Jaouen, F.; Bogdanoff, P.; Fiechter, S.; Abs-Wurmbach, I.; Mukerjee, S.; Dodelet, J.-P. *PCCP* **2012**, *14*, 11673.
- (24) Kramm, U. I.; Abs-Wurmbach, I.; Fiechter, S.; Herrmann, I.; Radnik, J.; Bogdanoff, P. *ECS Trans.* **2009**, *25*, 93.

- (25) Jaouen, F.; Lefèvre, M.; Dodelet, J.-P.; Cai, M. *J. Phys. Chem. B* **2006**, *110*, 5553.
- (26) Zitolo, A.; Goellner, V.; Armel, V.; Sougrati, M.-T.; Mineva, T.; Stievano, L.; Fonda, E.; Jaouen, F. *Nat. Mater.* **2015**, *14*, 937.
- (27) Kramm, U. I.; Abs-Wurmbach, I.; Herrmann-Geppert, I.; Radnik, J.; Fiechter, S.; Bogdanoff, P. *J. Electrochem. Soc.* **2011**, *158*, B69.
- (28) Matter, P. H.; Wang, E.; Millet, J.-M. M.; Ozkan, U. S. *J. Phys. Chem. C* **2007**, *111*, 1444.
- (29) Deng, D.; Yu, L.; Chen, X.; Wang, G.; Jin, L.; Pan, X.; Deng, J.; Sun, G.; Bao, X. *Angew. Chem., Int. Ed.* **2013**, *52*, 371.
- (30) Strickland, K.; Miner, E.; Jia, Q.; Tylus, U.; Ramaswamy, N.; Liang, W.; Sougrati, M.-T.; Jaouen, F.; Mukerjee, S. *Nat. Commun.* **2015**, *6*.
- (31) Kramm, U. I.; Herrmann-Geppert, I.; Behrends, J.; Lips, K.; Fiechter, S.; Bogdanoff, P. *J. Am. Chem. Soc.* **2016**, *138*, 635.
- (32) von Deak, D.; Singh, D.; Biddinger, E. J.; King, J. C.; Bayram, B.; Miller, J. T.; Ozkan, U. S. *J. Catal.* **2012**, *285*, 145.
- (33) Singh, D.; Tian, J.; Mamtani, K.; King, J.; Miller, J. T.; Ozkan, U. S. *J. Catal.* **2014**, *317*, 30.
- (34) Koslowski, U. I.; Abs-Wurmbach, I.; Fiechter, S.; Bogdanoff, P. *The Journal of Physical Chemistry C* **2008**, *112*, 15356.
- (35) Birry, L.; Zagal, J. H.; Dodelet, J.-P. *Electrochem. Commun.* **2010**, *12*, 628.
- (36) S. Gupta, C. F., E. Yeager *J. Electroanal. Chem. Interfacial Electrochem.* **1991**, *306*, 239.

- (37) Collman, J. P.; Brauman, J. I.; Halbert, T. R.; Suslick, K. S. *Proceedings of the National Academy of Sciences* **1976**, *73*, 3333.
- (38) Collman, J. P.; Dey, A.; Barile, C. J.; Ghosh, S.; Decréau, R. A. *Inorg. Chem.* **2009**, *48*, 10528.
- (39) Kramm, U. I.; Herrmann-Geppert, I.; Bogdanoff, P.; Fiechter, S. *J. Phys. Chem. C* **2011**, *115*, 23417.
- (40) Ambrosi, A.; Chua, C. K.; Khezri, B.; Sofer, Z.; Webster, R. D.; Pumera, M. *Proc. Natl. Acad. Sci.* **2012**, *109*, 12899.
- (41) Pumera, M. *Langmuir* **2007**, *23*, 6453.
- (42) Mercier, G.; Herold, C.; Mareche, J.-F.; Cahen, S.; Gleize, J.; Ghanbaja, J.; Lamura, G.; Bellouard, C.; Vigolo, B. *New J. Chem.* **2013**, *37*, 790.
- (43) Chng, E. L. K.; Poh, H. L.; Sofer, Z.; Pumera, M. *Phys. Chem. Chem. Phys.* **2013**, *15*, 5615.
- (44) Drago, R. S. *Physical methods in chemistry*; Saunders: Philadelphia :, 1977.
- (45) Lind, M. D. *The Journal of Chemical Physics* **1967**, *47*, 990.
- (46) Newville, M.; Ravel, B.; Haskel, D.; Rehr, J. J.; Stern, E. A.; Yacoby, Y. *Physica B Cond. Matter* **1995**, *208–209*, 154.
- (47) Ankudinov, A. L.; Ravel, B.; Rehr, J. J.; Conradson, S. D. *Phys. Rev. B* **1998**, *58*, 7565.
- (48) Frenkel, A. *J. Synchrotron Rad.* **1999**, *6*, 293.
- (49) Tavakkoli, M.; Kallio, T.; Reynaud, O.; Nasibulin, A. G.; Johans, C.; Sainio, J.; Jiang, H.; Kauppinen, E. I.; Laasonen, K. *Angew. Chem., Int. Ed.* **2015**, *54*, 4535.

- (50) Chen, L.; Chen, Z. X.; Huang, Z.; Huang, Z. Y.; Wang, Y. F.; Li, H. X.; Zhou, H. H.; Kuang, Y. F. *J. Phys. Chem. C* **2015**, *119*, 28757.
- (51) Guo, D.; Shibuya, R.; Akiba, C.; Saji, S.; Kondo, T.; Nakamura, J. *Science* **2016**, *351*, 361.
- (52) Herranz, J.; Jaouen, F.; Lefèvre, M.; Kramm, U. I.; Proietti, E.; Dodelet, J.-P.; Bogdanoff, P.; Fiechter, S.; Abs-Wurmbach, I.; Bertrand, P.; Arruda, T. M.; Mukerjee, S. *The Journal of Physical Chemistry C* **2011**, *115*, 16087.
- (53) Kappen, P.; Rider, A.; Pigram, P. J.; Brack, N. *J. Phys. Chem. C* **2011**, *115*, 21083.
- (54) Taubert, S.; Laasonen, K. *Phys. Chem. Chem. Phys.* **2014**, *16*, 3648.
- (55) Battino, R.; Rettich, T. R.; Tominaga, T. *J. Phys. Chem. Ref. Data* **1983**, *12*, 163.
- (56) Blomquist, J.; Lang, H.; Larsson, R.; Widelov, A. *Journal of the Chemical Society, Faraday Transactions* **1992**, *88*, 2007.
- (57) Borsa, D. M.; Boerma, D. O. *Hyperfine Interact.* **2003**, *151-152*, 31.
- (58) Schaaf, P. *Prog. Mater. Sci.* **2002**, *47*, 1.
- (59) Schulenburg, H.; Stankov, S.; Schünemann, V.; Radnik, J.; Dorbandt, I.; Fiechter, S.; Bogdanoff, P.; Tributsch, H. *J. Phys. Chem. B* **2003**, *107*, 9034.



## Chapter 3

### Revealing the Role of the Metal in Non-Precious Metal Catalysts for Oxygen Reduction via Selective Removal of Fe

Reprinted with permission from Varnell, J.A., Sotiropoulos, J.S., Brown, T.M., Subedi, K., Haasch, R.T., Schulz, C.E., Gewirth, A.A *ACS Energy Lett.* 2018, 3, 823-828. Copyright 2018 American Chemical Society.

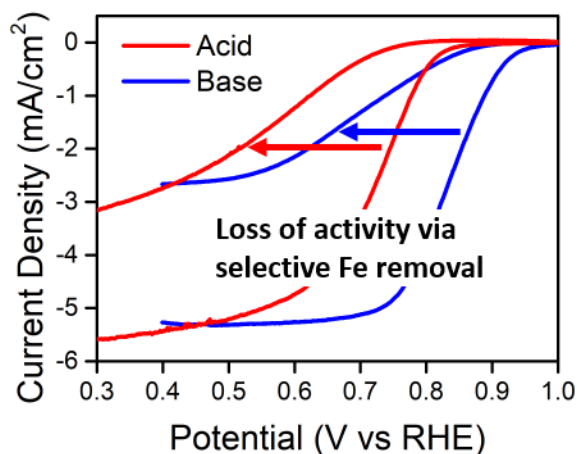


Figure 3.1 Graphical summary of the experimental results described in this work.

### 3.1 Introduction

The oxygen reduction reaction (ORR) is a fundamental process occurring at the cathode of PEM fuel cells. Currently, state-of-the-art catalysts require the use of Pt-alloys which are expensive and limit the widespread application of fuel cells.<sup>1,2</sup> Furthermore, the efficiency of fuel cells is significantly limited due to the nearly 300 mV overpotential exhibited by even the best Pt catalysts.<sup>3</sup> Consequently, the development of ORR catalysts free of precious metals has been the subject of intense research for more than 50 years.<sup>4</sup> For non-precious metal (NPM)

catalysts, there remains much debate as to the nature of the active site. While the need for Fe, N and C precursors is well established in their synthesis, the actual role or direct participation of Fe in the active sites is not well understood.<sup>4</sup> One possibility is that the incorporated metal is directly involved in the active site, possibly in the form of atomic Fe sites coordinated by N<sup>5,6</sup> or encapsulated Fe particles.<sup>6,7</sup> A second possibility is that the Fe present during the catalyst synthesis is responsible for catalyzing the formation of a metal-free C/N active site where the Fe is not directly involved in the active site for oxygen reduction.<sup>8,9</sup> Investigating the possibility of a metal-free active site is difficult given that a metal needs to be present to produce an active catalyst with high selectivity for the 4 e<sup>-</sup> reduction of O<sub>2</sub> to water. Furthermore, previous attempts utilizing acid washing to remove Fe from active catalysts were not able to remove all of the metal and in some cases have actually led to improvements in catalyst activity.<sup>10-12</sup> To date, no work has been able to entirely separate the individual contributions of sites involving metal species and sites that are metal-free within the same catalyst material. Thus, the exact role of the metal in the active site of non-precious metal catalysts remains uncertain.

### **3.2 Results**

In the current work, we report the nearly complete removal of Fe from a NPM catalyst using an acidic treatment aided by the addition of H<sub>2</sub>O<sub>2</sub>. Because washing NPM catalysts with acid alone typically leads to modest changes in activity, we utilized H<sub>2</sub>O<sub>2</sub> to oxidize the carbon in the catalyst and increase the amount of accessible metal species.<sup>10,13-15</sup> We prepared a NPM catalyst with FeCl<sub>3</sub> as the Fe source following a procedure from literature.<sup>16</sup> We then treated the “as-prepared” catalyst in a mixture of H<sub>2</sub>SO<sub>4</sub> and H<sub>2</sub>O<sub>2</sub> to oxidize the catalyst to give the “H<sub>2</sub>O<sub>2</sub>-treated” catalyst. We then pyrolyzed the H<sub>2</sub>O<sub>2</sub>-treated catalyst under N<sub>2</sub> to remove the oxygenic

species left by the acid treatment to give the “H<sub>2</sub>O<sub>2</sub>/N<sub>2</sub>-treated” catalyst. **Table 3.1** summarizes all of the catalysts and treatments used in this work.

**Figure 3.2a** shows the total Fe content of the as-prepared and treated catalysts determined from multiple ICP-OES measurements, along with the untreated Ketjenblack which was also used as a precursor for the as-prepared catalyst. The ICP-OES results show that the H<sub>2</sub>O<sub>2</sub> treatment leads to a more than 95% reduction in the total Fe content in the catalyst. Additionally, XPS confirms the oxidation of carbon resulting from the H<sub>2</sub>O<sub>2</sub> treatment with a relative increase in the magnitude of the O signal at ca. 532 eV in the survey spectrum and the appearance of a carbon-oxygen peak at 288 eV in the C1s region (**Fig. 3.3**). By comparison, a control treatment omitting the addition of H<sub>2</sub>O<sub>2</sub> results in only a ca. 70% loss in Fe content and does not change the carbon structure as evidenced by the lack of a carbon-oxygen peak in the C1s region in the XPS spectrum. The Fe content measured in both the H<sub>2</sub>O<sub>2</sub>-treated and the H<sub>2</sub>O<sub>2</sub>/N<sub>2</sub>-treated catalysts is the same within error as the amount found in as-received Ketjenblack ( $0.047 \pm 0.012$  wt %) and is on the same order of magnitude as that reported for another typical carbon black (ca. 0.01 wt %).<sup>17</sup> No Fe signal was visible in the XPS survey spectra for any of the materials we tested, despite having Fe contents detectable by ICP-OES.

To study the Fe species in each catalyst, we used Mössbauer spectroscopy. **Figures 3.2b-d** show the Mössbauer spectra and fitting of the as-prepared, control-treated, and no-metal-added catalysts. Due to the low Fe content of the H<sub>2</sub>O<sub>2</sub>-treated and H<sub>2</sub>O<sub>2</sub>/N<sub>2</sub>-treated catalysts no identifiable signals were observed using Mössbauer; Ketjenblack (as-received) also exhibited no Mössbauer signal (**Fig. 3.4**). From the Mössbauer fitting it is evident that the as-prepared catalyst contains a mixture of several Fe species, consistent with previous reports.<sup>18,19</sup> The control-treated and no-metal-added catalysts also contain a mixture of several Fe species. The

sextet (seen in **Fig. 3.2b, c**) and singlet (seen in **Fig. 3.2d**) represent reduced Fe species in the form of Fe<sub>3</sub>C and superparamagnetic Fe particles respectively. The doublet species (seen in **Fig. 3.2b-d**) are assigned to different forms of FeN<sub>4</sub> sites. Detailed fitting parameters for the Mössbauer spectra are provided in **Table 3.2**.

To test the ORR activity of each catalyst we used a rotating disk electrode (RDE). **Figure 3.5a** shows linear sweep voltammograms (LSVs) obtained in 0.1M HClO<sub>4</sub> and **Figure 3.5b** shows LSVs obtained in 0.1M NaOH. In both acidic and alkaline conditions the as-prepared catalyst exhibits the highest ORR onset potential. The H<sub>2</sub>O<sub>2</sub>-treated catalyst exhibits almost no ORR activity across the full range of potentials, particularly in acid. This finding is consistent with the carbon oxidation exhibited by this material, shown using XPS in **Figure 3.3**. Studies have shown the detrimental effect of oxidation caused by H<sub>2</sub>O<sub>2</sub> to catalyst performance using ex situ and in operando treatments.<sup>20-23</sup> The H<sub>2</sub>O<sub>2</sub>/N<sub>2</sub>-treated catalyst displays a lower onset potential in both acid and base than the as-prepared catalyst.

For comparison, we measured the activity of the control-treated and no-metal-added catalysts along with as-received Ketjenblack. LSVs of these materials are shown in **Figure 3.5c and 3.5d** in acid and base respectively. Interestingly, the control-treated catalyst in which ca. 70% of the Fe has been removed exhibits activity similar to the as-prepared catalyst. This result suggests that a large portion of the Fe species within the catalyst do not actively contribute towards the ORR activity, consistent with previous work.<sup>10,16</sup> The remaining 30% of the Fe in the control-treated catalyst must include the active species, since the addition of H<sub>2</sub>O<sub>2</sub> to access and remove these species and subsequent N<sub>2</sub> treatment leads to catalyst with lower activity. Due to the heterogeneity observed in the Mössbauer spectra for the catalysts shown in **Figure 3.2**, it is not possible to assign the catalytic activity to a specific type of Fe site. The no-metal-added

catalyst exhibits similar activity to the H<sub>2</sub>O<sub>2</sub>/N<sub>2</sub>-treated catalyst possibly indicating that both catalysts contain a similar type of active site which does not involve Fe. Ketjenblack shows no activity in acid but in base it exhibits an ORR onset slightly below the H<sub>2</sub>O<sub>2</sub>/N<sub>2</sub>-treated and no-metal-added catalysts. The activity of pure carbon in alkaline conditions has been reported elsewhere; Zn-air batteries feature a C-only catalyst that carries out an initial 2e<sup>-</sup> reduction of O<sub>2</sub> in alkaline.<sup>24</sup>

Using Koutecky-Levich analysis we compared the selectivity for the reduction of O<sub>2</sub> to H<sub>2</sub>O of the as-prepared, control-treated, H<sub>2</sub>O<sub>2</sub>/N<sub>2</sub>-treated, and no-metal-added catalysts. **Table 3.3** gives the values of the electron transfer number (n) in acid and base. **Figure 3.6** shows representative LSVs used in the calculation. The value of n is close to 4 for the as-prepared and control-treated catalysts, in agreement with previous work.<sup>16</sup> The n values for the H<sub>2</sub>O<sub>2</sub>/N<sub>2</sub>-treated and no-metal-added catalysts are closer to 3, which indicates the ORR pathway has shifted toward the 2e<sup>-</sup> reduction of O<sub>2</sub> to H<sub>2</sub>O<sub>2</sub> in the absence of Fe. We also verified the electron transfer numbers using RRDE shown in **Figures 3.7-8**. The RRDE experiments also indicate that the as-prepared and control-treated catalysts have a higher n value than the H<sub>2</sub>O<sub>2</sub>/N<sub>2</sub>-treated and no-metal-added catalysts in base, but in acid the n value for the no-metal-added catalyst is similar to that of the as-prepared catalyst. We note that the n values determined using RRDE are higher than those determined using Koutecky-Levich analysis, especially for the H<sub>2</sub>O<sub>2</sub>/N<sub>2</sub>-treated and no-metal-added catalysts. This discrepancy likely arises from the subsequent reduction of H<sub>2</sub>O<sub>2</sub> which is formed on the H<sub>2</sub>O<sub>2</sub>/N<sub>2</sub>-treated and no-metal-added catalysts since it is known that RRDE tends to underestimate the contribution of the 2 x 2 e<sup>-</sup> pathway.<sup>25</sup>

We used XPS in the N 1s region to study the nitrogen species on the surface of the catalysts as shown in **Figure 3.9a**. The spectra for the as-prepared, control-treated, H<sub>2</sub>O<sub>2</sub>/N<sub>2</sub>-treated, and no-metal-added catalysts all exhibit two main peaks at 398 and 401 eV corresponding to pyridinic and graphitic species respectively.<sup>10,26</sup> We note that a small shift in binding energies (ca. 0.2-0.3 eV) is present in the N 1s spectra. While the small shift does not affect the assignment of N species, a similar shift was previously observed and was attributed to the presence and influence of Fe on the N 1s binding energies.<sup>17</sup> **Figure 3.10** shows fitting in the N1s region for the as-prepared, H<sub>2</sub>O<sub>2</sub>/N<sub>2</sub>-treated, and no-metal-added catalysts which exhibit pyridinic N concentrations of 24-35% and graphitic N concentrations of 54-66%. From the fitting, the relative amounts of graphitic and pyridinic N species do not seem to be directly correlated with the ORR activity. The most active catalyst, the as-prepared, exhibits intermediate amounts of both pyridinic and graphitic N. **Figure 3.9b** shows the total N content determined from CHN analysis. From the CHN results it appears that the total N content is also not directly related to catalyst activity. The highest ORR onset potentials are observed for catalysts which contain ca. 3-4% N while the no-metal-added catalyst contains the highest amount of N but exhibits lower activity. The lower N content of the as-prepared and H<sub>2</sub>O<sub>2</sub>/N<sub>2</sub>-treated catalysts as compared to the no-metal-added catalyst is likely caused by the N content in the precursor mixture before pyrolysis and the possible Fe-catalyzed loss of C/N species during pyrolysis. Although we observe no direct correlation between the ORR activity and the total N content or distribution of N species, the incorporation of N, especially graphitic and pyridinic species, is still an important component in NPM catalysts as has been demonstrated previously.<sup>27-29</sup>

### 3.3 Discussion

Our results show definitively that the presence of Fe is the determining factor leading to high ORR activity. Previous work, where Fe content was controlled by Fe addition instead of by subsequent Fe removal as reported here, yielded a similar conclusion.<sup>30</sup> However the specific role of Fe, i.e. whether it is a part of the active site or is just a reagent for active C/N site formation has not been previously addressed. The relationship between the Fe content and ORR onset potential for all of the catalysts tested in our work in both acid and base is shown in **Figures 3.11a and 3.11b** respectively. The plots show a linear increase in onset and Fe content to around 0.2 wt% Fe followed by a leveling off of the activity as Fe content is increased further. The as-prepared and control-treated catalysts, with Fe contents greater than ca. 0.5 wt %, facilitate the 4 e<sup>-</sup> reduction of O<sub>2</sub>. By way of contrast the H<sub>2</sub>O<sub>2</sub>/N<sub>2</sub>-treated and no-metal-added catalysts, with less than ca. 0.2 wt % Fe, exhibit predominately 2e<sup>-</sup> reduction of O<sub>2</sub>. The direct comparison of the as-prepared and H<sub>2</sub>O<sub>2</sub>/N<sub>2</sub>-treated catalyst on this plot again shows that Fe is a necessary constituent in the active site for the ORR in both acid and base and is not just a reagent for active site formation.

To further demonstrate the need to include Fe, we added Fe back into the demetallated catalyst. We found that adding Fe back into the H<sub>2</sub>O<sub>2</sub>-treated catalyst (without pyrolysis) did not restore activity but that by adding Fe and pyrolyzing under Ar (to avoid adding an additional source of N) an onset potential similar to the as-prepared catalyst was achieved (**Fig. 3.12**). This result supports our suggestion that adsorbed or coordinated Fe species on the surface of the catalyst are not active for the ORR and that pyrolysis is necessary to form Fe species that are protected from oxidation and dissolution but yet are close enough to the catalyst surface to remain catalytically active.<sup>31</sup> This possibility is further highlighted by our observation that the

control-treated catalyst remains active despite a ca. 70% loss of Fe in the form of solution-accessible species when the catalyst is treated in acid alone. Therefore, we suggest that the reason the maximum activity is reached for Fe contents between 0.2 wt % and 0.5 wt % is that relatively few Fe sites satisfy the necessary structure to be active within the catalyst. Such structural requirements include the specific form of Fe in the catalyst, the protection of the Fe species from direct interaction with the electrolyte, the distance of the Fe species from the surface of the catalyst, and the proximity of C and N species which are likely a part of the active site along with Fe.

The removal of Fe from an active catalyst allows us to directly compare the role of Fe in similarly prepared materials. Specifically, we reveal that while “metal-free” catalyts with a preponderance of C/N sites do exhibit some ORR activity, they favor the partial reduction of oxygen to H<sub>2</sub>O<sub>2</sub> via a 2 e<sup>-</sup> pathway and do so with greater overpotentials than catalysts with appreciable amounts of metal directly incorporated. This lower activity arises even when a variety of N sites are present. This result agrees with previous work which compared two different catalysts and showed that direct Fe incorporation led to a more active catalyst.<sup>11</sup> That Fe is a requirement for achieving high ORR activity is especially significant given the numerous examples of “metal-free” catalysts in literature.<sup>32-34</sup> We suggest, along with other researchers, that many reported “metal-free” catalysts exhibiting high activity might actually contain enough metal to directly participate in the ORR.<sup>35-38</sup> As we demonstrate here, the use of ICP-OES to measure low Fe concentrations not detectable by routine XPS provides crucial information to understand the locus of activity in NPM and “metal-free” ORR catalysts.<sup>35,37</sup> Additionally, the absence of a Pt counter electrode in this work removes a possible source of Pt contamination and subsequent mechanistic uncertainty.



In summary, we show that the presence of Fe in NPM catalysts contributes directly to their ability to reduce oxygen to water via a 4 e<sup>-</sup> pathway and at lower overpotentials than catalysts featuring C and N sites alone. Catalysts without Fe, even those containing some residual metal, reduce O<sub>2</sub> with larger overpotentials and favor the 2 e<sup>-</sup> pathway for oxygen reduction in both acidic and alkaline conditions. Despite significant progress toward the development of NPM catalysts for the ORR, a more detailed understanding of the active site in NPM catalysts is necessary to help realize their potential as replacements for Pt-based catalysts. The results reported here provide crucial guidance for efforts to understand and synthesize improved NPM ORR catalysts and in so doing will aid in the search for catalysts leading to more affordable and efficient fuel cells in the near future.

### 3.4 Experimental Methods

*General-* Chemicals and starting materials were obtained from commercial sources and used without further purification unless otherwise specified. Water was obtained for synthesis and preparation of electrolytes using a Milli-Q system (>18 mΩ cm, MilliPore).

*Catalyst Synthesis-* The “as-prepared” NPM catalyst was synthesized following a literature procedure from LANL and previously described by our group.<sup>16,31</sup> Ketjenblack EC600J (AkzoNobel) was first treated in 0.1 M HCl (Macron, ACS Reagent) for 24 hours and then treated in 70% HNO<sub>3</sub> (Macron, ACS Reagent) at 80 °C for 8 hours before being filtered, dried, and collected. 2.5 mL of aniline (Sigma-Aldrich, ACS reagent) was pipetted into 500 mL of 2.0 M HCl and the solution was cooled in an ice bath before addition of 10 g of FeCl<sub>3</sub> (Sigma-Aldrich, Reagent) and 5 g of ammonium persulfate (Sigma-Aldrich, ACS Reagent). The mixture was allowed to stir for 3 hours and then 0.4 g of the treated Ketjenblack was added and the resulting mixture stirred for 48 hours. After mixing, all liquid was evaporated under a stream of

N<sub>2</sub> at 80 °C and the dry precursor was crushed into a fine powder using a mortar and pestle. The powder was then weighed into a ceramic boat and pyrolyzed in a tube furnace under flowing N<sub>2</sub> at 900 °C for 3 hours. After the first pyrolysis, the powder was again crushed with a mortar and pestle and washed in approximately 500 mL of 0.5 M H<sub>2</sub>SO<sub>4</sub> (Macron, ACS Reagent) at 80 °C for 8 hours before being filtered out and dried. The dry powder was then pyrolyzed a second time under N<sub>2</sub> at 900 °C giving the “as-prepared” catalyst. The “metal-free” catalyst was prepared according to an identical procedure, without the addition of FeCl<sub>3</sub>.

*Peroxide Treatment-* Caution! Concentrated H<sub>2</sub>SO<sub>4</sub> and H<sub>2</sub>O<sub>2</sub> are strong oxidizers. Extreme care should be taken when performing the peroxide treatment. The “H<sub>2</sub>O<sub>2</sub>-treated” catalyst was prepared by suspending 600 mg of the “as-prepared” catalyst in 200 mL of concentrated H<sub>2</sub>SO<sub>4</sub> in a round bottom flask with stirring using a pyrex stir bar. 200 mL of 30% H<sub>2</sub>O<sub>2</sub> (in water, Macron, ACS Reagent) was then added dropwise over the course of two hours. The suspension was allowed to stir for 8 hours before being filtered and dried to give the final product. The “control-treated” catalyst was prepared following same procedure described above except that 200 mL of water was added dropwise in place of H<sub>2</sub>O<sub>2</sub>.

*Additional N<sub>2</sub> Treatment-* The “H<sub>2</sub>O<sub>2</sub>/N<sub>2</sub>-treated” catalyst was prepared by pyrolyzing the “H<sub>2</sub>O<sub>2</sub>/N<sub>2</sub>-treated” catalyst for 1 hour under N<sub>2</sub> at 900 °C in order to remove oxygenic species.

*Addition of Fe to H<sub>2</sub>O<sub>2</sub>-treated Catalyst-* The H<sub>2</sub>O<sub>2</sub>-treated catalyst was suspended in EtOH. FeCl<sub>3</sub> was added (equivalent to 5 wt% Fe of the added catalyst) and the resulting mixture was sonicated for 10 minutes, evaporated under N<sub>2</sub>, and dried in a vacuum oven for 1 hour. Additionally, some of the catalyst was pyrolyzed under Ar at 900 °C for 1 hour.

*Electrochemical Characterization-* The ORR activity of each catalyst was measured using a rotating disk electrode (RDE) or a rotating ring-disk electrode (RRDE) in a typical 3-compartment electrochemical cell. A graphite rod (Ted Pella) separated by a glass frit was used as the counter electrode and a “no-leak” Ag/AgCl (EDAQ) separated from the working electrode by a Luggin capillary as the reference electrode. The working electrode was a glassy carbon electrode polished sequentially with diamond polish (Buehler). Catalyst inks were prepared using Nafion 117 (Sigma-Aldrich) and EtOH and drop cast onto the glassy carbon disk giving a final catalyst loading of 575  $\mu\text{g}/\text{cm}^2$ . Aqueous solutions were prepared using  $\text{HClO}_4$  (70 wt%, Fisher) and NaOH (10N solution, Amresco, Reagent). Cyclic voltammetry was performed using a CH Instruments 760 D Electrochemical Workstation (Austin, TX) at room temperature. The electrolyte was bubbled with  $\text{O}_2$  or Ar for 15 minutes before cyclic voltammetry was recorded for the  $\text{O}_2$ -saturated and  $\text{O}_2$ -free experiments respectively. The rotation rate of the R(R)DE was controlled using a MSRX rotator (Pine Instruments). All potentials were converted to RHE by monitoring the open-circuit potential of a clean Pt wire in  $\text{H}_2$  saturated electrolyte immediately after testing the ORR activity of catalysts.

*Physical Characterization-* Mössbauer spectra were recorded at 300 K using a constant acceleration spectrometer (Knox College). X-ray photoelectron spectroscopy was performed using a Kratos AXIS Ultra spectrometer equipped with a monochromatic Al  $K\alpha$  (1486.6 eV) X-ray source. All binding energies were referenced to the peak of graphitic carbon observed at 284.5 eV for all samples. Inductively coupled plasma optical emission spectroscopy was carried out on a PerkinElmer ICP-OES (Optima 8300, USA). A mixture of nitric acid (Trace metal grade, 67-70%) and hydrochloric acid (Trace metal grade 34-37%) in the ratio 5:1 was used to initially digest the samples which were further subjected to an automated sequential microwave

digester (Discover SP-D, CEM Corp.) The final clear transparent digest was analyzed by ICP-OES. At least two emission lines were observed for iron and the one with the highest intensity and lowest RSD (Relative Standard Deviation) was used for this study.

### 3.5 Figures and Tables

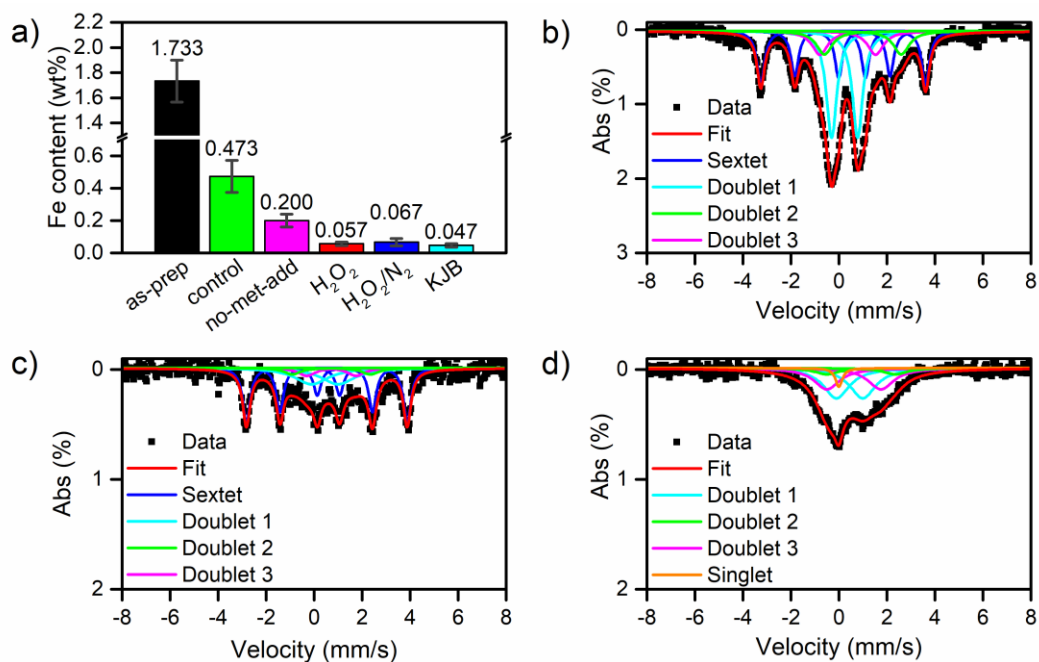


Figure 3.2 Fe content for all catalysts tested as determined from ICP-OES (a) and Mössbauer spectra with fitting of the as-prepared (b), control-treated (c), and no-metal-added (d) catalysts.

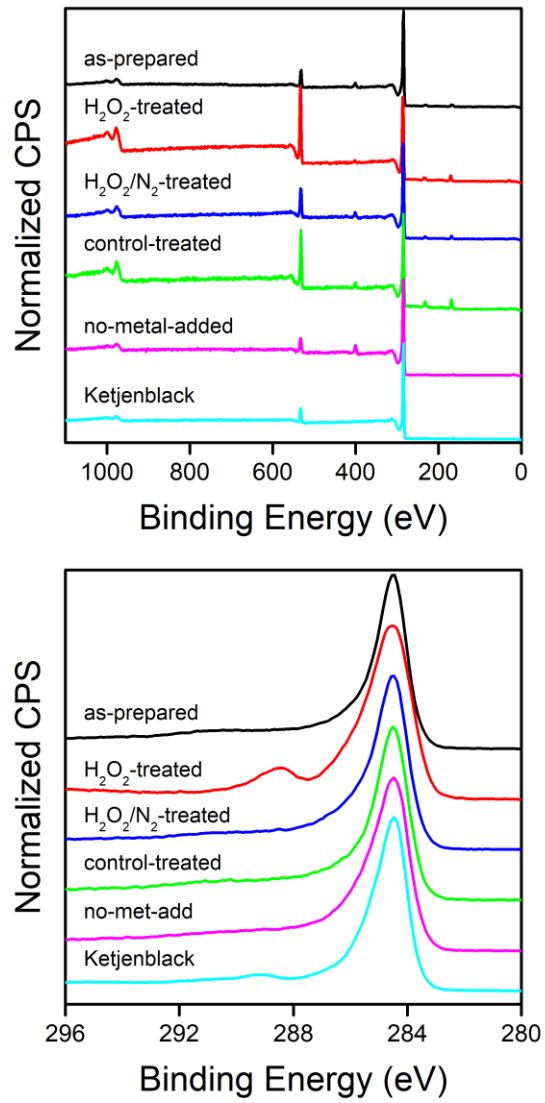


Figure 3.3 XPS survey spectra (top) and spectra from C 1s region (bottom) of catalysts tested.

The peak at 288 eV in the C1s spectrum of the H<sub>2</sub>O<sub>2</sub>-treated catalysts is consistent with the presence of C=O bonds on the surface of the catalyst.<sup>37</sup>

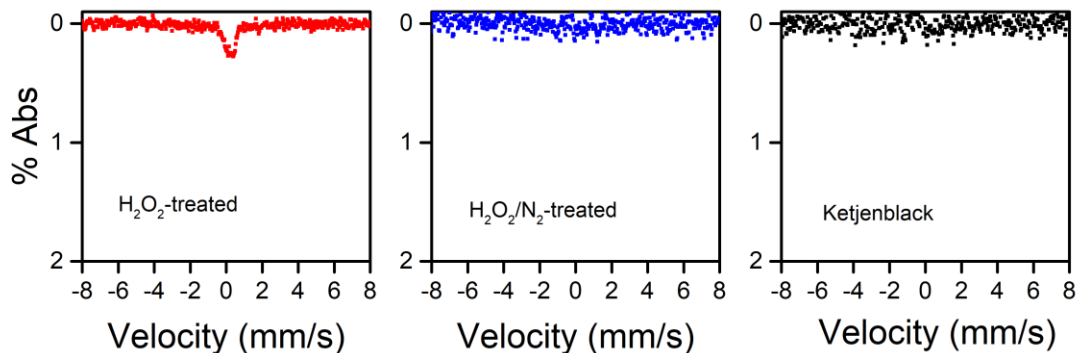


Figure 3.4 Mössbauer spectra of  $\text{H}_2\text{O}_2$ -treated catalyst,  $\text{H}_2\text{O}_2/\text{N}_2$ -treated catalyst, and Ketjenblack.

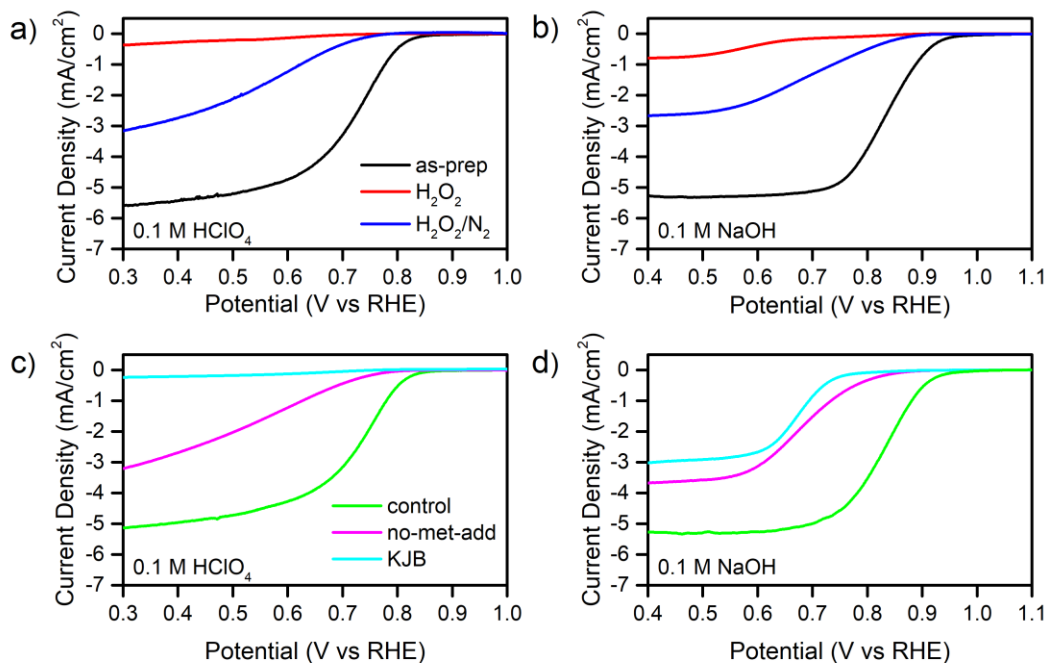


Figure 3.5 Linear sweep voltammograms of the as-prepared,  $\text{H}_2\text{O}_2$ -treated, and  $\text{H}_2\text{O}_2/\text{N}_2$ -treated catalyst in acid (a) and base (b). LSVs of the control-treated catalyst, no-metal-added catalyst, and Ketjenblack in acid (c) and base (d) for comparison.

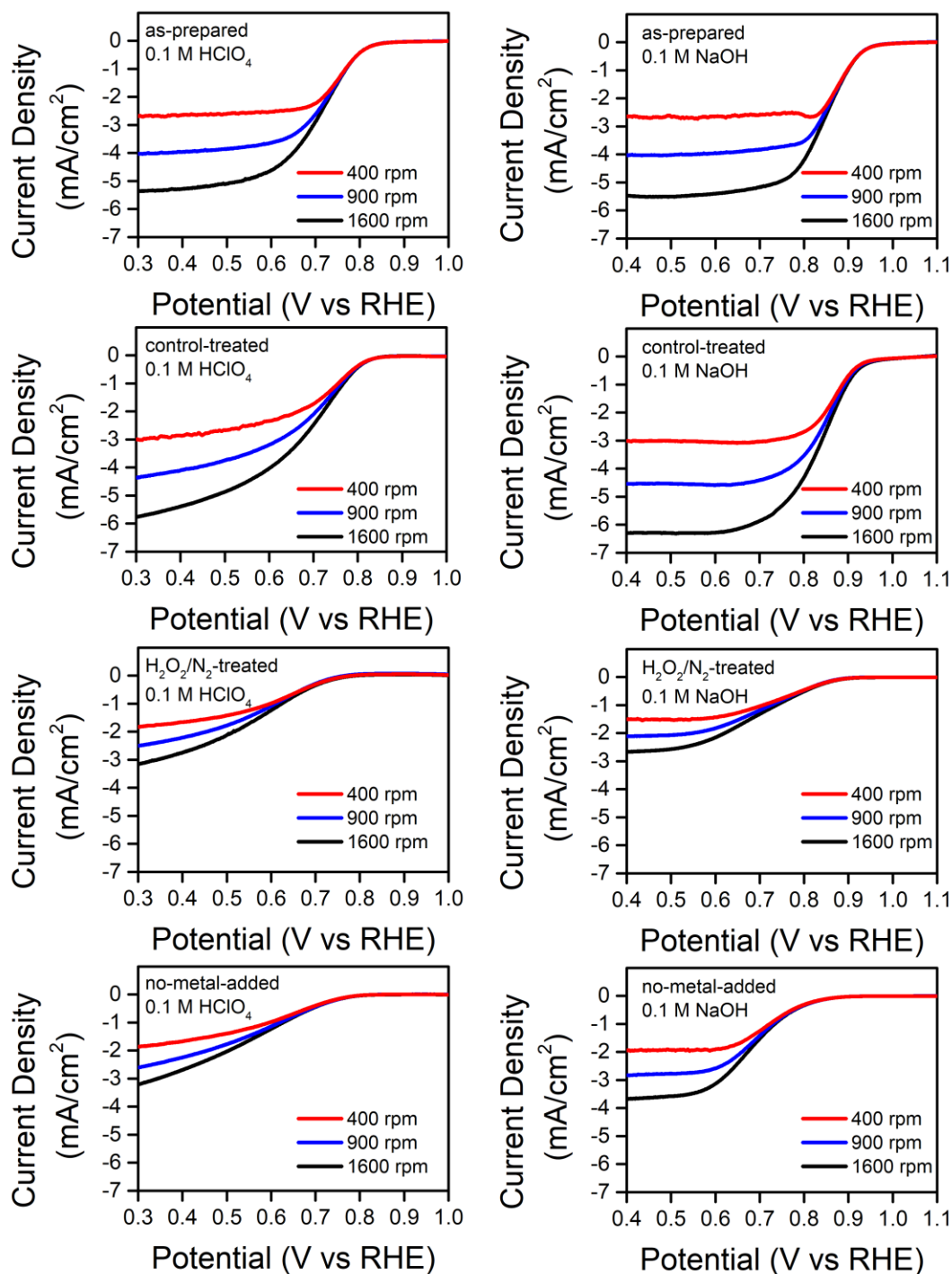


Figure 3.6 LSVs obtained using a RDE in acid and base for Koutecky-Levich analysis.

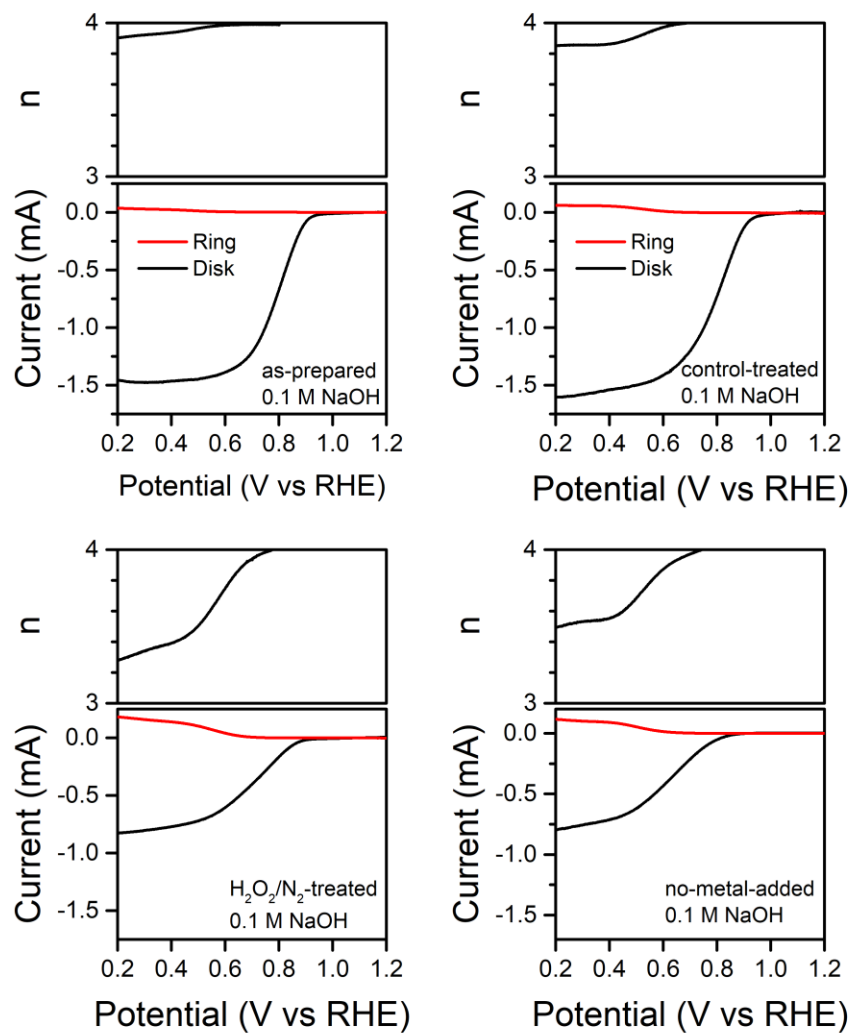


Figure 3.7 Rotating ring-disk electrode (RRDE) results giving the calculated electron transfer numbers ( $n$ ) in base.



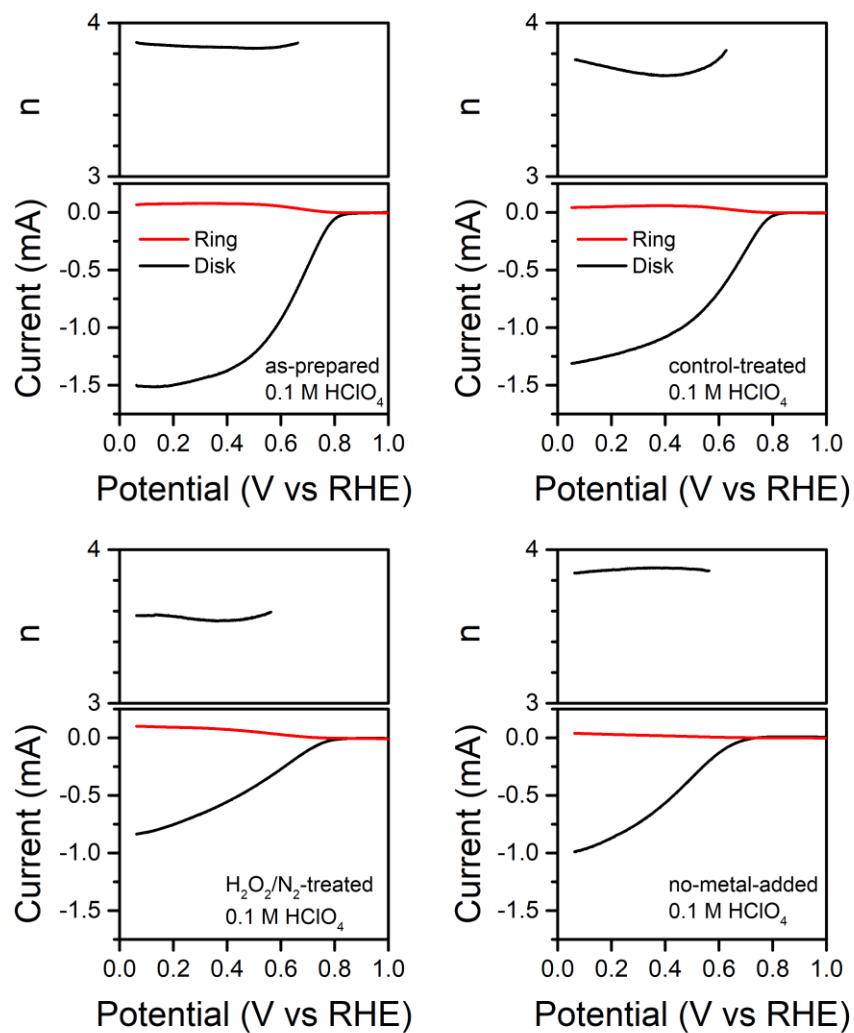


Figure 3.8 Rotating ring-disk electrode (RRDE) results giving the calculated electron transfer numbers (n) in acid.

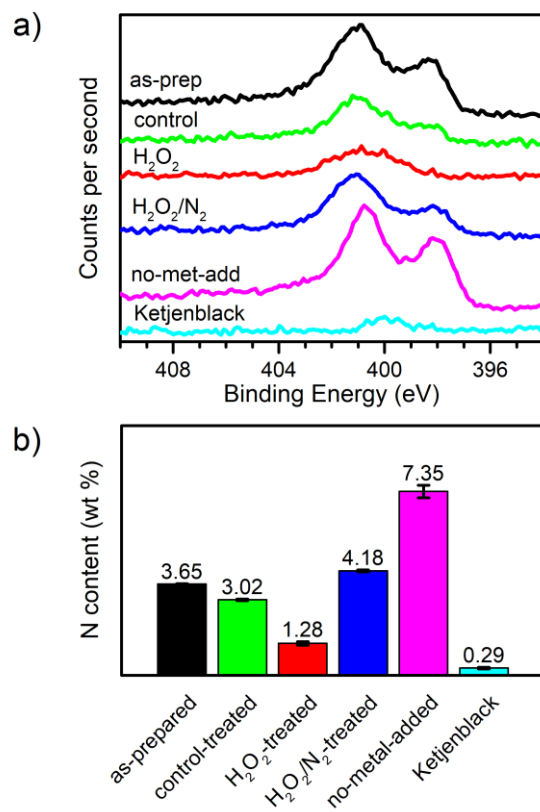


Figure 3.9 N1s XPS spectra for all catalysts (a) and total N content determined using CHN analysis (b).

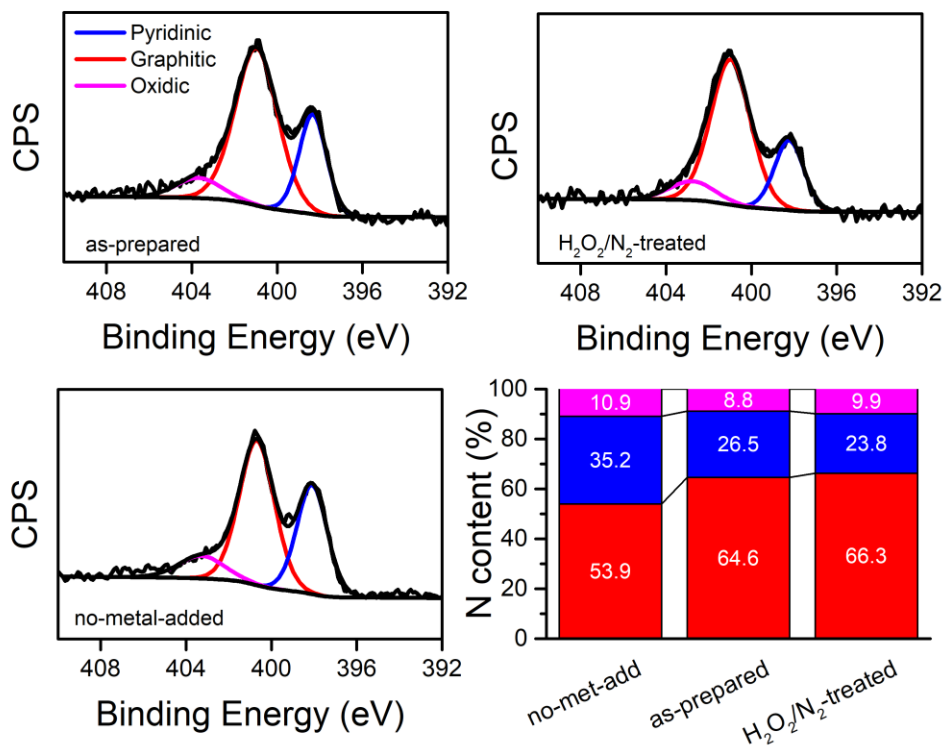


Figure 3.10 XPS N1s spectra and fitting for the as-prepared, H<sub>2</sub>O<sub>2</sub>/N<sub>2</sub>-treated, and no-metal-added catalysts along with a comparison of the content of each N species in each catalyst.

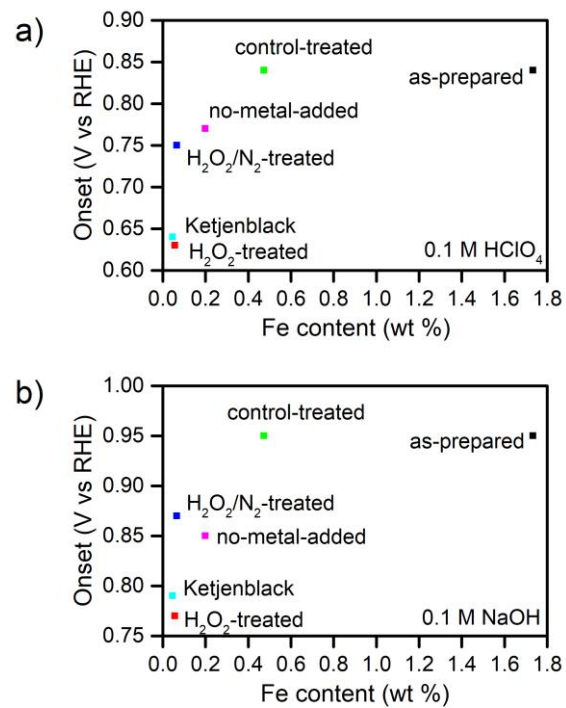


Figure 3.11 Relationship between Fe content and ORR onset in acid (a) and base (b).

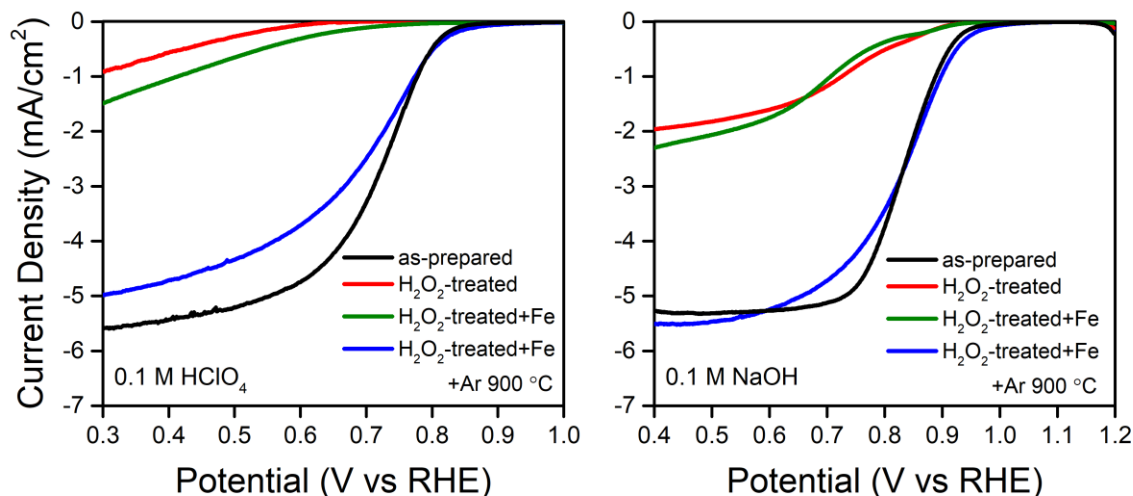


Figure 3.12 LSVs of catalysts before and after re-introduction of Fe in acid (left) and base (right). The  $n$  values for the  $\text{H}_2\text{O}_2$ -treated+Fe+Ar 900 °C catalyst are 3.41 and 3.43 in acid (at 0.3 V vs RHE) and base (at 0.4 V vs RHE) respectively, determined using Koutecky-Levich analysis.

Table 3.1 Summary of catalysts prepared in this work.

Catalyst	Abbreviation	Preparation
As-prepared	As-prep	Catalyst prepared w/ addition of Fe
No-metal-added	No-met-add	Catalyst prepared w/o addition of Fe
Control-treated	Control	As-prepared catalyst treated in $\text{H}_2\text{SO}_4$ and $\text{H}_2\text{O}$
$\text{H}_2\text{O}_2$ -treated	$\text{H}_2\text{O}_2$	As-prepared catalyst treated in $\text{H}_2\text{SO}_4$ and $\text{H}_2\text{O}_2$
$\text{H}_2\text{O}_2/\text{N}_2$ -treated	$\text{H}_2\text{O}_2/\text{N}_2$	$\text{H}_2\text{O}_2$ -treated catalyst pyrolyzed under $\text{N}_2$ at 900 °C
Ketjenblack	KJB	Ketjenblack EC600J used as received

Table 3.2 Fitting parameters and assignment of Fe signal measured using Mössbauer spectroscopy. Assignment of Fe species made by comparing to previous literature.<sup>18,39,40</sup>













Component	Color	$\delta_{\text{iso}}/$ $\text{mm s}^{-1}$	$\Delta E_{\text{Q}}/$ $\text{mm s}^{-1}$	$\Delta H_{\text{int}}/$ T	fwhm/ $\text{mm s}^{-1}$	Assignment
As-prepared						
Doublet 1		0.24	1.08	-	0.53	FeN <sub>4</sub>
Doublet 2		1.00	3.20	-	0.81	FeN <sub>4</sub>
Doublet 3		0.37	2.32	-	0.81	FeN <sub>4</sub>
Sextet 1		0.18	-	21.3	0.39	Fe <sub>3</sub> C
Control-treated						
Doublet 1		0.45	1.10	-	1.70	FeN <sub>4</sub>
Doublet 2		0.72	3.25	-	0.87	FeN <sub>4</sub>
Doublet 3		0.73	2.06	-	0.87	FeN <sub>4</sub>
Sextet 1		0.53	-	20.8	0.38	Fe <sub>3</sub> C
No-metal-added						
Doublet 1		0.45	1.10	-	1.30	FeN <sub>4</sub>
Doublet 2		0.92	2.85	-	1.21	FeN <sub>4</sub>
Doublet 3		0.63	2.26	-	1.30	FeN <sub>4</sub>
Singlet 1		0.00	-	-	0.35	$\alpha$ -Fe (superparamagnetic)

Table 3.3 Electron transfer numbers (n) determined using Koutecky-Levich analysis.

Catalyst	n in acid (0.3 V vs RHE)	n in base (0.4 V vs RHE)
as-prepared	3.7 ± 0.2	3.4 ± 0.5
control-treated	3.8 ± 0.4	3.4 ± 0.5
H <sub>2</sub> O <sub>2</sub> /N <sub>2</sub> -treated	2.8 ± 0.4	2.2 ± 0.4
no-metal-added	3.0 ± 0.4	2.7 ± 0.2

### 3.6 References

- (1) Shao, M.; Chang, Q.; Dodelet, J.-P.; Chenitz, R. *Chem. Rev.* **2016**, *116*, 3594.
- (2) Wu, J.; Yang, H. *Acc. Chem. Res.* **2013**, *46*, 1848.
- (3) Gewirth, A. A.; Thorum, M. S. *Inorg. Chem.* **2010**, *49*, 3557.
- (4) Wu, G.; Zelenay, P. *Acc. Chem. Res.* **2013**, *46*, 1878.
- (5) van Veen, J. A. R.; van Baar, J. F.; Kroese, K. J. *J. Chem. Soc., Faraday Trans. 1 F* **1981**, *77*, 2827.
- (6) Faubert, G.; Lalande, G.; Côté, R.; Guay, D.; Dodelet, J. P.; Weng, L. T.; Bertrand, P.; Dénès, G. *Electrochim. Acta* **1996**, *41*, 1689.
- (7) Lalande, G.; Faubert, G.; Côté, R.; Guay, D.; Dodelet, J. P.; Weng, L. T.; Bertrand, P. *J. Power Sources* **1996**, *61*, 227.
- (8) Franke, R.; Ohms, D.; Wiesener, K. *J. Electroanal. Chem. Interfacial Electrochem.* **1989**, *260*, 63.
- (9) Wiesener, K. *Electrochim. Acta* **1986**, *31*, 1073.
- (10) Faubert, G.; Côté, R.; Guay, D.; Dodelet, J. P.; Dénès, G.; Poleunis, C.; Bertrand, P. *Electrochim. Acta* **1998**, *43*, 1969.
- (11) Singh, D.; Tian, J.; Mamtani, K.; King, J.; Miller, J. T.; Ozkan, U. S. *J. Catal.* **2014**, *317*, 30.
- (12) Jaouen, F.; Proietti, E.; Lefevre, M.; Chenitz, R.; Dodelet, J.-P.; Wu, G.; Chung, H. T.; Johnston, C. M.; Zelenay, P. *Energy Environ. Sci.* **2011**, *4*, 114.
- (13) Mamtani, K.; Singh, D.; Tian, J.; Millet, J. M. M.; Miller, J. T.; Co, A. C.; Ozkan, U. S. *Catal. Lett.* **2016**, *146*, 1749.

- (14) Wang, J.; Nakazato, T.; Sakanishi, K.; Yamada, O.; Tao, H.; Saito, I. *Anal. Chim. Acta* **2004**, *514*, 115.
- (15) Ge, C.; Lao, F.; Li, W.; Li, Y.; Chen, C.; Qiu, Y.; Mao, X.; Li, B.; Chai, Z.; Zhao, Y. *Anal. Chem.* **2008**, *80*, 9426.
- (16) Wu, G.; More, K. L.; Johnston, C. M.; Zelenay, P. *Science* **2011**, *332*, 443.
- (17) Wang, H.; Côté, R.; Faubert, G.; Guay, D.; Dodelet, J. P. *J. Phys. Chem. B* **1999**, *103*, 2042.
- (18) Ferrandon, M.; Kropf, A. J.; Myers, D. J.; Artyushkova, K.; Kramm, U.; Bogdanoff, P.; Wu, G.; Johnston, C. M.; Zelenay, P. *J. Phys. Chem. C* **2012**, *116*, 16001.
- (19) Strickland, K.; Elise, M. W.; Jia, Q. Y.; Tylus, U.; Ramaswamy, N.; Liang, W. T.; Sougrati, M. T.; Jaouen, F.; Mukerjee, S. *Nat. Commun.* **2015**, *6*, 8343.
- (20) Goellner, V.; Armel, V.; Zitolo, A.; Fonda, E.; Jaouen, F. *J. Electrochem. Soc.* **2015**, *162*, H403.
- (21) Zhang, G. X.; Chenitz, R.; Lefevre, M.; Sun, S.; Dodelet, J. P. *Nano Energy* **2016**, *29*, 111.
- (22) Wu, G.; Artyushkova, K.; Ferrandon, M.; Kropf, A. J.; Myers, D.; Zelenay, P. *ECS Trans.* **2009**, *25*, 1299.
- (23) Lefèvre, M.; Dodelet, J.-P. *Electrochim. Acta* **2003**, *48*, 2749.
- (24) Cheng, F.; Chen, J. *Chem. Soc. Rev.* **2012**, *41*, 2172.
- (25) Muthukrishnan, A.; Nabaee, Y. *J. Phys. Chem. C* **2016**, *120*, 22515.
- (26) Matter, P. H.; Zhang, L.; Ozkan, U. S. *J. Catal.* **2006**, *239*, 83.



- (27) Lalande, G.; Côté, R.; Guay, D.; Dodelet, J. P.; Weng, L. T.; Bertrand, P.  
*Electrochim. Acta* **1997**, *42*, 1379.
- (28) Bezerra, C. W. B.; Zhang, L.; Lee, K.; Liu, H.; Marques, A. L. B.; Marques, E. P.;  
Wang, H.; Zhang, J. *Electrochim. Acta* **2008**, *53*, 4937.
- (29) Wu, G. *Frontiers in Energy* **2017**, *11*, 286.
- (30) Jaouen, F.; Dodelet, J.-P. *Electrochim. Acta* **2007**, *52*, 5975.
- (31) Varnell, J. A.; Tse, E. C. M.; Schulz, C. E.; Fister, T. T.; Haasch, R. T.;  
Timoshenko, J.; Frenkel, A. I.; Gewirth, A. A. *Nat. Commun.* **2016**, *7*, 12582.
- (32) Dai, L.; Xue, Y.; Qu, L.; Choi, H.-J.; Baek, J.-B. *Chem. Rev.* **2015**, *115*, 4823.
- (33) Liu, X.; Dai, L. **2016**, *1*, 16064.
- (34) Guo, D.; Shibuya, R.; Akiba, C.; Saji, S.; Kondo, T.; Nakamura, J. *Science* **2016**,  
*351*, 361.
- (35) Kolodiazhnyi, T.; Pumera, M. *Small* **2008**, *4*, 1476.
- (36) Wang, L.; Ambrosi, A.; Pumera, M. *Angew. Chem. Int. Ed.* **2013**, *52*, 13818.
- (37) Wang, L.; Wong, C. H. A.; Kherzi, B.; Webster, R. D.; Pumera, M.  
*ChemCatChem* **2015**, *7*, 1650.
- (38) Pumera, M.; Miyahara, Y. *Nanoscale* **2009**, *1*, 260.
- (39) Zitolo, A.; Goellner, V.; Armel, V.; Sougrati, M. T.; Mineva, T.; Stievano, L.;  
Fonda, E.; Jaouen, F. *Nat. Mater.* **2015**, *14*, 937.
- (40) Kramm, U. I.; Herranz, J.; Larouche, N.; Arruda, T. M.; Lefevre, M.; Jaouen, F.;  
Bogdanoff, P.; Fiechter, S.; Abs-Wurmbach, I.; Mukerjee, S.; Dodelet, J.-P.  
*PCCP* **2012**, *14*, 11673.

## Chapter 4

### Elucidating Proton Involvement in the Rate-Determining Step for Pt/Pd-Based and Non-Precious Metal Oxygen Reduction Reaction Catalysts Using the Kinetic Isotope Effect

Reprinted with permission from Tse, E.C.M., Varnell, J.A., Hoang, T.T.H, Gewirth, A.A *J. Phys. Chem. Lett.* 2016, 7 (18), 3542-3547. Copyright 2016 American Chemical Society.

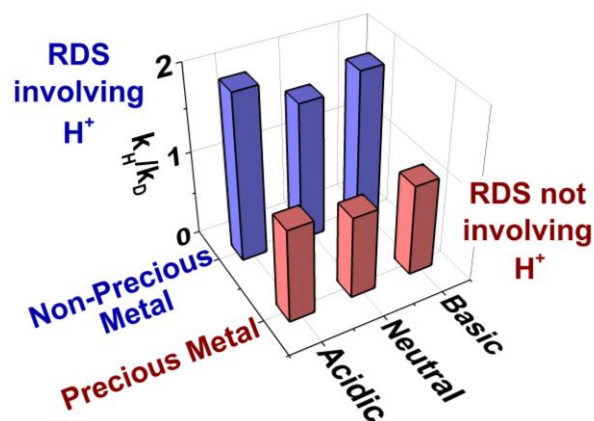


Figure 4.1 Graphical summary of the experimental results described in this work.

#### 4.1 Introduction

The oxygen reduction reaction (ORR) is central to the development of alternative energy conversion devices.<sup>1,2</sup> Currently, state-of-the-art fuel cells utilize Pt or one of its alloys to facilitate the ORR.<sup>3-6</sup> Unfortunately, these precious materials degrade or are poisoned during operation and despite being the best catalysts they still exhibit overpotentials of about 300 mV. An alternate strategy to promote efficient O<sub>2</sub> reduction is to utilize low-cost and poison-resistant non-precious metal (NPM) catalysts.<sup>2,7,8</sup> State-of-the-art NPM ORR catalysts are prepared via pyrolysis of transition metal/N/C precursors,<sup>9</sup> which results in a highly heterogeneous surface

structure.<sup>10</sup> Due to the heterogeneity of the catalyst material,<sup>11</sup> optimization of ORR performance cannot be achieved using conventional structure-activity relationship approaches.<sup>12</sup> Apart from the incomplete structural information of the active site, the pathways which lead to formation of deleterious side products such as  $O_2^-$  and  $H_2O_2$  implicated in fuel cell degradation are also elusive.<sup>13,14</sup> Despite advances in the preparation and characterization of competent NPM catalysts, a complete understanding of the ORR mechanism is still lacking.<sup>2,9,15-17</sup>

Understanding the ORR mechanism is instrumental to lowering the activation barrier of ORR. For precious metals and their alloys, the principle of Sabatier is invoked in so-called ‘volcano plots’ or ‘d-band model’ which relate rate to a thermodynamic quantity,<sup>18</sup> typically the M-O bond strength or related quantity.<sup>19</sup> Nonetheless, using computational approaches to delineate the explicit role of protons from that of electrons in ORR is particularly challenging, and the reaction kinetics of heterogeneous catalytic processes remains poorly understood.<sup>20</sup> The best results are found for Pt-X (X = Ni, Co) alloys which destabilize the M-OH bond to a certain extent.<sup>21</sup> Tafel slopes are also used to discuss ORR mechanism.<sup>22-24</sup> For Pt, which exhibits the lowest overpotential for the ORR to date, a 120 mV/dec Tafel slope was observed, suggesting that the rate-determining step (RDS) for Pt is the first electron transfer step which involves the transfer of a single electron and no protons.<sup>4</sup> The onset potential of ORR by Pt is not pH-dependent,<sup>25</sup> further providing evidence that the RDS is not a proton-coupled electron transfer (PCET) step. On the other hand, recent studies of NPM catalysts have shown that the ORR onset potential is pH-dependent,<sup>8,12,15</sup> suggesting that protons are involved in the RDS. An important question is whether the ORR mechanism on Pt and related metals is the same as that in the NPM materials.

Another way to study mechanism is through the kinetic isotope effect (KIE), particularly in organic and inorganic reactions.<sup>26-32</sup> Specifically, the substitution of hydrogen with deuterium many times yields large differences in reaction rates arising from reduced mass differences between the isotopes.<sup>33,34</sup> The use of KIE to study the ORR was pioneered by Yeager and coworkers. Their efforts show that Pt does not exhibit a KIE during ORR in phosphoric acid, signifying that the steps at or before the RDS do not involve protons.<sup>32</sup> A recent report found that Au(100) exhibits a substantial KIE during ORR at pH < 7, but no KIE at pH > 7.<sup>35</sup> Information about the pH dependence of the KIE on Pt as well as other metals is lacking. Additionally, the magnitude of the KIE and its pH dependence on NPM catalysts is unknown.

In this paper, we examine the effect of deuteration on the ORR process for three different ORR catalysts in three different pH regimes: the acidic condition that is relevant to proton-conducting polymer electrolyte membrane fuel cells, neutral conditions found commonly in biological systems, and basic conditions for alkaline fuel cells. Finally, we evaluate the effect of deuteration on product speciation for Pt, Pd, and NPM electrodes.

## 4.2 Results

For our KIE studies, we selected PANI-Fe-C as a representative NPM catalyst with high activity, along with Pt/C, and Pd/C, which are common fuel cell catalysts. In order to calculate the KIE of these catalysts during ORR, we used Koutecky-Levich analysis. The voltammograms of O<sub>2</sub> reduction catalyzed by PANI-Fe-C, Pt/C, and Pd/C under various rotation regimes in acidic, neutral, and basic conditions and the corresponding Koutecky-Levich plots are shown in **Figures 4.2 and 4.3-5**. We note that in some cases the O<sub>2</sub>-diffusion limited current densities observed in proteo solution are different from those found in deutero solution. However, the difference in the mass transport limited current density does not directly relate to the KIE.

Additionally, for some cases the LSVs do not reach a constant diffusion limited current,<sup>36</sup> which can be explained by the heterogeneity present in NPM catalysts commonly reported in literature.<sup>9,11,12</sup> For the Pt case, a change in the slope of the ORR voltammograms is observed due to the change in Tafel slopes, i.e. changing from a 1e<sup>-</sup> to a 2e<sup>-</sup> rate-limiting step, which is related to the different potential-dependent and pH-dependent stability of the surface structure of the oxide layer. This phenomenon is well-characterized in the literature.<sup>4,23,25,37-41</sup>

The KIE was determined from the voltammograms by comparing the kinetically limited current density ( $j_K$ ) given by the Koutecky-Levich equation:

$$\frac{1}{j} = \frac{1}{j_K} + \frac{1}{j_{l,c}}$$

$$j_K = nFk_f C_{O_2}^*$$

where  $j_{l,c}$  = limiting cathodic current density,  $n$  = number of electrons transferred,  $F$  = Faraday's constant,  $k_f$  = heterogeneous rate constant for reduction, and  $C_{O_2}^*$  = the bulk concentration of  $O_2$ . In order to observe the kinetic effect of the replacement of hydrogen with deuterium, inks were prepared using Nafion powder to eliminate the effect of trapped protons in the catalyst film.

**Figure 4.6** shows bar graphs that summarizes the kinetically limited current densities of PANI-Fe-C, Pt/C, and Pd/C in  $O_2$ -saturated acidic, neutral and basic solutions. The observed kinetically limited current densities are comparable to the values found for conventional heterogeneous ORR catalysts.<sup>42-44</sup> We observe a dramatic decrease in the ORR kinetically limited current density for the deuterio case relative to the proteo case for PANI-Fe-C in all three pH regimes. The majority of the decrease in the kinetically limited current density observed for the NPM catalyst is therefore attributed to a KIE. By way of contrast, the ORR  $j_K$  for Pt/C and Pd/C exhibits only a slight dependence on whether the electrolyte is deuterated or not, which is attributed to the difference in bulk concentration of  $O_2$  in proteo and deuterio solvents. By taking

into account the differences in the value of  $C_{O_2}^*$  in proteo and deuterio solutions and comparing the results in the two solutions, the kinetic isotope effects for the ORR catalyzed by PANI-Fe-C, Pt/C and Pd/C can be calculated.

**Table 4.1** shows the KIE corrected for the differences in  $C_{O_2}^*$  in proteo and deuterio solutions observed for PANI-Fe-C, Pt/C and Pd/C catalysts. For Pt/C a KIE of 1 was observed in all three pH regimes. The lack of a KIE on Pt signifies that protons are not involved in the RDS during ORR on Pt, in agreement with previous results by Yeager.<sup>32</sup> Additionally, the absence of a KIE on Pt is consistent with the use of Tafel slope to examine the ORR mechanism, which suggests that the RDS is a  $1e^-$  or  $2e^-$  step without proton involvement.<sup>4</sup> For PANI-Fe-C, a KIE of approximately 2 was observed, which demonstrates the involvement of protons in the ORR mechanism at or before the RDS. The presence of a KIE for the NPM catalyst and lack of a KIE on Pt/C suggests that the mechanism for ORR includes a different RDS for these two catalysts. Pt/C exhibits a fairly low overpotential for the ORR, while that for PANI-Fe-C is somewhat higher. We wanted to test whether a higher overpotential for the ORR might be correlated with sensitivity to deuteration. Experiments using Pd/C, a catalyst that exhibits a higher overpotential for ORR than Pt/C, also show a KIE of 1, indicating that for these precious metal ORR catalysts (Pt/C and Pd/C) the RDS is a proton-independent electron transfer process. Together, these results suggest the existence of at least two broad classes of ORR catalysts, namely Pt-/Pd-based and NPM, each of which facilitates the ORR via a distinct mechanism with or without proton transfer at the RDS.

In an effort to investigate the effect of binder on protons or deuterons delivery to the catalytic site during the ORR process, we studied the ORR activity of PANI-Fe-C and Pt/C in proteo and deuterio solutions using an ink preparation method without Nafion powder.

Voltammograms for these inks are shown in **Figures 4.7-8**. **Figure 4.9** compares the kinetically limited current densities calculated from Koutecky-Levich plots of PANI-Fe-C and Pt/C using inks without Nafion powder. We observe lower ORR kinetically limited current densities by PANI-Fe-C in deuterio solutions as compared to proteo solutions. For Pt/C, the ORR kinetically limited current densities are similar in both deuterio and proteo solutions. **Table 4.2** displays the kinetic isotope effects calculated using values in **Figure 4.9**. In all three pH regimes, the kinetic isotope effects measured for PANI-Fe-C and Pt/C are ca. 2 and 1, respectively. These results are similar to those obtained from inks prepared using Nafion powder as binders.

To further investigate the effect of trapped protons in binders, we formulated inks using Nafion 117 solution saturated with protons. **Figures 4.10 and 4.11** display the ORR LSVs and Koutecky-Levich plots of PANI-Fe-C and Pt/C with inks saturated with protons. Using inks saturated with protons, we observed no change in the O<sub>2</sub> reduction voltammetries and the kinetically limited current densities. **Figure 4.12** shows the bar graphs summarizing the measured kinetically limited current densities of PANI-Fe-C and Pt/C with inks saturated with protons. **Table 4.3** summarizes the measured kinetically limited current densities and the calculated kinetic isotope effects of PANI-Fe-C and Pt/C with inks saturated with protons. Both PANI-Fe-C and Pt/C exhibit KIEs of ca. 1, suggesting that the presence of deuterons in bulk solution does not slow down nor speed up the ORR. These results suggest that by using inks prepared the conventional way with commercially available Nafion 117 solution and EtOH, protons remain trapped in the catalyst film even after drying.

In order to further investigate the role of protons in the ORR mechanism on Pt and NPM catalysts we carried out rotating ring disk electrode (RRDE) experiments in H and D solutions. Recently, we showed that by controlling the rate of proton transfer through a membrane we

could alter the reaction pathway of a Cu-based ORR catalyst and that by changing the pH to less acidic conditions and by switching to deuterated electrolyte that we could control product speciation on an Fe-based catalyst.<sup>45</sup> Here, we carried out similar RRDE experiments to monitor the amount of peroxide generated in H and D solutions and determine the selectivity of the electrocatalysts. **Figure 4.13a** displays the RRDE LSVs of PANI-Fe-C in proteo and deutero acidic conditions, and **Figure 4.13b** shows the number of electrons transferred by the NPM catalyst calculated from the amount of peroxide detected by the ring at two representative potentials. Upon performing the RRDE experiments in deuterated solution, the amount of current passing through the ring decreases, indicating that PANI-Fe-C generates less peroxide and reduces O<sub>2</sub> by a mechanism closer to 4 e<sup>-</sup> in 0.5M D<sub>2</sub>SO<sub>4</sub> than for the case in 0.5 M H<sub>2</sub>SO<sub>4</sub>. In contrast, Pt/C generates the same amount of peroxide in 0.5 M H<sub>2</sub>SO<sub>4</sub> and 0.5 M D<sub>2</sub>SO<sub>4</sub> solutions (**Fig. 4.13c and 4.13d**), suggesting that proton transfer kinetics do not play a role in dictating product selectivity during the ORR for Pt/C.

### 4.3 Discussion

Our KIE studies demonstrate that different ORR catalysts achieve the same reaction via different mechanisms, which is an important distinction when considering the design of new catalyst materials. Most notably, the observation that proton transfer kinetics must be considered for NPM catalysts but not for the Pt and Pd catalysts tested. In order to highlight the differences in the ORR on the two types of ORR catalysts studied, we attempted to incorporate our findings into two mechanisms. **Figure 4.14** shows our proposed ORR mechanisms consistent with the ORR results on Pt and Pd (**Fig. 4.14a**) or NPM ORR catalysts (**Fig. 4.14b**). The lack of a KIE on Pt and Pd indicates that protons do not participate in the RDS of the ORR, confirming that the RDS of O<sub>2</sub> reduction by Pt and Pd is a proton-independent electron transfer step (**Fig. 4.14a**), at



least in the high overpotential region.<sup>25,32</sup> Additionally, the fact that deuteration does not change the relative amount of peroxide generated by Pt also shows that this speciation is not controlled by the rate of proton transfer. The presence of an electron-transfer-limited RDS is fully consistent with the 120 mV dec<sup>-1</sup> Tafel slope observed in the so-called Langmuir region of the ORR voltammetry.<sup>4</sup> We also note that on an oxide-covered Pt surface, a 60 mV dec<sup>-1</sup> Tafel slope was observed previously in the Temkin region, indicative of a 2 e<sup>-</sup> RDS which also does not involve protons.<sup>4</sup> An electron transfer RDS signifies that proton transfer plays a negligible role in determining the ORR kinetics on Pt. Therefore, methods altering proton transfer kinetics for Pt and related materials will not change the ORR rate.<sup>21,46,47</sup>

For the NPM ORR catalyst examined, the presence of a KIE  $\approx 2$  indicates that protons are involved at or before the RDS. Furthermore, the decrease in peroxide yield observed in deuterated solution suggests that proton kinetics control the production of peroxide as a side product at a branch point in the mechanism. **Figure 4.14b** displays a possible mechanism that is consistent with these observations and is similar to some previously proposed ORR schemes.<sup>11,48,49</sup> In the mechanism presented in **Figure 4.14b**, protons are associated with the initial reduction of O<sub>2</sub> during the RDS. Previous work has shown that the ORR onset potential of NPM catalysts is pH-dependent,<sup>8,12,15</sup> further supporting the involvement of at least one protonation step at or before the RDS in the ORR mechanism. In order to explain the branch point we assign the bound hydroperoxyl adduct as a bifurcation species. If the electron transfer rate is comparable to or faster than the proton transfer kinetics, O-O bond cleavage will occur and promote H<sub>2</sub>O generation. If the kinetics of proton transfer is faster than the electron transfer rate, the hydroperoxyl species will be protonated off as H<sub>2</sub>O<sub>2</sub>, which is a deleterious ORR side product. Our present results recorded on a RRDE are similar to previous findings obtained using

a hybrid bilayer membrane electrochemical platform which explain the ORR activity and product selectivity of other previously reported ORR electrocatalysts.<sup>45</sup> The amount of H<sub>2</sub>O<sub>2</sub> detected for Cu and Fe containing catalysts generally decreases as the pH of the solution increases,<sup>8,12,15</sup> a phenomenon that can now be explained by the proton availability at the catalyst active site.

In this report, we investigated the effect of deuteration on the ORR activities of both precious and NPM catalysts. For the ORR on the precious metal catalysts Pt and Pd, we found a KIE of 1, in agreement with previous studies. For the ORR on Fe-based NPM catalysts, we found a KIE of 2 which demonstrates the involvement of protons at or before the RDS. Using RRDE experiments we also observed a decrease in the peroxide yield in deuterio-solution compared to proteo-solution suggesting that the decreased availability of deuterons as compared to protons at the same concentration helps to control product speciation during the ORR. Our KIE studies reveal the important role of protons during the ORR on NPM catalysts and immediately suggest the crucial need to consider proton transfer kinetics in the design and synthesis of improved NPM ORR catalysts.

#### **4.4 Experimental Methods**

*General-* Chemicals were obtained from commercial sources and used without further purification unless otherwise specified. All proteo and deuterio aqueous solutions were prepared freshly each day using Milli-Q water (> 18 MΩ cm) and D<sub>2</sub>O, respectively. For experiments at pH 0.3 and pD 0.3, H<sub>2</sub>SO<sub>4</sub> (500 mM) and D<sub>2</sub>SO<sub>4</sub> (500 mM) solutions were used, respectively. For experiments at pH 7 and pD 7, proteo potassium phosphate buffer solution (H-phos, 100 mM) and deuterio potassium phosphate buffer solution (D-phos, 100 mM) were used, respectively. For experiments at pH 13 and pD 13, NaOH (100 mM) and NaOD (100 mM)

solutions were used, respectively. Solutions were sparged with O<sub>2</sub>, which was dried using a drying tube, for 30 min prior to each experiment.

*Electrochemical Characterization-* Electrochemical studies were carried out using a CH Instruments 760 D Electrochemical Workstation (Austin, TX) at room temperature (24 °C to 26 °C). Experiments were performed in a three-compartment cell with an aqueous “no leak” Ag/AgCl (3 M KCl, eDAQ, Inc.) reference electrode separated from the working electrode by a Luggin capillary. A deviation of ca. 1.3 mV in the electrode potential of the Ag/AgCl reference was expected due to a temperature deviation of 2 °C.<sup>50</sup> A carbon rod counter electrode was separated from the working electrode by a glass frit. Unless otherwise stated, the scan rate was 10 mV s<sup>-1</sup>. The measured potential by the Ag/AgCl reference electrode did not shift in proteo and deuterio solutions, as confirmed by the peak position of the Fe(II/III) wave of K<sub>3</sub>Fe(CN)<sub>6</sub> (**Fig. 4.15**).<sup>31,45,51</sup> Electrochemical potentials are reported relative to the reversible hydrogen electrode (RHE) the value of which was measured by sparging the solution with H<sub>2</sub> (1 atm) and monitoring the open circuit potential between the Ag/AgCl reference and a Pt wire introduced following the measurement.<sup>12</sup> All experiments performed were at least quadruplicated. Voltammograms shown are from representative trials. Error bars presented represent standard deviations of all trials.

Rotating disk electrode (RDE) and rotating ring-disk electrode (RRDE) experiments were performed using a glassy carbon (GC) disk electrode (0.196 cm<sup>2</sup>, E5 series, Pine instruments) connected to a MSR<sub>X</sub> rotator (Pine Instruments). The GC working electrode was polished sequentially with 0.25 and 0.05 μm diameter diamond polish (Buehler), and sonicated in water after each stage. For RRDE experiments, a concentric Pt ring was used and electrochemically polished by cycling from -0.4 V to +1.7 V vs Ag/AgCl reference at 100 mV/s in an aqueous solution of HClO<sub>4</sub> (0.1 M) until the oxide stripping feature at about +0.35 V versus Ag/AgCl was

stable. PANI-Fe-C was prepared according to published procedure using a similar catalyst loading to the loading of NPM catalysts used in recent reports.<sup>9,52</sup> Ink slurries were prepared using Nafion 117 solution (5 wt % in alcohols, Sigma-Aldrich) or solution made of Nafion powder (Sigma-Aldrich). To prepare the binder solution from Nafion powder, Nafion powder (5 mg) was dissolved in IPA or IPA-D8 (95 mg). After sonicating the mixture for 10 min and heating to 70 °C for 1 min, PEG200 (5 mg) was added. PANI-Fe-C (7.2 mg), Pt supported on Vulcan XC-72 (Pt/C, 7.2 mg, 20 wt. %, E-Tek Inc.), or Pd supported on Vulcan XC-72 (Pd/C, 7.2 mg, 20 wt. %, E-Tek Inc.) was dispersed in EtOH (500 µL) or EtOD (500 µL) and sonicated for 20 min. Nafion solution (10 µL) was added, and the resultant ink solution was sonicated for 30 min. 10 µL ink (loading = 0.72 mg/cm<sup>2</sup>) was drop-casted onto a polished GC disk (0.196 cm<sup>2</sup>) and let dry under a stream of Ar. To eliminate the possibility of residual H<sup>+</sup> in the Nafion binder interfering with the experimental results obtained in D<sub>2</sub>O, the Nafion powder was reconstituted with EtOD, dried under reduced pressure, and this process was repeated three times. To further exchange the putative trapped protons in the prepared catalyst films, the electrode assembly was soaked in D<sub>2</sub>O for 5 min both with and without rotation. In all cases, the KIE values obtained were comparable to each other. For the binderless cases, the inks were prepared in analogous manner in the absence of Nafion solution. The resultant suspension was further sonicated for 20 min to afford an ink slurry, which was deposited onto a GC electrode and then dried under a stream of Ar.

*Calculating Kinetic Isotope Effect-* The kinetic isotope effect was calculated using the Koutecky-Levich equation and comparing the values of the kinetically limited current density ( $j_K$ ) determined experimentally in proteo and deutero conditions.

$$\frac{1}{j} = \frac{1}{j_K} + \frac{1}{j_{l,c}}$$

$$\text{limiting cathodic current density} = j_{l,c} = 0.62nFD_{O_2}^{2/3}\omega^{1/2}\nu^{-1/6}C_{O_2}^*$$

$$\text{kinetically limited current density} = j_K = nFk_fC_{O_2}^*$$

Where  $j$  = current density,  $n$  = number of electrons transferred,  $F$  = Faraday's constant,  $D_{O_2}$  = diffusion coefficient of  $O_2$ ,  $\omega$  = electrode rotation rate,  $\nu$  = kinematic viscosity,  $C_{O_2}^*$  = the bulk concentration of  $O_2$ , and  $k_f = k_0 e^{-\frac{\alpha F \eta}{RT}}$  = heterogeneous rate constant for reduction.

$j_{l,c}$  represents the current density obtained under totally mass-transfer-limited conditions and thus involves terms related to diffusion, bulk concentration, kinematic viscosity and rotation rate.  $j_K$  describes the current density measured under the kinetic limitation when the mass transfer is efficient enough to keep the concentration of reactants at the electrode surface equal to the bulk value. The current density absent any mass-transfer effects is a prerequisite to study kinetic isotope effect.

Plotting  $y = \frac{1}{j}$  and  $x = \frac{1}{\omega^{1/2}}$  gives:

$$\text{slope} = \frac{1}{0.62nFD_{O_2}^{2/3}\nu^{-1/6}C_{O_2}^*}$$

$$\text{intercept} = \frac{1}{j_K} = \frac{1}{nFk_fC_{O_2}^*}$$

Dividing  $j_K^H$  obtained in proteo solution by  $j_K^D$  obtained in deuterio solution gives:

$$\frac{j_0^H}{j_0^D} = \frac{n^H k_f^H C_{O_2}^{*,H}}{n^D k_f^D C_{O_2}^{*,D}}$$

Following established methods,<sup>53,54</sup> the solvomolalities of  $O_2$  in  $H_2O$  and  $D_2O$  at 298.15

K are converted to bulk concentrations of  $O_2$  in  $H_2O$  ( $C_{O_2}^{*,H}$ ) and in  $D_2O$  ( $C_{O_2}^{*,D}$ ) to yield

$$\frac{C_{O_2}^{*,H}}{C_{O_2}^{*,D}} = 0.908$$

Calculating the KIE at constant overpotentials and assuming the total number of electrons transferred and the transfer coefficients to be similar yields:

$$\frac{k_0^H}{k_0^D} = \frac{j_0^H C_{O_2}^{*,D}}{j_0^D C_{O_2}^{*,H}} = \frac{j_0^H}{j_0^D} \frac{1}{0.908}$$

KIE is calculated by comparing the rate constants in proteo ( $k_0^H$ ) and deuterio ( $k_0^D$ ) solutions, a procedure typically utilized in the literature.<sup>32-34</sup> The pre-exponential factor,  $A$ , in the Arrhenius equation remains almost unperturbed for all isotopically labeled compounds,<sup>55</sup> therefore we do not calculate KIE using the pre-exponential factor. Changes in  $O_2$  diffusion limited current is due to differences in  $O_2$  diffusion coefficients, kinematic viscosity, and bulk  $O_2$  concentration between H and D solutions. Similar changes in the peak current can be observed for the case without rotation.

The overpotentials used for Pt/C in acidic, neutral, and basic solutions 0.520 mV, 0.650 mV, and 0.540 mV respectively. The overpotentials used for Pd/C in acidic, neutral, and basic solutions 0.530 mV, 0.630 mV, and 0.470 mV respectively. The overpotentials used for PANI-Fe-C in acidic, neutral, and basic solutions 0.820 mV, 0.550 mV, and 0.540 mV respectively.

## 4.5 Figures and Tables

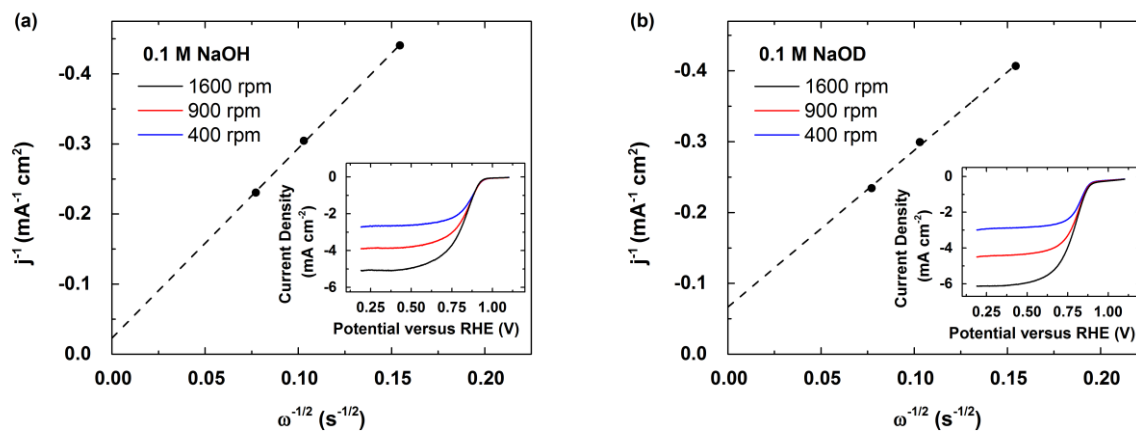


Figure 4.2 Koutecky-Levich plots and rotating disk electrode (RDE) voltammograms (insets) of PANI-Fe-C in (a) pH 13 and (b) pD 13 O<sub>2</sub>-saturated solutions with a scan rate of 10 mV s<sup>-1</sup> at 400 (blue), 900 (red), and 1600 (black) rpm.

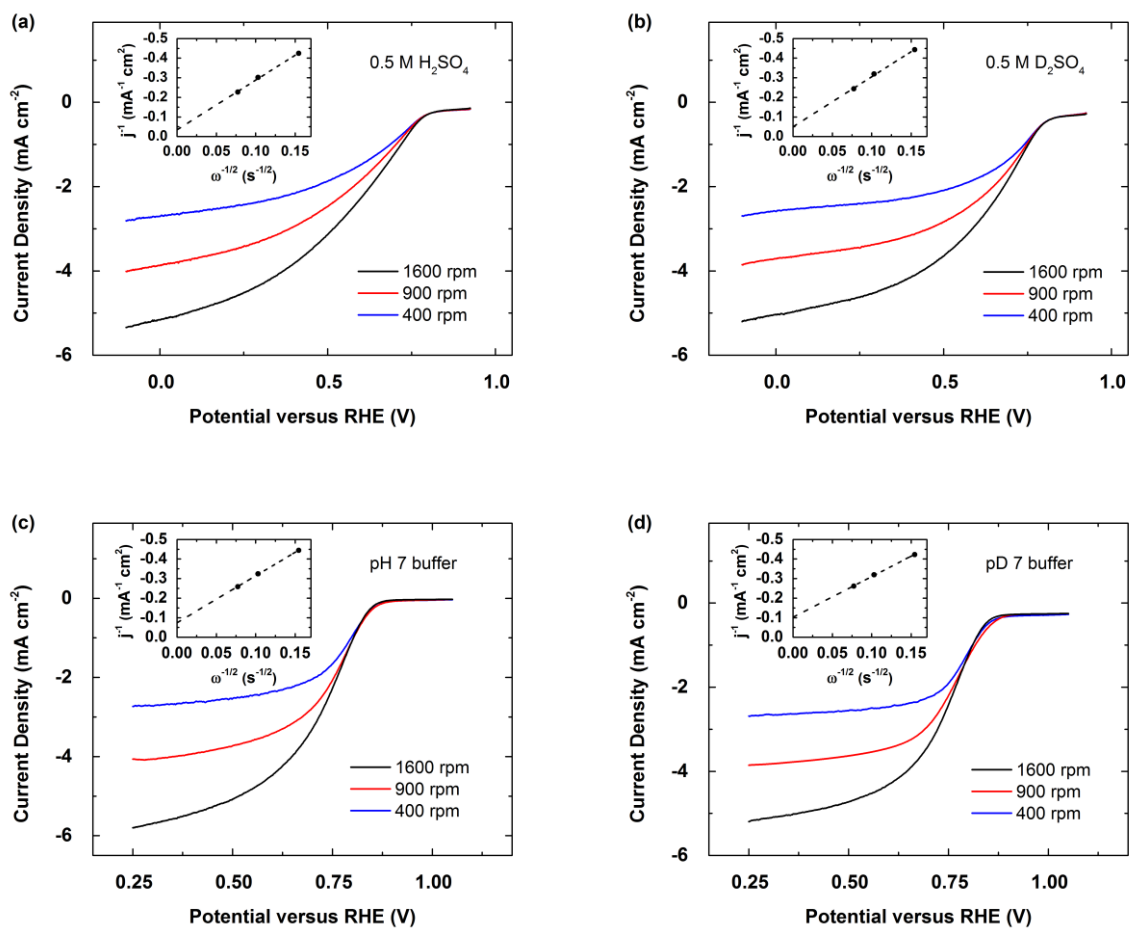


Figure 4.3 RDE voltammograms and Koutecky-Levich plots (insets) of PANI-Fe-C with inks prepared with Nafion powder in (a) pH 0.3, (b) pD 0.3, (c) pH 7, and (d) pD 7  $\text{O}_2$ -saturated solutions with a scan rate of 10 mV/s at 400 (blue), 900 (red), and 1600 (black) rpm.



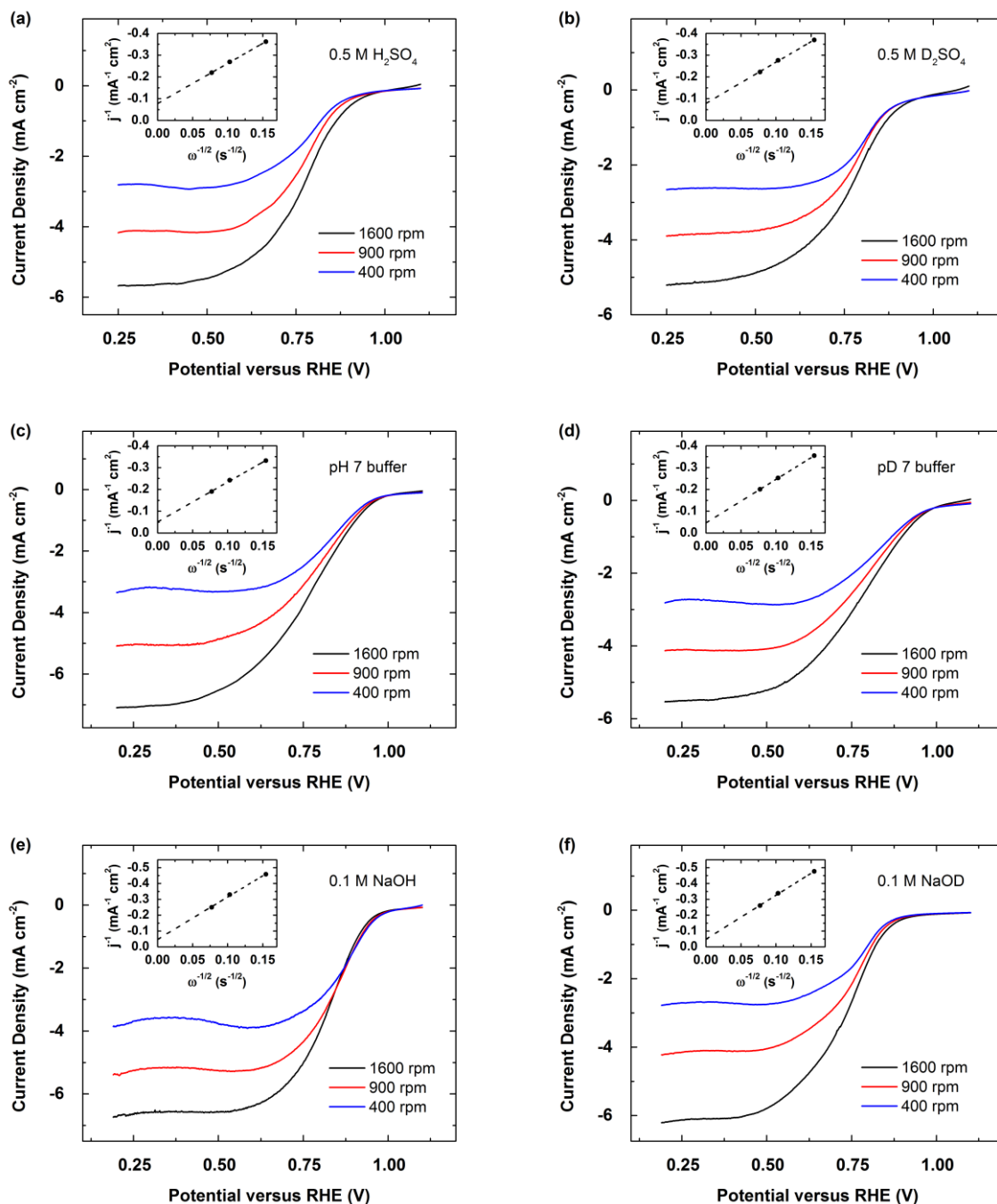


Figure 4.4 RDE voltammograms and Koutecky-Levich plots (insets) of 20 wt.% Pt supported on Vulcan XC-72 with inks prepared with Nafion powder in (a) pH 0.3, (b) pD 0.3, (c) pH 7, (d) pD 7, (e) pH 13, and (f) pD 13  $\text{O}_2$ -saturated solutions with a scan rate of 10 mV/s at 400 (blue), 900 (red), and 1600 (black) rpm.

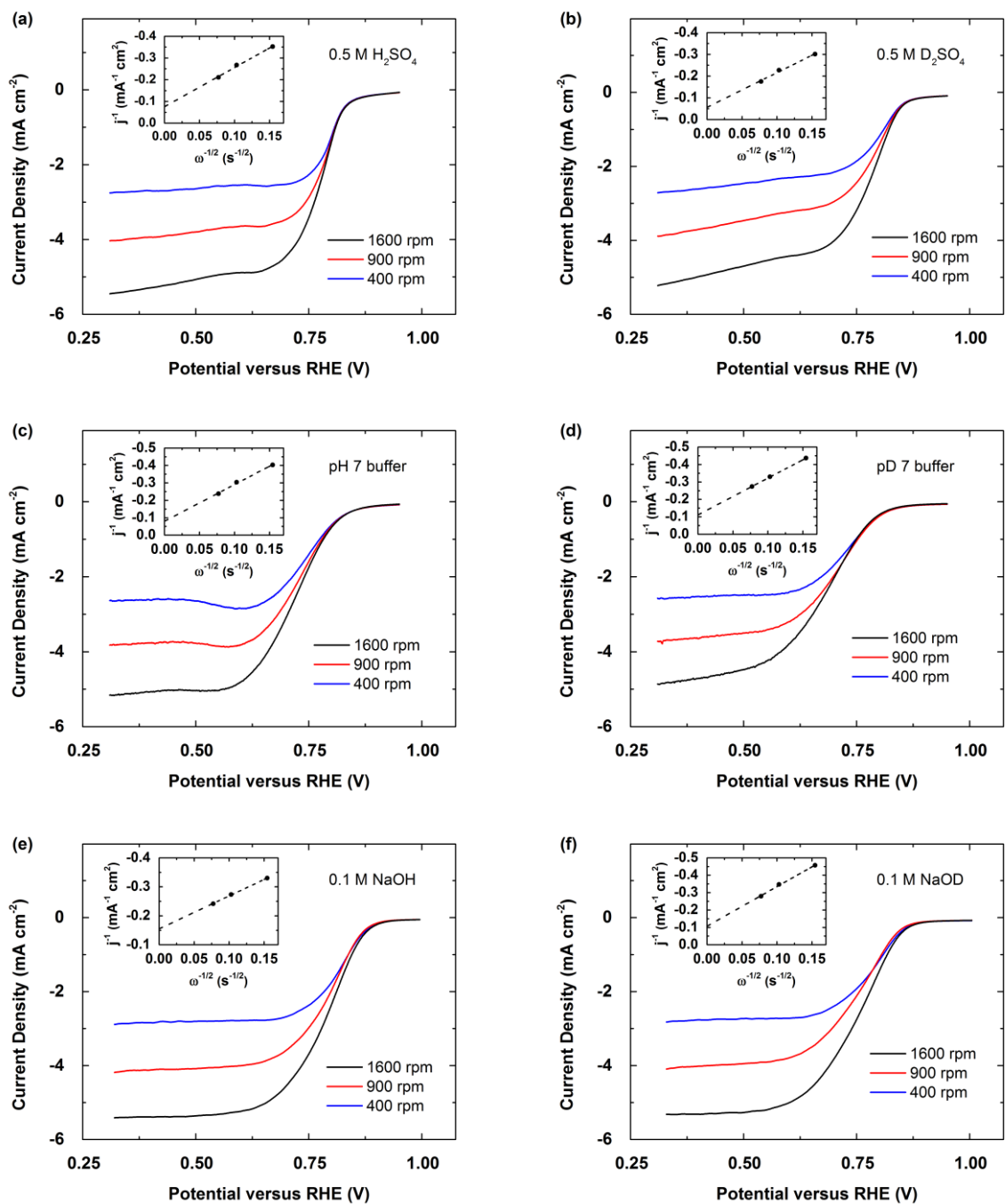


Figure 4.5 RDE voltammograms and Koutecky-Levich plots (insets) of 20 wt.% Pd supported on Vulcan XC-72 with inks prepared with Nafion powder in (a) pH 0.3, (b) pD 0.3, (c) pH 7, (d) pD 7, (e) pH 13, and (f) pD 13  $\text{O}_2$ -saturated solutions with a scan rate of 10 mV/s at 400 (blue), 900 (red), and 1600 (black) rpm.

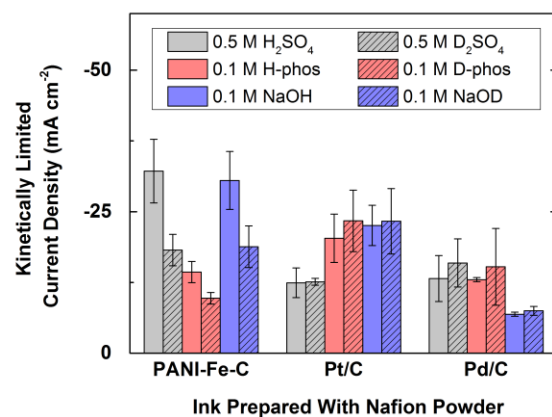


Figure 4.6 Bar graphs summarizing the kinetically limited current densities obtained from Koutecky-Levich analyses of O<sub>2</sub> reduction voltammograms for PANI-Fe-C, Pt/C and Pd/C with inks prepared with Nafion powder in O<sub>2</sub>-saturated 0.5 M H<sub>2</sub>SO<sub>4</sub> (gray), 0.5 M D<sub>2</sub>SO<sub>4</sub> (gray with stripes), 0.1 M pH 7 phosphate buffer (red), 0.1 M pD 7 phosphate buffer (red with stripes), 0.1 M NaOH (blue), and 0.1 M NaOD (blue with stripes) solutions.

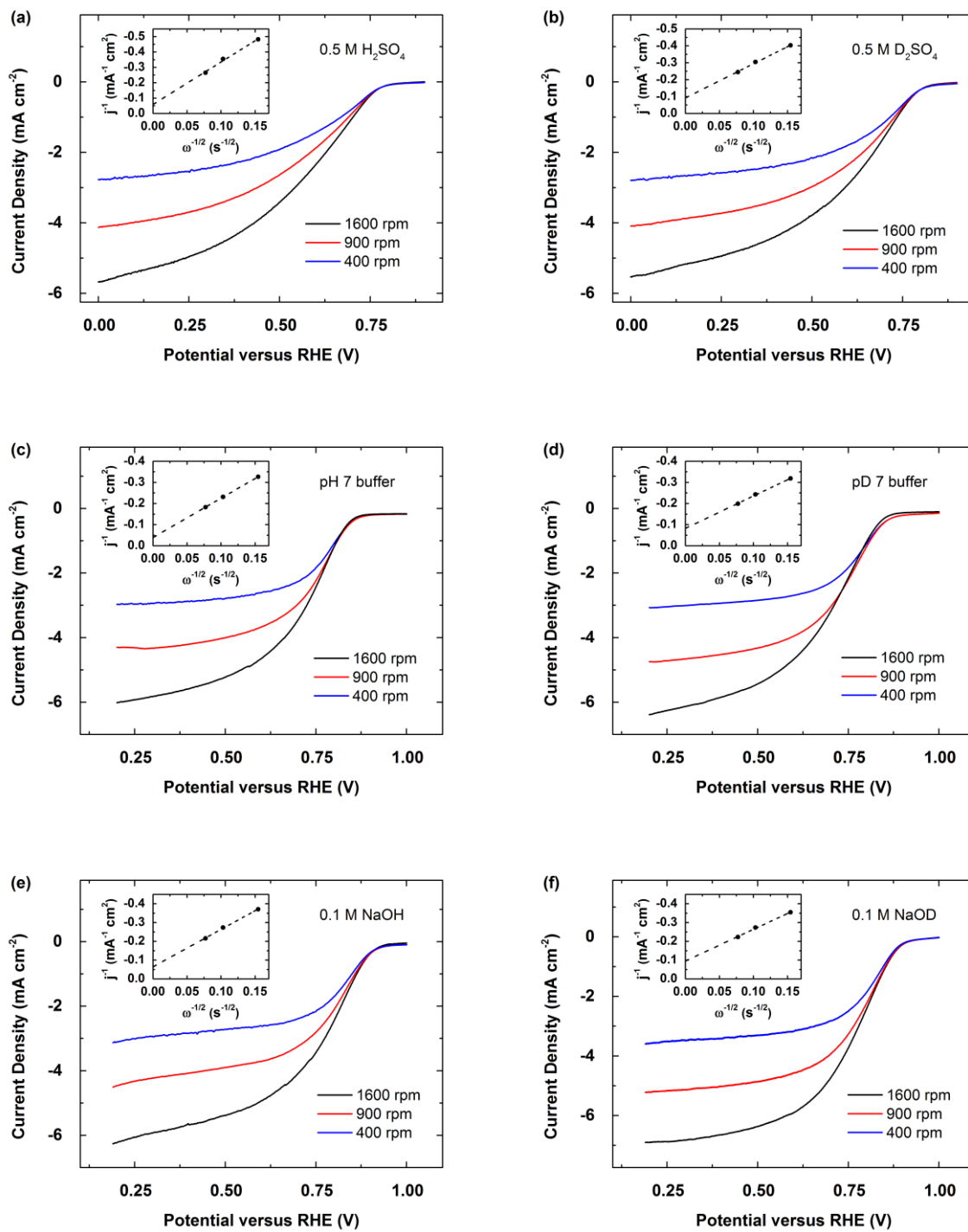


Figure 4.7 RDE voltammograms and Koutecky-Levich plots (insets) of PANI-Fe-C without binder in (a) pH 0.3, (b) pD 0.3, (c) pH 7, (d) pD 7, (e) pH 13, and (f) pD 13 O<sub>2</sub>-saturated solutions with a scan rate of 10 mV/s at 400 (blue), 900 (red), and 1600 (black) rpm.

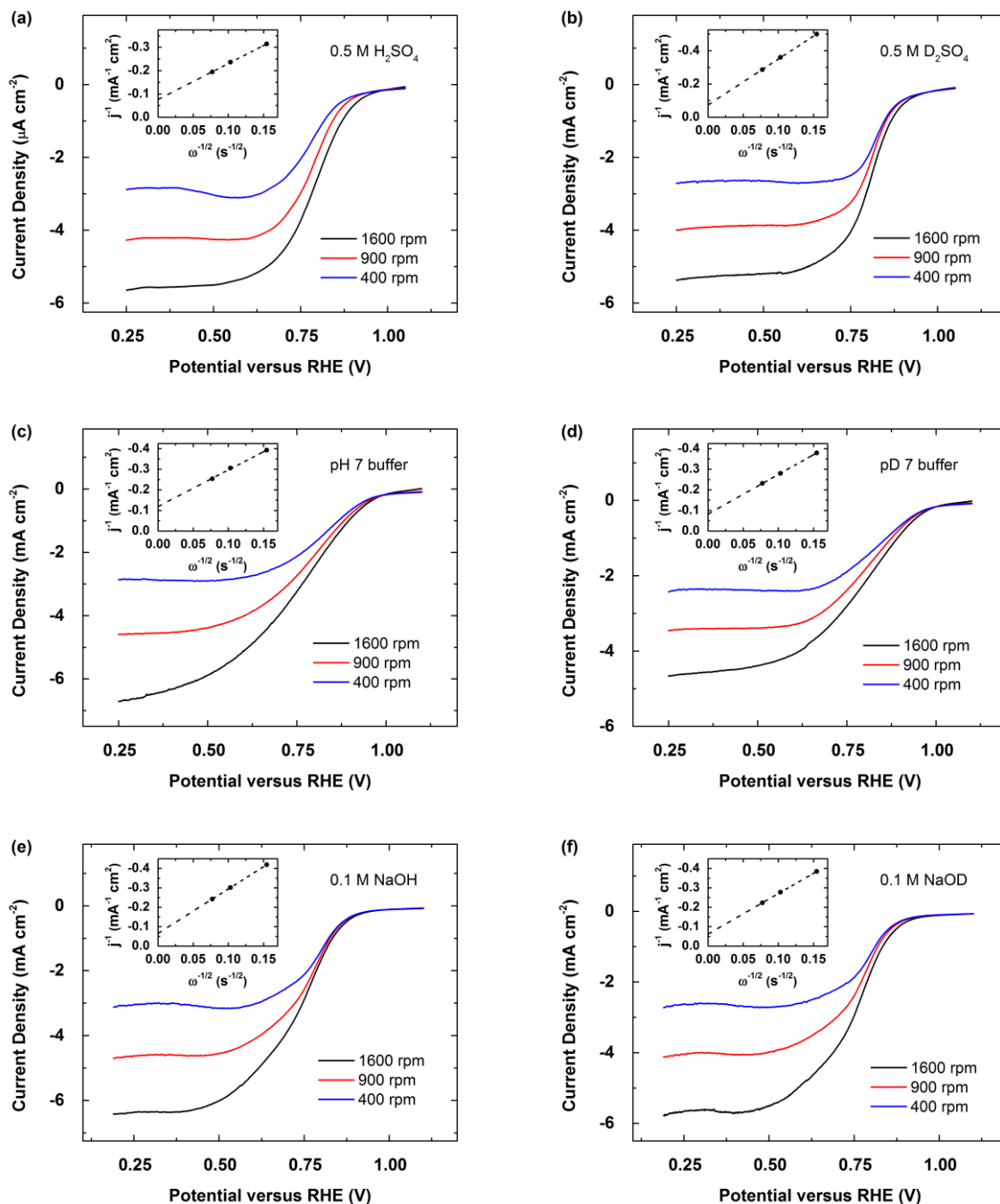


Figure 4.8 RDE voltammograms and Koutecky-Levich plots (insets) of 20 wt.% Pt supported on Vulcan XC-72 without binder in (a) pH 0.3, (b) pD 0.3, (c) pH 7, (d) pD 7, (e) pH 13, and (f) pD 13  $\text{O}_2$ -saturated solutions with a scan rate of 10 mV/s at 400 (blue), 900 (red), and 1600 (black) rpm.

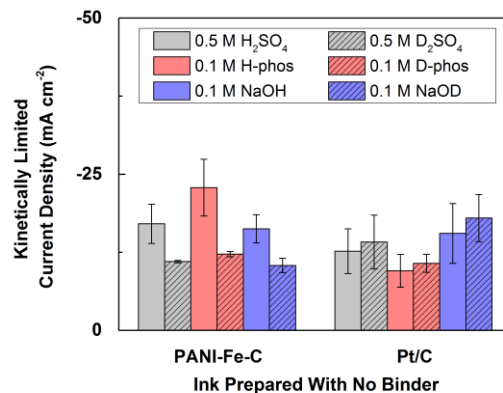


Figure 4.9 Bar graphs summarizing the kinetically limited current densities obtained from Koutecky-Levich analyses of O<sub>2</sub> reduction voltammograms for PANI-Fe-C, Pt/C and Pd/C with inks prepared with without binder in O<sub>2</sub>-saturated 0.5 M H<sub>2</sub>SO<sub>4</sub> (gray), 0.5 M D<sub>2</sub>SO<sub>4</sub> (gray with stripes), 0.1 M pH 7 phosphate buffer (red), 0.1 M pD 7 phosphate buffer (red with stripes), 0.1 M NaOH (blue), and 0.1 M NaOD (blue with stripes) solutions.

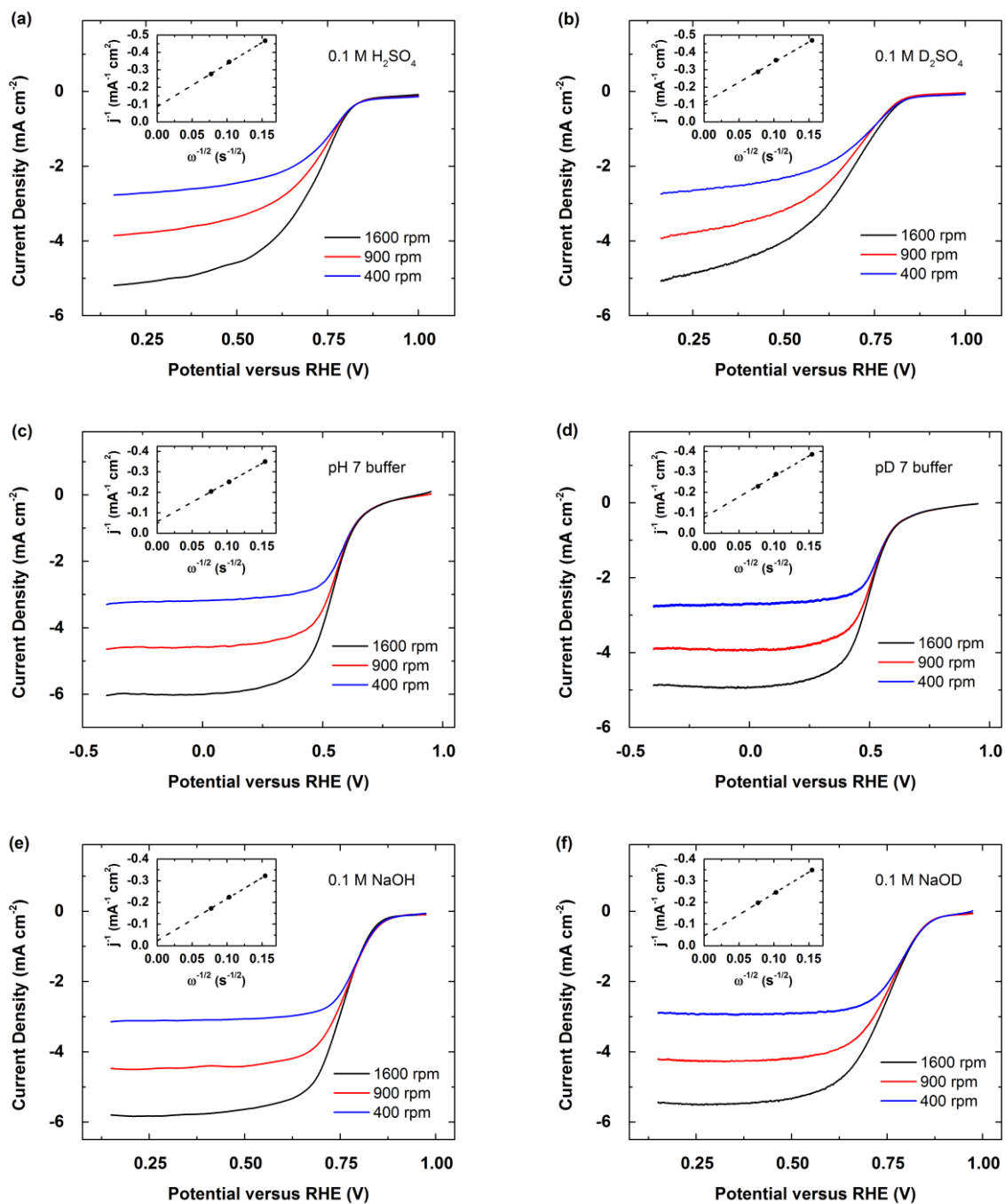


Figure 4.10 RDE voltammograms and Koutecky-Levich plots (insets) of PANI-Fe-C with inks prepared using Nafion 117 solution in EtOH in (a) pH 0.3, (b) pD 0.3, (c) pH 7, (d) pD 7, (e) pH 13, and (f) pD 13  $\text{O}_2$ -saturated solutions with a scan rate of 10 mV/s at 400 (blue), 900 (red), and 1600 (black) rpm.

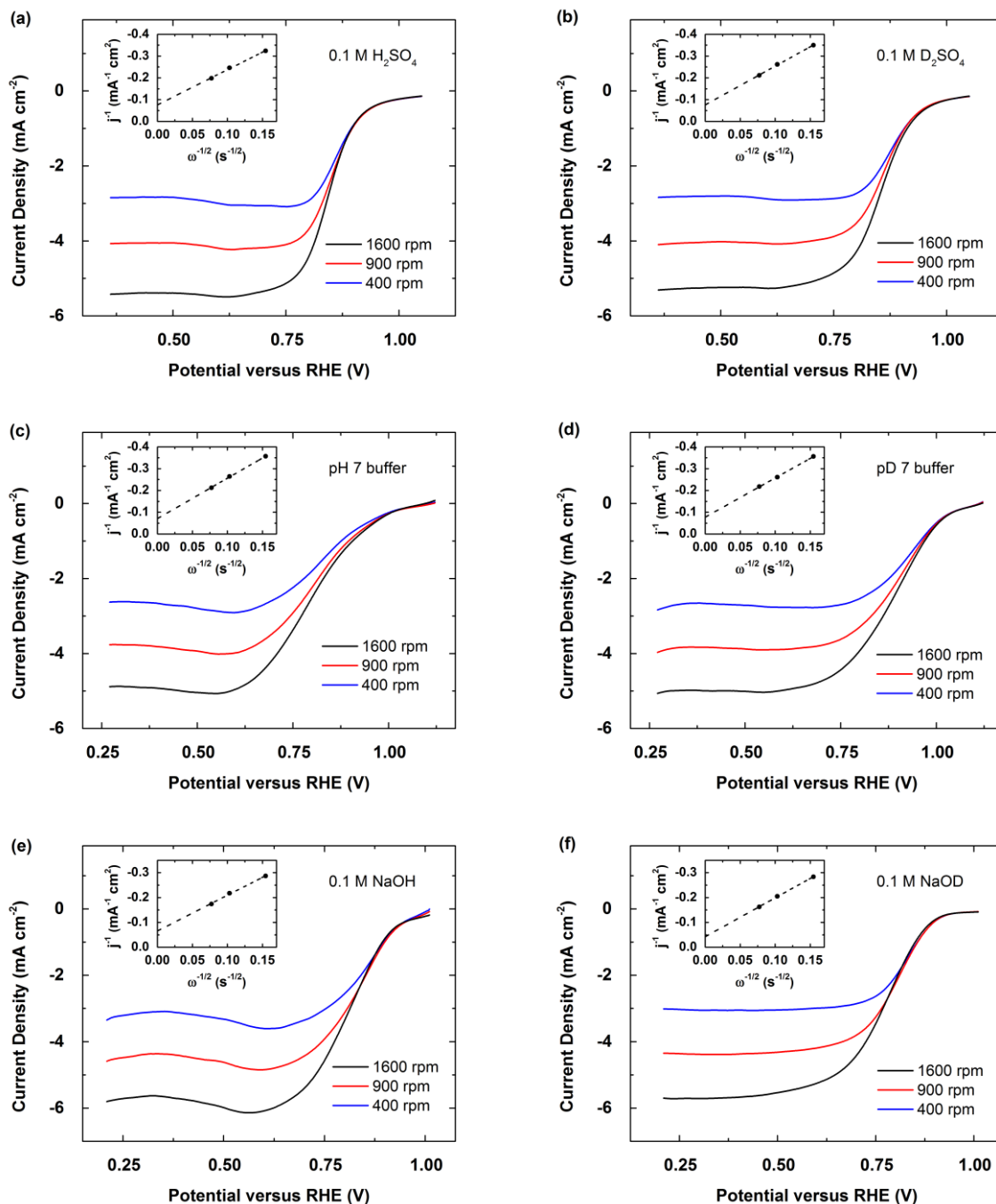


Figure 4.11 RDE voltammograms and Koutecky-Levich plots (insets) of 20 wt.% Pt supported on Vulcan XC-72 with inks prepared using Nafion 117 solution in EtOH in (a) pH 0.3, (b) pD 0.3, (c) pH 7, (d) pD 7, (e) pH 13, and (f) pD 13  $\text{O}_2$ -saturated solutions with a scan rate of 10 mV/s at 400 (blue), 900 (red), and 1600 (black) rpm.



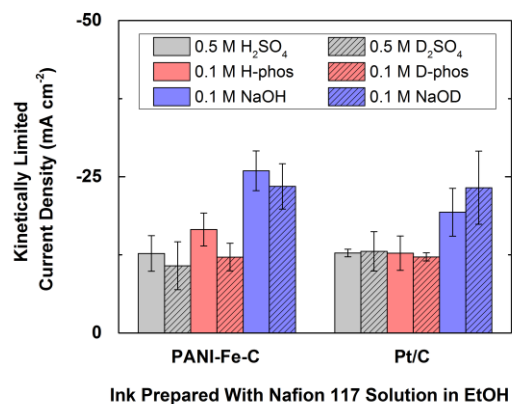


Figure 4.12 Bar graphs summarizing the kinetically limited current densities obtained from Koutecky-Levich analyses of O<sub>2</sub> reduction voltammograms for PANI-Fe-C and Pt/C with inks prepared using Nafion 117 solution in O<sub>2</sub>-saturated 0.5 M H<sub>2</sub>SO<sub>4</sub> (gray), 0.5 M D<sub>2</sub>SO<sub>4</sub> (gray with stripes), 0.1 M pH 7 phosphate buffer (red), 0.1 M pD 7 phosphate buffer (red with stripes), 0.1 M NaOH (blue), and 0.1 M NaOD (blue with stripes) solutions.

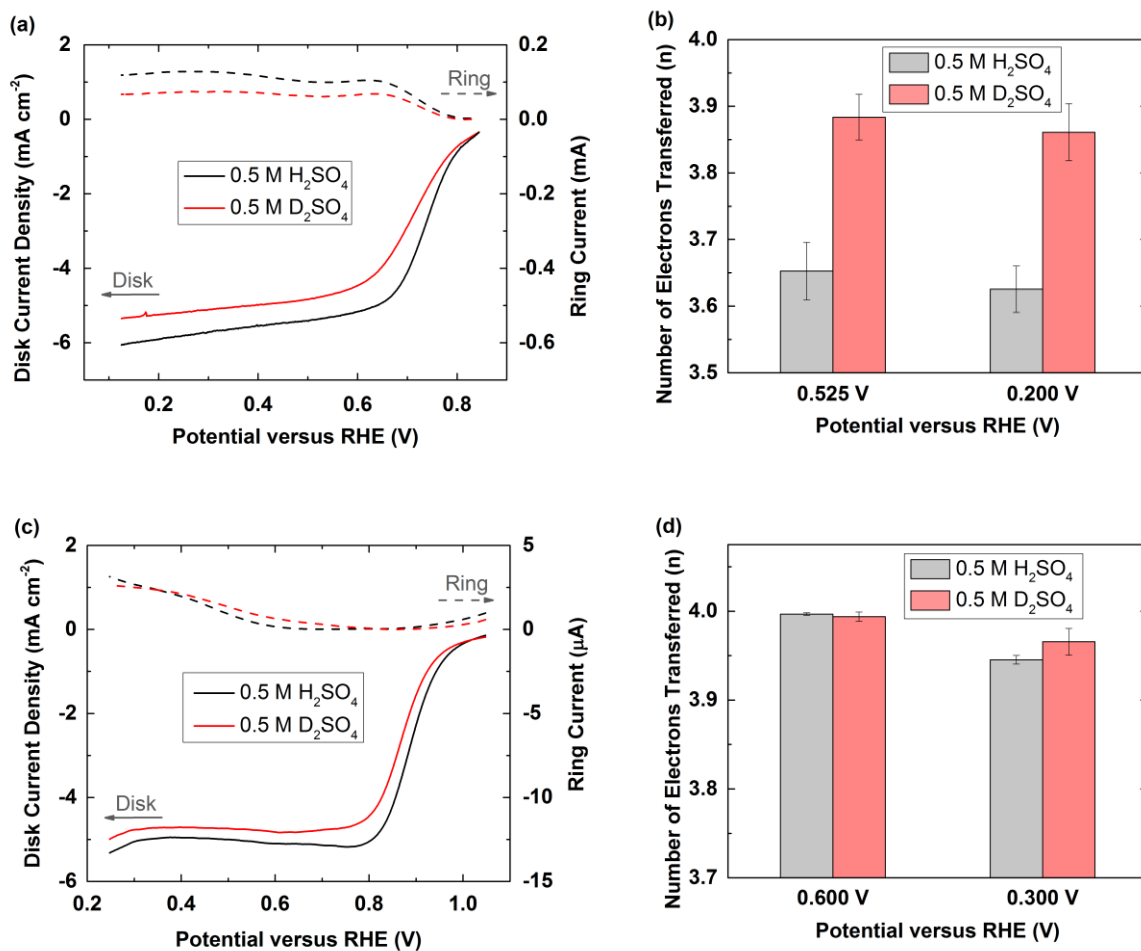


Figure 4.13 (a) Rotating ring-disk electrode (RRDE) experiments of PANI-Fe-C in 0.5 M H<sub>2</sub>SO<sub>4</sub> (black) and 0.5 M D<sub>2</sub>SO<sub>4</sub> (red) with a rotation rate of 1600 rpm at a scan rate of 10 mV s<sup>-1</sup>. Solid line = disk current density. Dashed line = ring current. (b) Number of electrons transferred calculated at two different potentials using the RRDE data shown in Figure 3a. (c) RRDE experiments of Pt/C in 0.5 M H<sub>2</sub>SO<sub>4</sub> (black) and 0.5 M D<sub>2</sub>SO<sub>4</sub> (red) with a rotation rate of 1600 rpm at a scan rate of 10 mV s<sup>-1</sup>. Solid line = disk current density. Dashed line = ring current. (d) Number of electrons transferred calculated at two different potentials using the RRDE data shown in Figure 3c.

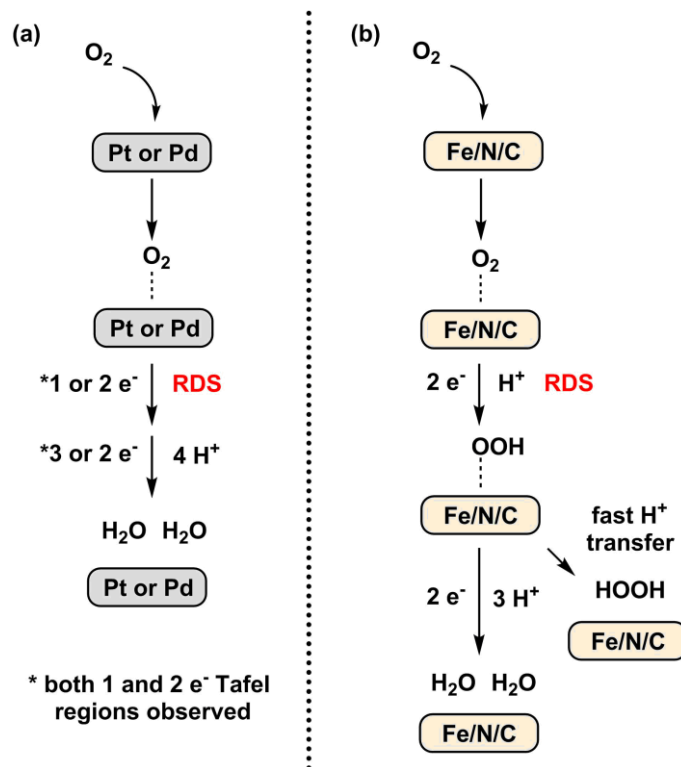


Figure 4.14 Possible mechanisms for the ORR on (a) precious metal and (b) non-precious metal materials. RDS is shown in red.

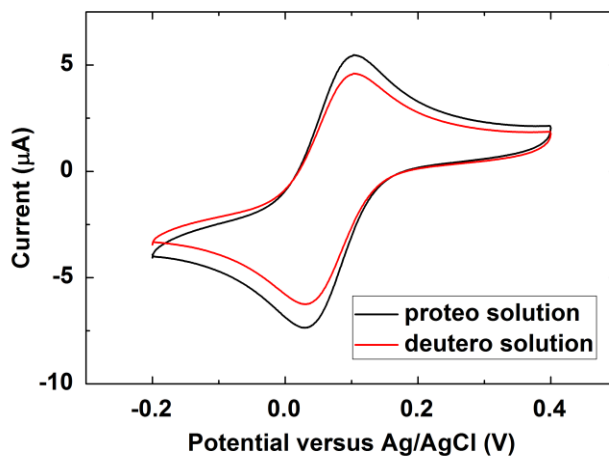


Figure 4.15 Cyclic voltammograms of 1 mM  $K_3Fe(CN)_6$  in proteo (black) and deuterio (red) solutions at a scan rate of  $100 \text{ mV s}^{-1}$ .

Table 4.1 Summary of the kinetic isotope effect of ORR catalyzed by PANI-Fe-C, Pt/C, and Pd/C in acidic (0.5 M H<sub>2</sub>SO<sub>4</sub>/D<sub>2</sub>SO<sub>4</sub>), neutral (0.1 M, pH/pD 7 phosphate buffer) and basic (0.1 M NaOH/NaOD) conditions.

<b>Catalysts</b>	<b>PANI-Fe-C</b>	<b>Pt/C</b>	<b>Pd/C</b>
Acidic	1.9 ± 0.5	1.1 ± 0.2	0.9 ± 0.4
Neutral	1.6 ± 0.3	1.0 ± 0.3	0.9 ± 0.4
Basic	1.8 ± 0.5	1.0 ± 0.3	1.0 ± 0.2

Table 4.2 Summary of the kinetic isotope effect of ORR catalyzed by PANI-Fe-C, Pt/C, and Pd/C with inks prepared without binder in acidic (0.5 M H<sub>2</sub>SO<sub>4</sub>/D<sub>2</sub>SO<sub>4</sub>), neutral (0.1 M, pH/pD 7 phosphate buffer) and basic (0.1 M NaOH/NaOD) conditions.

<b>Catalysts</b>	<b>PANI-Fe-C</b>	<b>Pt/C</b>
Acidic	1.7 ± 0.3	1.0 ± 0.4
Neutral	2.1 ± 0.4	1.0 ± 0.3
Basic	1.7 ± 0.3	0.9 ± 0.4

Table 4.3 Summary of the kinetic isotope effect of ORR catalyzed by PANI-Fe-C and Pt/C with inks prepared using Nafion 117 solution in acidic (0.5 M H<sub>2</sub>SO<sub>4</sub>/D<sub>2</sub>SO<sub>4</sub>), neutral (0.1 M, pH/pD 7 phosphate buffer) and basic (0.1 M NaOH/NaOD) conditions.

<b>Catalysts</b>	<b>PANI-Fe-C</b>	<b>Pt/C</b>
Acidic	1.3 ± 0.5	1.1 ± 0.3
Neutral	1.5 ± 0.4	1.2 ± 0.3
Basic	1.2 ± 0.2	0.9 ± 0.3

## 4.6 References

- (1) Mayer, J. M.; Rhile, I. J. *BBA-Bioenergetics* **2004**, *1655*, 51.
- (2) Jaouen, F.; Proietti, E.; Lefevre, M.; Chenitz, R.; Dodelet, J.-P.; Wu, G.; Chung, H. T.; Johnston, C. M.; Zelenay, P. *Energy Environ. Sci.* **2011**, *4*, 114.
- (3) Katsounaros, I.; Cherevko, S.; Zeradjanin, A. R.; Mayrhofer, K. J. J. *Angew. Chem. Int. Ed.* **2014**, *53*, 102.
- (4) Zhang, J.; Xie, Z.; Zhang, J.; Tang, Y.; Song, C.; Navessin, T.; Shi, Z.; Song, D.; Wang, H.; Wilkinson, D. P.; Liu, Z.-S.; Holdcroft, S. *J. Power Sources* **2006**, *160*, 872.
- (5) Carmo, M.; Fritz, D. L.; Mergel, J.; Stolten, D. *Int. J. Hydrogen Energy* **2013**, *38*, 4901.
- (6) Gewirth, A. A.; Thorum, M. S. *Inorg. Chem.* **2010**, *49*, 3557.
- (7) Thorseth, M. A.; Tornow, C. E.; Tse, E. C. M.; Gewirth, A. A. *Coord. Chem. Rev.* **2013**, *257*, 130.
- (8) Tse, E. C. M.; Schilter, D.; Gray, D. L.; Rauchfuss, T. B.; Gewirth, A. A. *Inorg. Chem.* **2014**, *53*, 8505.
- (9) Wu, G.; More, K. L.; Johnston, C. M.; Zelenay, P. *Science* **2011**, *332*, 443.
- (10) Varnell, J. A.; Tse, E. C. M.; Schulz, C. E.; Fister, T. T.; Haasch, R. T.; Timoshenko, J.; Frenkel, A. I.; Gewirth, A. A. *Nat. Commun.* **2016**, DOI: [10.1038/ncomms12582](https://doi.org/10.1038/ncomms12582).
- (11) Tylus, U.; Jia, Q.; Strickland, K.; Ramaswamy, N.; Serov, A.; Atanassov, P.; Mukerjee, S. *J. Phys. Chem. C* **2014**, *118*, 8999.

- (12) Thorseth, M. A.; Letko, C. S.; Tse, E. C. M.; Rauchfuss, T. B.; Gewirth, A. A. *Inorg. Chem.* **2012**, *52*, 628.
- (13) Inaba, M.; Kinumoto, T.; Kiriake, M.; Umebayashi, R.; Tasaka, A.; Ogumi, Z. *Electrochim. Acta* **2006**, *51*, 5746.
- (14) Coms, F. D. *ECS Trans.* **2008**, *16*, 235.
- (15) Boulatov, R.; Collman, J. P.; Shiryayeva, I. M.; Sunderland, C. J. *J. Am. Chem. Soc.* **2002**, *124*, 11923.
- (16) Barile, C. J.; Tse, E. C. M.; Li, Y.; Sobyra, T. B.; Zimmerman, S. C.; Hosseini, A.; Gewirth, A. A. *Nat. Mater.* **2014**, *13*, 619.
- (17) Das, D.; Lee, Y.-M.; Ohkubo, K.; Nam, W.; Karlin, K. D.; Fukuzumi, S. *J. Am. Chem. Soc.* **2013**, *135*, 4018.
- (18) Masel, R. I. *Principles of Adsorption and Reaction on Solid Surfaces*; Wiley, 1996.
- (19) Nørskov, J. K.; Rossmeisl, J.; Logadottir, A.; Lindqvist, L.; Kitchin, J. R.; Bligaard, T.; Jónsson, H. *J. Phys. Chem. B* **2004**, *108*, 17886.
- (20) Christensen, N. J.; Fristrup, P. *Synlett* **2015**, *26*, 508.
- (21) Stamenkovic, V. R.; Fowler, B.; Mun, B. S.; Wang, G.; Ross, P. N.; Lucas, C. A.; Marković, N. M. *Science* **2007**, *315*, 493.
- (22) Fletcher, S. *J. Solid State Electrochem.* **2008**, *13*, 537.
- (23) Tse, E. C. M.; Gewirth, A. A. *J. Phys. Chem. A* **2015**, *119*, 1246.
- (24) Shinagawa, T.; Garcia-Esparza, A. T.; Takanabe, K. *Scientific Reports* **2015**, *5*, 13801.

- (25) Li, M. F.; Liao, L. W.; Yuan, D. F.; Mei, D.; Chen, Y.-X. *Electrochim. Acta* **2013**, *110*, 780.
- (26) Klinman, J. P. *FEBS Journal* **2014**, *281*, 489.
- (27) Nelson, S. D.; Trager, W. F. *Drug Metab. Dispos.* **2003**, *31*, 1481.
- (28) Conway, B. E.; Salomon, M. *J. Chem. Phys.* **1964**, *41*, 3169.
- (29) Salomon, M.; Conway, B. E. *Ber. Bunsen-Ges. Phys. Chem.* **1965**, *69*, 669.
- (30) Krishtalik, L. I. *Electrochim. Acta* **2001**, *46*, 2949.
- (31) Tse, E. C. M.; Hoang, T. T. H.; Varnell, J. A.; Gewirth, A. A. *ACS Catal.* **2016**.
- (32) Ghoneim, M. M.; Clouser, S.; Yeager, E. *J. Electrochem. Soc.* **1985**, *132*, 1160.
- (33) Gómez-Gallego, M.; Sierra, M. A. *Chem. Rev.* **2011**, *111*, 4857.
- (34) Saunders, W. H.; Melander, L. R. *Reaction Rates of Isotopic Molecules*; Wiley: New York, 1980.
- (35) Mei, D.; He, Z. D.; Zheng, Y. L.; Jiang, D. C.; Chen, Y.-X. *Phys. Chem. Chem. Phys.* **2014**, *16*, 13762.
- (36) Jiang, R.; Anson, F. C. *J. Electroanal. Chem. Interfacial Electrochem.* **1991**, *305*, 171.
- (37) Parthasarathy, A.; Srinivasan, S.; Appleby, A. J.; Martin, C. R. *J. Electrochem. Soc.* **1992**, *139*, 2530.
- (38) Strbac, S. *Electrochim. Acta* **2011**, *56*, 1597.
- (39) Liao, L. W.; Li, M. F.; Kang, J.; Chen, D.; Chen, Y.-X.; Ye, S. *J. Electroanal. Chem.* **2013**, *688*, 207.
- (40) Parthasarathy, A.; Martin, C. R.; Srinivasan, S. *J. Electrochem. Soc.* **1991**, *138*, 916.

- (41) Shinagawa, T.; Garcia-Esparza, A. T.; Takanabe, K. *Sci. Rep.* **2015**, *5*, 13801.
- (42) Ye, H.; Crooks, J. A.; Crooks, R. M. *Langmuir* **2007**, *23*, 11901.
- (43) Zurilla, R. W.; Sen, R. K.; Yeager, E. J. *J. Electrochem. Soc.* **1978**, *125*, 1103.
- (44) Ci, S.; Wu, Y.; Zou, J.; Tang, L.; Luo, S.; Li, J.; Wen, Z. *Chinese Sci. Bull.* **2012**, *57*, 3065.
- (45) Tse, E. C. M.; Barile, C. J.; Kirchschrager, N. A.; Li, Y.; Gewargis, J. P.; Zimmerman, S. C.; Hosseini, A.; Gewirth, A. A. *Nat. Mater.* **2016**, *15*, 754.
- (46) Huang, X.; Zhao, Z.; Cao, L.; Chen, Y.; Zhu, E.; Lin, Z.; Li, M.; Yan, A.; Zettl, A.; Wang, Y. M.; Duan, X.; Mueller, T.; Huang, Y. *Science* **2015**, *348*, 1230.
- (47) Cao, L.; Mueller, T. *J. Phys. Chem. C* **2015**, *119*, 17735.
- (48) Olson, T. S.; Pylypenko, S.; Fulghum, J. E.; Atanassov, P. *Journal of The Electrochemical Society* **2010**, *157*, B54.
- (49) Ramaswamy, N.; Tylus, U.; Jia, Q.; Mukerjee, S. *Journal of the American Chemical Society* **2013**, *135*, 15443.
- (50) Bard, A. J.; Parson, R.; Jordan, J. *Standard Potentials in Aqueous Solution*; Marcel Dekker, Inc., 1985.
- (51) Weaver, M. J.; Nettles, S. M. *Inorg. Chem.* **1980**, *19*, 1641.
- (52) Zitolo, A.; Goellner, V.; Armel, V.; Sougrati, M.-T.; Mineva, T.; Stievano, L.; Fonda, E.; Jaouen, F. *Nat. Mater.* **2015**, *14*, 937.
- (53) Ivanov, E. V.; Abrosimov, V. K. *Russ. J. Gen. Chem.* **2005**, *75*, 1851.
- (54) Battino, R.; Rettich, T. R.; Tominaga, T. *J. Phys. Chem. Ref. Data* **1983**, *12*, 163.
- (55) Asperger, S. *Chemical Kinetics and Inorganic Reaction Mechanisms*; Springer US: New York, 2011.



## Chapter 5

### Investigating the Corrosion Behavior and Mechanical Properties of Al-Alloy “Covetics”

Reprinted from Varnell, J.A., Bakir, M., DiAscro, A.M., Nilufar, S., Jasiuk, I., Gewirth, A.A

*Submitted.*

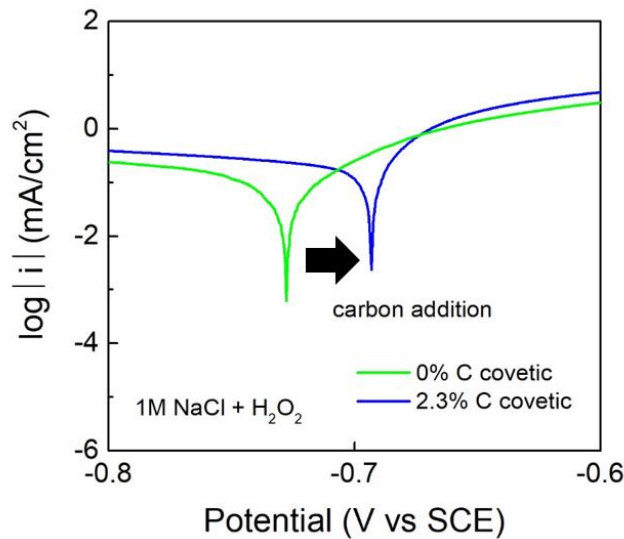


Figure 5.1 Graphical summary of the experimental results described in this work.

### 5.1 Introduction

The formation and processing of metal alloys allows significant enhancements in the desirable properties of the base metal. For example, the carburization of steel strongly influences its strength and ductility, and also increases its resistance to oxidation.<sup>1,2</sup> Metal alloys are widely utilized in the building of infrastructure such as for the transmission of electricity in high-voltage

power lines, for the fabrication of high-performance electronics, and for the construction of lightweight aerospace, naval, and automotive vehicles.

Aluminum (Al) and its alloys are of interest because of their increasingly significant role in applications requiring lightweight yet strong building materials that are resistant to chemical attack and degradation. The corrosion of many Al alloys has been investigated previously to understand the mechanism of corrosion and corrosion resistance. Typically, Al and its alloys undergo pitting corrosion in the presence of chlorine ions ( $\text{Cl}^-$ ) in which local breakdown of the metal-oxide passivation layer results in the dissolution of the Al surface.<sup>3-7</sup> Such pitting corrosion is of major concern due to the high  $\text{Cl}^-$  levels found in the environments in which these metals are typically used, such as in seawater and on roadways. For Al alloys, chromate conversion coating is commonly used to protect the surface.<sup>4</sup> However, this process involves the use of chromic acid which is toxic and highly regulated. Thus, alternative methods to protect Al alloys from corrosion are desirable.<sup>8</sup>

Many attempts to manufacture composite materials by combining carbon fillers and metallic Al powders have recently been described.<sup>9</sup> These include mixing graphene and carbon nanotubes with powders of pure Al or Al-alloys and applying various processing techniques including ball milling, binder-assisted mixing, hot-pressing/sintering, high-pressure torsion, friction stir processing, and plasma spray forming.<sup>10-17</sup> The resulting composite materials consist of a mixture of carbon structures and Al particles because the solubility of carbon in Al is extremely low.<sup>18</sup> Additionally, the presence of a carbide phase,  $\text{Al}_4\text{C}_3$ , has been observed for manufacturing processes which involve high temperatures, generally above 600 °C. For all of these methods the resulting composite material typically consists of interdispersed carbon structures within the Al alloy.

Recently, a new method for incorporating carbon into Al alloys was developed by Third Millennium Materials, LLC, referred to as “electrocharging assisted bulk processing”.<sup>19,20</sup> This process, which involves adding carbon to the molten metal and applying a high electrical current while stirring the mixture, was used to incorporate carbon into metals and alloys for which the predicted solubility of carbon is low, such as Ag, Cu, and Al.<sup>19-30</sup> It is hypothesized that the high currents used in this process result in the ionization of carbon atoms within the melt. This ionization could enable the formation of covalent bonds between the carbon and the metal, for which these “covetic” materials have been named. The formation of covetics in Ag, Cu, and Al has been studied by diffraction, electron energy-loss spectroscopy (EELS), Kelvin force-probe microscopy, and X-ray photoelectron spectroscopy (XPS).<sup>19,26,27</sup> Additionally, multiple density functional theory (DFT) calculations have suggested the possibility of forming direct bonds between C and metal atoms, particularly for C atoms at defect sites and at the edge of graphene-like sheets.<sup>19,26,31</sup>

The covetics obtained through the electrocharging process represent a new class of metallic/carbon nanostructured materials, in contrast to previously studied composite materials.<sup>32,33</sup> It is expected that covetics, which ostensibly feature covalent bonds between the metal and carbon, could exhibit enhanced properties relative to the composites. Indeed, studies showed that covetic mechanical properties, such as hardness and tensile strength, are improved from the pure alloy upon carbon addition.<sup>21,22,25</sup> Covetics also exhibit higher thermal stability and a higher melting temperature compared to the pure alloy.<sup>19,21,22</sup> Efforts on the characterization of covetics and the enhanced properties of covetics are summarized in a recent review.<sup>2</sup>

It has also been suggested that covetics could have the desirable properties of improved corrosion resistance and resistance to oxidation.<sup>28,34</sup> Previous studies demonstrated that graphene can act as a barrier to prevent the oxidation of a Cu surface and a similar resistance to oxidation was observed for a Cu covetic.<sup>30,35,36</sup> However, a full experimental investigation of the corrosion properties and an understanding of how the covetic process influences these properties is lacking. As previously proposed, it is likely that the changes induced during the process used to make the covetics could affect their corrosion properties, particularly if the surface exhibits increased carbon content and/or there is a covalent interaction between the Al and any putative C.<sup>30,37</sup> For typical Al alloys, the addition of alloying elements results in the formation of secondary phases which vary in composition from the bulk material.<sup>38</sup> The presence of these enriched phases is known to affect the corrosion properties of alloy materials and anodic dissolution methods are sometimes employed to reveal the composition of different secondary phases.<sup>38,39</sup> In this study, we present the results of corrosion tests for an Al 6061-based covetic with and without carbon added during the manufacturing process, and observe that the covetic with carbon exhibits a significant increase in corrosion potential. We also confirm improvements in the mechanical properties of the covetic with carbon added and provide detailed physical characterization to help reveal the origin of the observed changes in both mechanical properties and corrosion behavior.

## **5.2 Results**

### **5.2.1 Corrosion Testing and Surface Characterization**

In order to evaluate the corrosion behavior of the Al alloy and Al covetic samples we used linear polarization (LP) using the conditions for the “oxygenated saltwater test” and in acidic conditions using 0.1 M HCl. **Figure 5.2** shows the linear polarization curves obtained for the Al covetic (AC) samples and two reference samples: Al alloy (AA) 6061-T6 and AA 3003.

The corrosion potential ( $E_{\text{corr}}$ ) for each sample was determined from the polarization curves using Tafel fitting.<sup>40,41</sup> The  $E_{\text{corr}}$  values for each sample are given in **Table 5.1**. From these results, we observe that the 2.3% covetic exhibits a  $E_{\text{corr}}$  approximately 30-40 mV higher than the 0% covetic. The  $E_{\text{corr}}$  of the 2.3% covetic is also higher than the corresponding values measured for the Al 6061-T6 and Al 3003 samples.

To confirm the results of the LP tests, the open circuit potential (OCP) was recorded for a period of 60 minutes for each of the samples as shown in **Figure 5.3**. **Table 5.2** provides the corresponding values of  $E_{\text{corr}}$  as determined by averaging the OCP over a period of 30 minutes, following a previously established method.<sup>42,43</sup> The values of  $E_{\text{corr}}$  as determined from both the linear polarization curves and open circuit potentials agree closely. The values of  $E_{\text{corr}}$  obtained for the reference samples are consistent with the values reported in literature (**Table 5.3**).<sup>42</sup>

In order to compare the effects of the covetic process and addition of carbon on the corrosion properties of the samples, additional corrosion parameters were calculated by fitting the polarization curves. The corrosion current density ( $i_{\text{corr}}$ ), anodic and cathodic Tafel slopes ( $\beta_a$  and  $\beta_c$ ), and polarization resistance ( $R_p$ ) for each sample are given in **Table 5.4**.<sup>40,41</sup> These results indicate that the corrosion current density measured at  $E_{\text{corr}}$  in both 0.1 M HCl and 1 M NaCl + H<sub>2</sub>O<sub>2</sub> is higher for the 2.3% covetic than for the other samples. The lower  $R_p$  value for the 2.3% covetic indicates that the 2.3% covetic is more easily corroded near its corrosion potential as compared to the rest of the samples. Interestingly, in acidic conditions the anodic branch of the polarization curve for the 2.3% covetic is shifted slightly to lower current density than the other samples as a result of the increase in  $E_{\text{corr}}$ . This shift indicates that at potentials above  $E_{\text{corr}}$  the corrosion rate is reduced for the 2.3% covetic as compared to other samples. In acidic conditions the slopes of the cathodic and anodic branches of the polarization curve are

higher for the 2.3% covetic than for the other samples, which suggests that there is a change in the kinetics of both the cathodic and anodic reactions resulting from the process of adding carbon. In 1 M NaCl +H<sub>2</sub>O<sub>2</sub> the slope of the cathodic branch increased slightly for the 2.3% covetic while the slope of the anodic branch decreased, suggesting that in these conditions the rate of the cathodic reaction was retarded while the anodic reaction (corrosion) was accelerated.

To explain the difference in the corrosion behavior of the 2.3% covetic, we investigated the surface composition of the covetic samples. **Figures 5.4a and 5.4b** show SEM images of the covetics following the corrosion tests. The 0% covetic exhibits a crystalline etching pattern while the 2.3% covetic has a rougher-looking surface. To probe the elemental composition of the samples after corrosion, EDS was used at two different accelerating voltages as shown in **Figures 5.4c and 5.4d**. Interestingly, these results indicate that the surface of the 2.3% covetic after corrosion is enriched with Si, Cu, Mn, and Ti. XPS was also used to interrogate the surface composition of the samples before and after the corrosion tests as shown in **Figure 5.5**. In agreement with the EDS results, XPS also indicates that the surface of the 2.3% covetic contains Si, Cu and Mn. The elements found on the surface of the 2.3% covetic are all present in the Al 6061 parent material used to form the covetic.<sup>6</sup> The enrichment of these elements on the surface of the 2.3% covetic after corrosion suggests that the material is not homogeneous and that the composition of the material is altered. Since the 0% covetic does not exhibit the same increase in corrosion potential, it is evident that the addition of carbon to the covetic is necessary to promote this change in composition.

To further study the surfaces of the samples XRD was performed before and after corrosion. **Figure 5.6** shows crystallographic morphologies of both 0% and 2.3% covetics. In both samples the crystal structure order of the base Al matrix was preserved. In addition, the 0%

covetic demonstrated a polycrystalline morphology where the (111) peak intensity varied with respect to other peaks as the sample was rotated to different orientations. On the other hand, the 2.3% covetic possessed a preferred grain orientation where structural order did not display this modulation effect. Additionally, broadening in the (111) peak was observed for the 2.3% covetic. The peak widths were used to determine the average grain sizes and lattice constants for each material by using the Scherer formula.<sup>36</sup> The average grain size for the 2.3% covetic was  $170 \pm 4 \text{ \AA}$  as compared to an average grain size of  $232 \pm 27 \text{ \AA}$  for the 0% covetic. From these values, it is clear that the surface of the 2.3% covetic has generally smaller grains than the 0% covetic. A previous study also observed smaller grain size resulting from the process used to make the covetics.<sup>22</sup> The presence of smaller grains also explains the preferential alignment of the grains in the 2.3% covetic.<sup>44,45</sup> However, the lattice constants for the 2.3% and 0% covetics were determined to be  $4.04524 \pm 0.00121 \text{ \AA}$  and  $4.04841 \pm 0.00456 \text{ \AA}$ , respectively. These lattice constants are identical within error which suggests that the 2.3% and 0% covetics have a similar metallic-alloy structure. We note that no characteristic peaks for Al-carbides or for carbon were observed in the XRD spectra in any of the samples. For the case of the 2.3% covetic, this lack could indicate either that the carbon is well dispersed into the Al matrix via the electrocharging process, or that carbon is not present.

Finally, we carried out thermogravimetric analysis (TGA) on the 0% and 2.3% covetic samples. **Figure 5.7** displays the temperature-ramp of the covetics carried out using TGA. The 0% covetic exhibited mass uptake with a small slope from the adsorption of  $\text{N}_2$  at elevated temperature, which corresponds to ca. 0.1 % mass increase up until 800 °C. This trend was consistently reproduced through application of two subsequent heating cycles. However, the 2.3% covetic yielded significant mass reduction associated with thermal degradation until about

660 °C within the vicinity of melting point of the Al matrix. The mass loss was measured to be between 0.2 and 0.8 % of the initial mass of the sample. Decomposition started immediately during the thermal cycle, indicating that the observed mass loss is likely a consequence of the presence of water physically or chemically adsorbed to the transition metal oxides present in the 2.3% sample.<sup>46</sup> **Figure 5.8** shows the degradation rate curve for the covetic samples, with the curve for the 2.3% covetic exhibiting a degradation rate peak at low temperatures which is a characteristic of the loss of water.<sup>47</sup> Following the initial mass loss, the thermal curve took a positive slope similar to the 0% covetic. Likewise, a second cycle heating curve closely followed thermal behavior of the 0% covetic. We note that the TGA samples were freshly cut and not corroded before heating, so the observed mass loss likely corresponds to a phase found within the bulk composition and not only on the surface.

### 5.2.2 Mechanical Properties of Covetic Materials

In addition to corrosion testing we also investigated mechanical properties of the covetic materials. **Figure 5.9** shows representative compressive stress-strain curves of the 0% and 2.3% covetics. The 0% covetic displays a large plastic deformation domain following an initial elastic regime, which agrees well with the characteristic compressive behavior of Al samples.<sup>48</sup> The 2.3% covetic yielded substantially improved compressive strength relative to the 0% covetic. Increasing compressive stress applied on the 2.3% covetic was sustained until the formation of fracture at around  $407.3 \pm 25.4$  MPa and  $31.04 \pm 5.8\%$  strain-to-failure ratio. Hence, the 2.3% covetic enabled dramatically increased deformation energy absorption, as indicated by the toughness. The fracture formation under compression with the 2.3% covetic is a clear indication of a brittle morphology when compared to the completely plastic behavior of the 0% covetic. Additionally, as demonstrated in **Table 5.5**, both Rockwell and Vickers hardness values



measured on the 2.3% covetic notably increased with respect to the 0% covetic. Namely, the Rockwell and Vickers hardnesses improved by 10% and 51%, respectively, for the 2.3% covetic.

The reduced grain size in the 2.3% covetic relates directly to the enhancement in mechanical properties through the Hall-Petch relation.<sup>49</sup> The Hall-Petch model suggests that increases in strength are expected to vary inversely with the square root of the grain size. Consequently, the prediction is that the 2.3% covetic should exhibit a strength slightly larger than that seen in the 0% covetic due to the marginally reduced grain size. However, the actual increases in the yield and ultimate strengths in the 2.3% covetic material are almost four-times until fracture. Thus, an additional strengthening mechanism is required to fully describe the large increase in compressive strengths observed for the 2.3% covetic.

### **5.3 Discussion**

Our findings reveal that the corrosion potential is shifted to a more positive potential for the 2.3% covetic with carbon added via the electrocharging assisted process. Despite this shift, the corrosion current density at  $E_{\text{corr}}$  is increased in the 2.3% covetic as compared to the 0% covetic and reference Al 3003 and Al 6061-T6 samples. Using several methods to study the materials before and after the corrosion tests we observe key differences between the 0% covetic and the 2.3% covetic. Surface characterization using SEM, EDS, and XPS indicates that the surface composition of the 2.3% covetic is different after corrosion, containing a higher concentration of several elements present in the parent material including Si, Ti, Mn, and Cu. The presence of these elements has been found to play a significant role in the corrosion behavior of Al alloys in agreement with the data that we report.<sup>6</sup> Additionally, previous work indicates that the presence of a secondary phase within an Al alloy containing Cu, Mn, and Si can greatly affect the corrosion properties of the material.<sup>39</sup>

Additionally, we observe substantial improvements in the mechanical properties of the 2.3% covetic. In particular, the compressive strength is improved by four-fold in the covetic, which also dramatically enhanced the materials toughness. Additionally, the HRB and VHN hardness values of the covetics increased by 10% and 51%, respectively. We show that the average grain size for the 2.3% covetic is smaller than that of the 0% covetic. As expected, the reduction in grain size corresponds to an increase in the compressive strength and hardness for the 2.3% covetic, in agreement with previous reports.<sup>21,22,25</sup> However, the improvements in the mechanical properties observed for the 2.3% covetic are larger than would be expected from the decrease in grain size alone. From the corrosion studies and sample characterization, the change in composition of the alloy phases present after addition of carbon further explains the increased strength and hardness of the 2.3% covetic.<sup>1,50</sup>

Compositional differences within Al alloys are commonly observed due to secondary phase formation and as a result of processing, such as during heat treatments, aging, and welding.<sup>4,38,39</sup> Due to the high temperature and electrical current used to manufacture the covetic samples it is extremely likely that similar changes in the local composition of the alloy have occurred for the covetic samples. However, since the changes in corrosion potential, mechanical strength, and hardness are only observed for the 2.3% covetic it is apparent that the addition of carbon is required to facilitate these compositional changes. Carbon interacts strongly with oxygen and as carbon is added oxygen atoms may also be introduced into the molten covetic material. The O interacts strongly with the other elements present in the melt and as the covetic is cooled phase separation occurs. This results in changes to the phase composition within the material, increasing the presence of oxides of Al, Si, Mn, Ti, and Cu.

Previous studies on covetic materials suggest that carbon incorporation into the covetic material results in graphene-like nanoribbons, observed using techniques such as Raman and EELS mapping.<sup>19,25-27</sup> Such possibilities have been supported by DFT studies which show that graphene-like carbon can be directly bonded to Al atoms in the alloy through the formation of covalent bonds between carbon and Al.<sup>19,26,31</sup> However, in our studies we did not specifically observe the incorporation of carbon into the 2.3% covetic. All of the samples examined by XPS exhibited a peak around 284 eV from carbon on the surface. The carbon peak was more pronounced before the corrosion tests, but was still present on all samples after corrosion, even those not intentionally doped with carbon. In our case, we attribute this peak to residual surface contamination, unrelated to the incorporation of carbon into the covetic materials. For the covetic samples we studied any incorporated carbon would be difficult to quantify since the amount of carbon present is expected to be very close to or below the normal detection limits of XPS (ca. 2%).<sup>51</sup>

In summary, we show that changes in the composition of alloy phases with elevated amounts of O, Si, Ti, Mn, and Cu are induced by the addition of carbon during the electrocharging assisted process. We further show that these compositional changes are more evident on the surface of the material after corrosion testing, forming a layer which increases the corrosion potential but also the corrosion current density. Additionally, we observe that the mechanical properties including the compressive strength and hardness are also enhanced by the addition of carbon in the 2.3% covetic. We attribute the origin of these improvements to the altered phase composition within the covetic material and also to the smaller grain size. Understanding the corrosion behavior and mechanical properties of covetic materials is important for potential applications within manufacturing and construction industries. Our

findings suggest that covetics prepared via the electrocharging-assisted process could be promising candidates for application as robust as lightweight building materials where corrosion may be an issue. We believe that further research to gain a better understanding of the processing and characteristics of covetic materials could lead to further control and improvement of their properties and help to accelerate their commercialization.

## 5.4 Experimental Methods

*Sample Preparation-* Al 3003 samples were obtained from McMaster Carr (product number 8973K87). Al 6061-T6 (the parent material for the covetic) and the covetic Al 6061 samples were received from Third Millennium Materials (TMM) LLC, Waverly, OH. Covetic Al 6061 samples were prepared as described in previous work.<sup>2,26,27</sup> One material was prepared using the covetic process but without the addition of any carbon (“0% covetic”, “AC 0% C”) and one was prepared by adding 2.3 wt % carbon (“2.3% covetic”, “AC 2.3% C”) during manufacturing. We note that these carbon amounts are those reported by manufacturers and they may not be the actual carbon contents incorporated in the covetic materials. All samples were cut into disks with diameter = 1 cm. Before characterization and corrosion testing one surface of each sample was sanded using 220 grit aluminum oxide sandpaper to remove surface contamination and passive oxide layers followed by progressive polishing using 1.0  $\mu\text{m}$  to 0.25  $\mu\text{m}$  alumina polish. After polishing, samples were sonicated in Milli-Q (Millipore) water and thoroughly rinsed. Samples characterized after corrosion tests were first thoroughly rinsed with Milli-Q water.

*Chemicals and Reagents-* Electrolyte solutions were prepared using NaCl (ACS reagent  $\geq 99\%$ , Sigma-Aldrich),  $\text{H}_2\text{O}_2$  (ACS reagent, 30% solution, Macron), HCl (ACS reagent, Macron), and 18.2  $\text{M}\Omega\cdot\text{cm}$  Milli-Q water (Millipore). All chemicals were used as received. For

experiments following ASTM G69 (“oxygenated saltwater test”), 0.9 mL of 30% H<sub>2</sub>O<sub>2</sub> (ACS reagent, Macron) was added to 100 mL of 1 M NaCl prior to beginning the corrosion test.<sup>42,43</sup> For all experiments fresh electrolyte was used, taken from the same stock solution to ensure consistency in the results.

*Corrosion Testing-* Corrosion tests were carried out at room temperature using a single compartment cell exposed to air with Al samples attached to a steel rod by conductive double-sided Cu tape and suspended using a hanging meniscus configuration. The Al samples were used as the working electrode with a Saturated Calomel Electrode (SCE, Koslow Scientific) used as the reference electrode and a graphite rod used as the counter electrode. Typically, the open circuit potential (OCP) was monitored and allowed to stabilize over a period of 30-60 minutes before data was collected.<sup>42</sup> Then OCP was recorded for 1 hour before beginning linear polarization (LP) testing. LP was performed using a potential range of  $\pm 250$  mV of the OCP with a scan rate of 60 mV/min.<sup>40</sup> Tafel fitting was performed using EC-Lab software.<sup>41</sup> OCP measurements were taken using a CHI 760C (CH Instruments) and LP measurements were taken using a SP-150 (Biologic Science Instruments).

*Mechanical Properties Testing-* The compressive properties of the Al covetic samples were measured via a compressive test using a load frame (4483 Load Frame, Instron Testing Systems) with a constant crosshead speed of 0.05 mm/min. The samples were machined to cylindrical shapes with a diameter of 5 mm and a height of 10 mm. Three samples of each covetic material (0% and 2.3%) were tested. The measurements were carried out in accordance with the ASTM E9 standard.<sup>52</sup> Rockwell hardness (HRB) was measured on both the longitudinal and transverse surfaces of the samples using a hardness tester (Wilson/ Rockwell Model 523). Vickers micro hardness (VHN) was also measured on both surfaces of the same samples by

applying a load of 3000 grams for 15 seconds using a microhardness tester (Shimadzu HMV-M3 Newage Testing Instruments). The reported hardness values were the averages of the total of ten measurements made on the two orthogonal surfaces (longitudinal and transverse) of each sample.

*Physical Characterization-* Scanning electron microscopy (SEM) was carried out using a Hitachi A-4700 high resolution microscope with an emission gun capable of 2.5 nm resolution. Energy dispersive x-ray spectroscopy (EDS) was carried out using an Oxford Instruments ISIS EDS X-ray system with accelerating voltages of 5 keV and 20 keV. X-ray photoelectron spectroscopy (XPS) was performed with a Kratos AXIS Ultra spectrometer with a monochromatic Al K $\alpha$  (1486.6 eV) X-ray source. X-ray diffraction was performed using an X-ray diffractometer (XRD) (Panalytical/Philips X'pert) with a Cu K-alpha source of 0.15148 nm wavelength operated at 45 kV/40 mA. The XRD spectra were obtained between diffraction angles of  $2\theta=5^\circ$  and  $2\theta=100^\circ$  with a scan step size of  $0.05^\circ$  and a dwell time of 2 s/step. For thermogravimetric analysis the covetic samples were cut into pieces weighing c.a. 50 mg, washed using isopropanol at least two times, and were allowed to dry. Then, they were placed in an alumina crucible and heating was carried out using TA Instruments Q-50 equipment with a temperature ramp heating cycle of  $10^\circ\text{C}/\text{min}$  up to  $800^\circ\text{C}$  under a constant  $\text{N}_2$  purge of 60 mL/min.

## 5.5 Figures and Tables

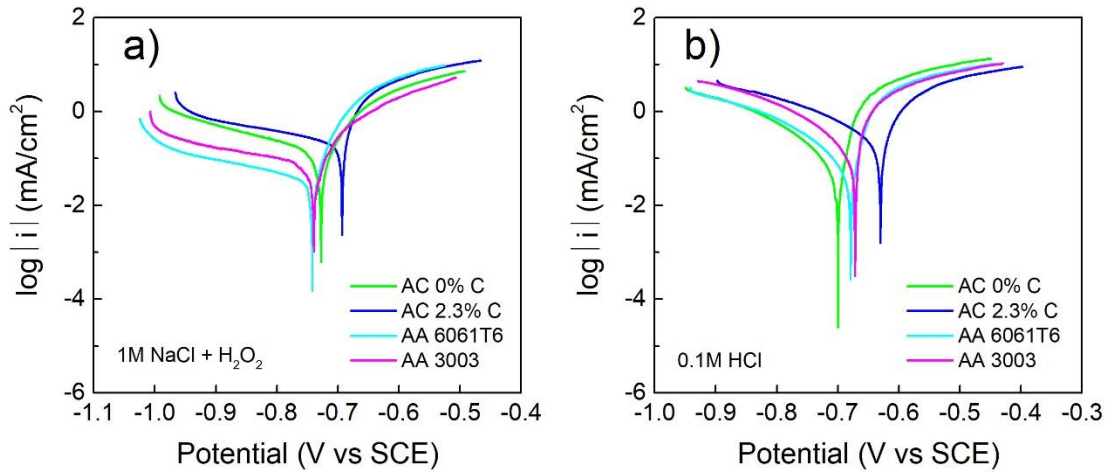


Figure 5.2 Linear polarization curves obtained for covetic materials and reference samples in the “oxygenated saltwater test” (1M NaCl + H<sub>2</sub>O<sub>2</sub>) (a) and 0.1M HCl (b).

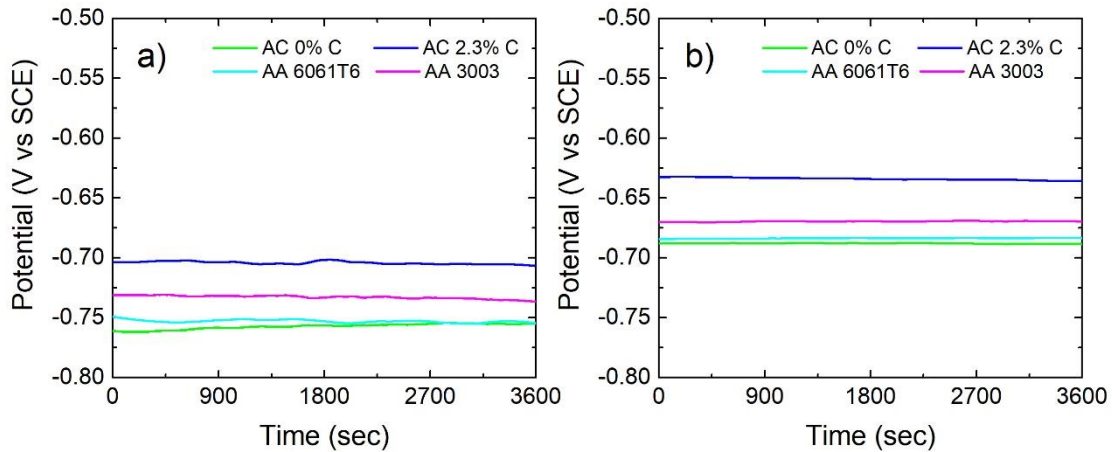


Figure 5.3 Open circuit potential (OCP) recorded for 60 minutes in 1M NaCl (a) and 0.1M HCl (b).

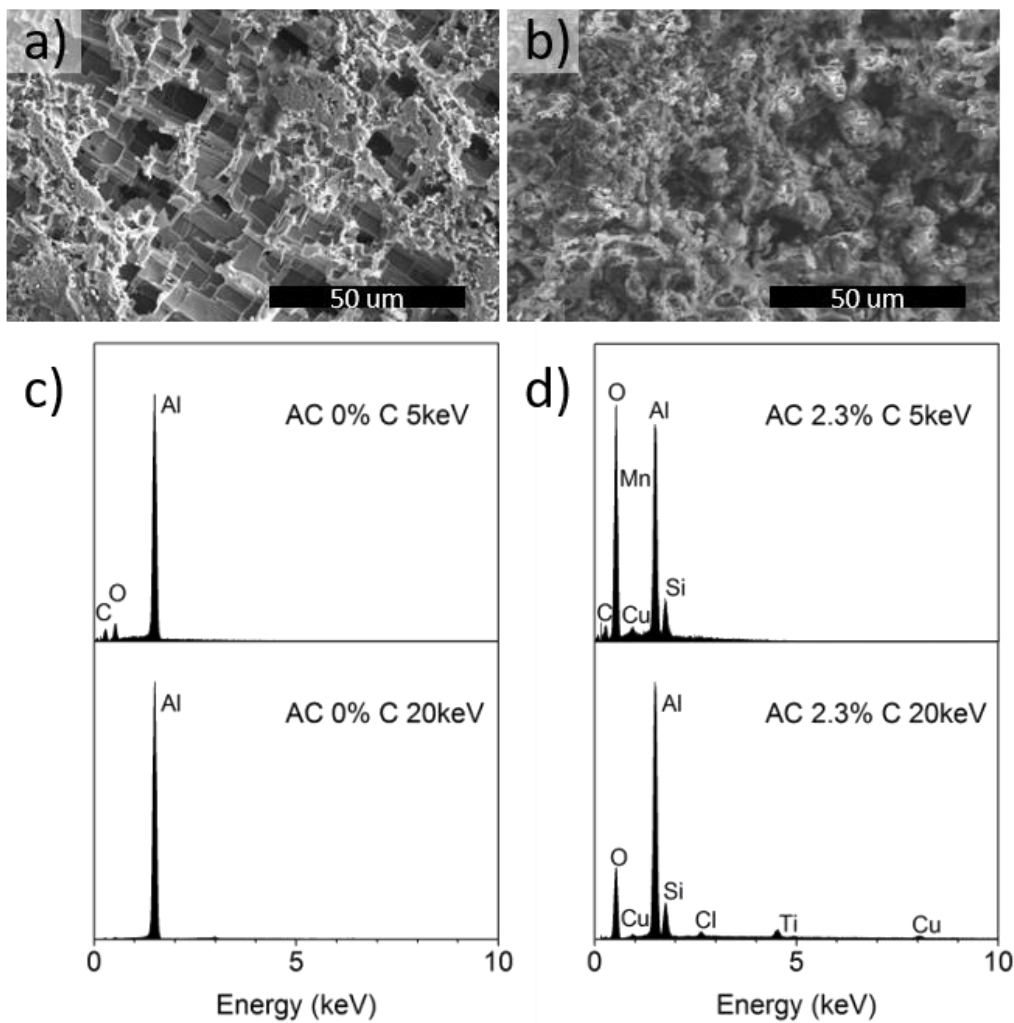


Figure 5.4 SEM images and EDS spectra recorded following corrosion tests for the 0% covetic (a, c) and the 2.3% covetic (b, d).



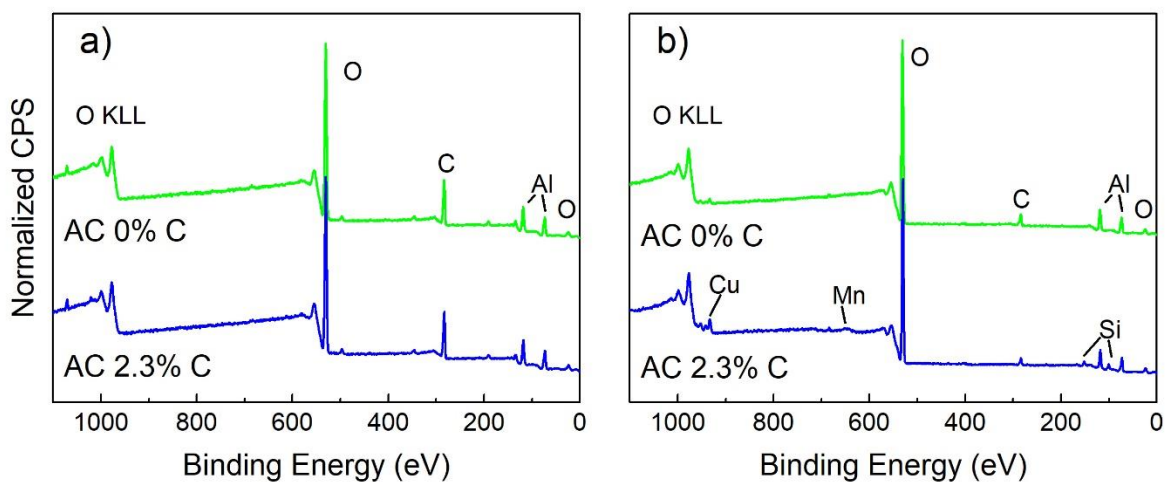


Figure 5.5 XPS survey spectra on Al covetic samples before (a) and after corrosion (b).

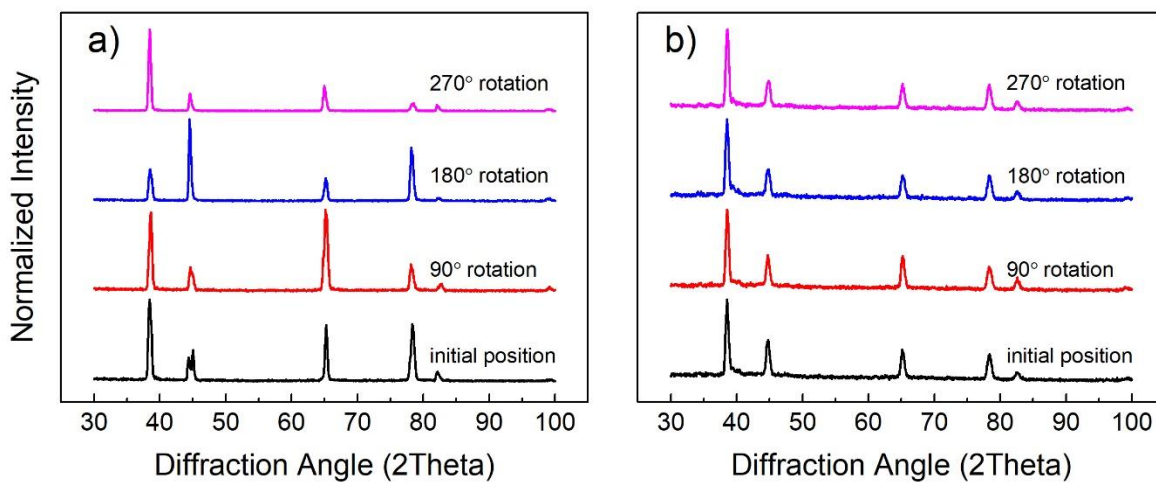


Figure 5.6 XRD spectra taken for the 0% covetic (a) and 2.3% covetic (b) following corrosion.

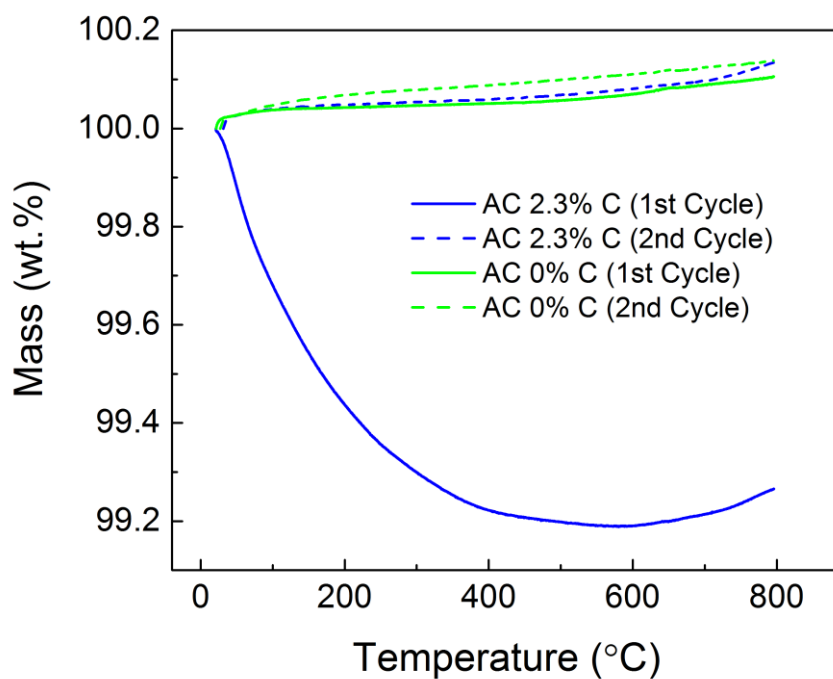


Figure 5.7 TGA curves for two heating cycles on the 0% and 2.3% covetic samples.

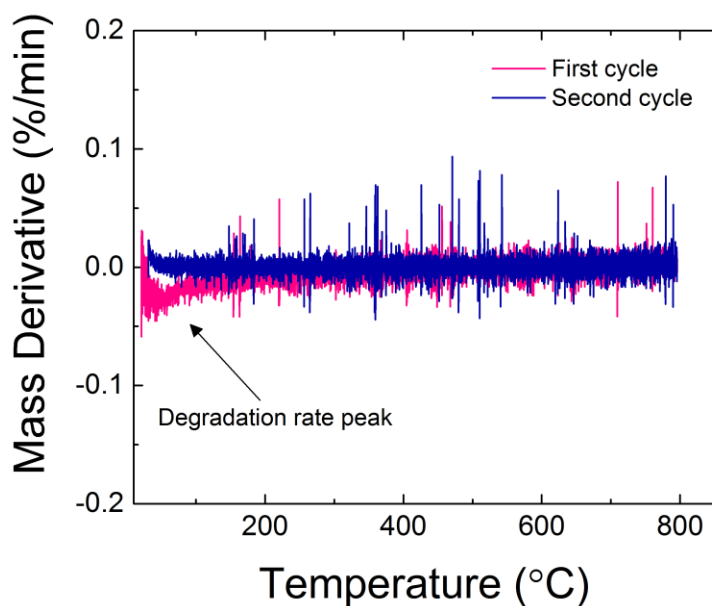


Figure 5.8 Degradation rate (DTG) curves for the 2.3% covetic.

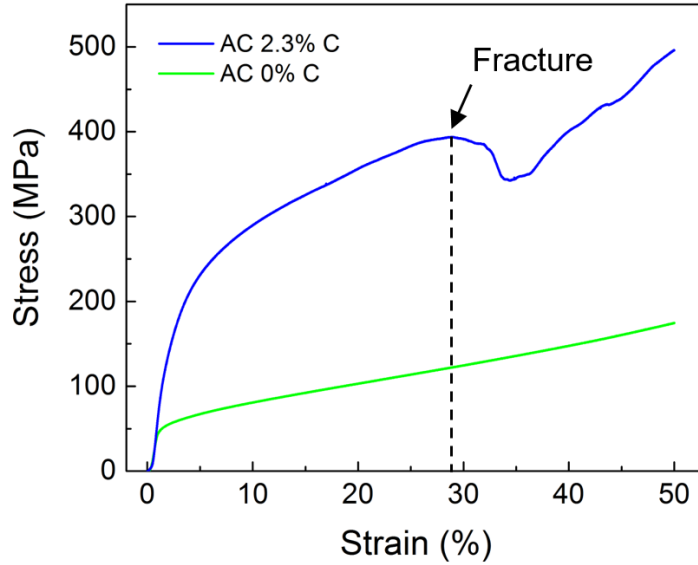


Figure 5.9 Compressive stress-strain curves for the 0% and 2.3% covetics.

Table 5.1 Corrosion potentials obtained for covetic materials and reference samples in 1M NaCl and 0.1M HCl as determined for the linear polarization curves.

<b>Aluminum Alloy Sample</b>	<b><math>E_{\text{corr}}</math> 1M NaCl + H<sub>2</sub>O<sub>2</sub></b> <b>(V vs SCE)</b>	<b><math>E_{\text{corr}}</math> 0.1M HCl</b> <b>(V vs SCE)</b>
Al 3003	-0.74	-0.67
Al 6061-T6	-0.74	-0.68
Al Covetic 0% C	-0.73	-0.70
Al Covetic 2.3% C	-0.69	-0.63

Table 5.2 Corrosion potentials obtained from averaging OCP values over the final 30 minutes of measurement.

<b>Aluminum Alloy Sample</b>	<b>E<sub>OCP</sub> NaCl (V vs SCE)</b>	<b>E<sub>OCP</sub> HCl (V vs SCE)</b>
Al 3003	-0.74	-0.67
Al 6061 T6	-0.75	-0.68
Al Covetic 0% C	-0.75	-0.69
Al Covetic 2.3% C	-0.70	-0.64

Table 5.3 Comparison of corrosion potentials for reference materials obtained from averaging OCP values over the final 30 minutes of measurement and given values from literature using the same method.

<b>Aluminum Alloy Sample</b>	<b>Measured E<sub>OCP</sub> NaCl (SCE)</b>	<b>Reference E<sub>OCP</sub> NaCl (SCE)<sup>42</sup></b>
Al 3003	-0.74	-0.74
Al 6061 T6	-0.75	-0.74

Table 5.4 Corrosion parameters calculated from polarization curves.

Electrolyte	Sample	$i_{\text{corr}}$ ( $\mu\text{A}/\text{cm}^2$ )	$\beta_a$ (mV/dec)	$\beta_c$ (mV/dec)	$R_p$ ( $\Omega$ )
0.1M HCl	Al 3003	75	21.9	76.7	66
	Al 6061-T6	42	24.5	81.7	148
	Al Covetic 0% C	42	24.8	76.4	136
	Al Covetic 2.3% C	273	49.3	192.8	70
1M NaCl + H <sub>2</sub> O <sub>2</sub>	Al 3003	90	61.7	582.8	316
	Al 6061-T6	38	34.4	405.6	337
	Al Covetic 0% C	181	76.3	412.2	186
	Al Covetic 2.3% C	232	32.9	493.2	53

Table 5.5 Hardness measurements for 0% and 2.3% covetic samples.

Aluminum Alloy Sample	Rockwell Hardness (HRB)	Vickers Hardness (kgf/mm <sup>2</sup> )
Al Covetic 0% C	38 ± 2.1	34 ± 3.2
Al Covetic 2.3% C	42 ± 1.8	65 ± 5.1

## 5.6 References

- (1) Smallman, R. E.; Ngan, A. H. W. *Physical Metallurgy and Advanced Materials (7th Edition)*; Elsevier, 2007.
- (2) Bakir, M., Jasiuk, I. *Advanced Materials Letters* **2017**, 8, 884.
- (3) Natishan, P. M.; O'Grady, W. E. *J. Electrochem. Soc.* **2014**, 161, C421.
- (4) Burleigh, T. D. In *Handbook of Aluminum* 2003; Vol. 2, p 421.

- (5) Hauffe, K. In *Corrosion Resistance of Aluminum and Its Alloys*; Bender, R., Ed.; Wiley: 2010.
- (6) Rockel, M. B. In *Corrosion Resistance of Aluminum and Its Alloys*; Bender, R., Ed.; Wiley: 2010, p 367.
- (7) Drodten, P. In *Corrosion Resistance of Aluminum and Its Alloys*; Bender, R., Ed.; Wiley: 2010, p 349.
- (8) Twite, R. L.; Bierwagen, G. P. *Progress in Organic Coatings* **1998**, *33*, 91.
- (9) Forrest, D. R. *Next Generation Electric Machines Workshop* **2015**.
- (10) Liao, J.; Tan, M.-J. *Powder Technology* **2011**, *208*, 42.
- (11) Bartolucci, S. F.; Paras, J.; Rafiee, M. A.; Rafiee, J.; Lee, S.; Kapoor, D.; Koratkar, N. *Materials Science and Engineering: A* **2011**, *528*, 7933.
- (12) Bastwros, M.; Kim, G.-Y.; Zhu, C.; Zhang, K.; Wang, S.; Tang, X.; Wang, X. *Composites Part B: Engineering* **2014**, *60*, 111.
- (13) Jeyasimman, D.; Sivaprasad, K.; Sivasankaran, S.; Narayanasamy, R. *Powder Technology* **2014**, *258*, 189.
- (14) Zhao, L.; Lu, H.; Gao, Z. *Advanced Engineering Materials* **2015**, *17*, 976.
- (15) Jeon, C.-H.; Jeong, Y.-H.; Seo, J.-J.; Tien, H. N.; Hong, S.-T.; Yum, Y.-J.; Hur, S.-H.; Lee, K.-J. *International Journal of Precision Engineering and Manufacturing* **2014**, *15*, 1235.
- (16) Laha, T.; Agarwal, A.; McKechnie, T.; Seal, S. *Materials Science and Engineering: A* **2004**, *381*, 249.
- (17) Laha, T.; Chen, Y.; Lahiri, D.; Agarwal, A. *Composites Part A: Applied Science and Manufacturing* **2009**, *40*, 589.

- (18) Qiu, C.; Metselaar, R. *J. Alloys Compd.* **1994**, *216*, 55.
- (19) Salamanca-Riba, L. G.; Isaacs, R. A.; LeMieux, M. C.; Wan, J.; Gaskell, K.; Jiang, Y.; Wuttig, M.; Mansour, A. N.; Rashkeev, S. N.; Kuklja, M. M.; Zavalij, P. Y.; Santiago, J. R.; Hu, L. *Adv. Funct. Mater.* **2015**, *25*, 4768.
- (20) Shugart, J. V.; Scherer, R. C.; Penn, R. L.; U.S. Patent US20120244033 A1: 2012.
- (21) Forrest, D. R.; Jasiuk, I.; Brown, L.; Joyce, P.; Mansour, A.; Salamanca-Riba, L. *Nanotech 2012* **2012**.
- (22) Brown, L.; Joyce, P.; Forrest, D.; Wolk, J. *Proceedings of the SAMPE Fall Technical Conference, Ft. Worth, TX, 17-20 October 2011* **2011**.
- (23) Nilufar, S.; Siddiqi, S.; Jasiuk, I. In *Materials Science and Technology Conference and Exhibition 2012, MS and T 2012* 2012; Vol. 1, p 701.
- (24) Jasiuk, I.; Nilufar, S.; Salamanca-Riba, L.; Isaacs, R.; Siddiqi, S. In *Technical Proceedings of the 2013 NSTI Nanotechnology Conference and Expo, NSTI-Nanotech 2013* 2013; Vol. 1, p 27.
- (25) Salamanca-Riba, L.; Isaacs, R.; Mansour, A. N.; Hall, A.; Forrest, D. R.; LeMieux, M. C.; Shugart, J. *Proceedings of Nanotech Conference and Expo 2012*. **2012**.
- (26) Jaim, H. M. I.; Isaacs, R. A.; Rashkeev, S. N.; Kuklja, M.; Cole, D. P.; LeMieux, M. C.; Jasiuk, I.; Nilufar, S.; Salamanca-Riba, L. G. *Carbon* **2016**, *107*, 56.
- (27) Jaim, H. M. I.; Cole, D. P.; Salamanca-Riba, L. G. *Carbon* **2017**, *111*, 309.
- (28) Knych, T.; Kwaśniewski, P.; Kiesiewicz, G.; Mamala, A.; Kawecki, A.; Smyrak, B. *Metallurgical and Materials Transactions B* **2014**, *45*, 1196.

- (29) Knych, T.; Kiesiewicz, G.; Kwasniewski, P.; Mamala, A.; Smyrak, B.; Kawecki, A. In *Archives of Metallurgy and Materials* 2014; Vol. 59, p 1283.
- (30) Isaacs, R. A.; Zhu, H.; Preston, C.; Mansour, A.; LeMieux, M.; Zavalij, P. Y.; Jaim, H. M. I.; Rabin, O.; Hu, L.; Salamanca-Riba, L. G. *Applied Physics Letters* **2015**, *106*, 193108.
- (31) Lim, D.-H.; Negreira, A. S.; Wilcox, J. *The Journal of Physical Chemistry C* **2011**, *115*, 8961.
- (32) Reed, J. C.; Zhu, H.; Zhu, A. Y.; Li, C.; Cubukcu, E. *Nano Lett.* **2012**, *12*, 4090.
- (33) Subramaniam, C.; Yamada, T.; Kobashi, K.; Sekiguchi, A.; Futaba, D. N.; Yumura, M.; Hata, K. *Nat. Commun.* **2013**, *4*, 2202.
- (34) Jablonski, P. D. *U.S. DOE Advanced Manufacturing Office Program Review Meeting* **2015**.
- (35) Tian, J.; Cao, H.; Wu, W.; Yu, Q.; Guisinger, N. P.; Chen, Y. P. *Nano Lett.* **2012**, *12*, 3893.
- (36) Isaacs, R. A.; Jaim, H. M. I.; Cole, D. P.; Gaskell, K.; Rabin, O.; Salamanca-Riba, L. G. *Carbon* **2017**, *122*, 336.
- (37) Wang, Y.; Jiao, M. G.; Song, W.; Wu, Z. J. *Carbon* **2017**, *114*, 393.
- (38) Cogan, S. F.; Gayle, F. W.; Klein, J. D.; Cocks, F. H.; Shepard, M. L. *Journal of Materials Science* **1978**, *13*, 2687.
- (39) Li, J.; Dang, J. *Metals* **2017**, *7*, 84.
- (40) Frankel, G. S. In *Active Protective Coatings: New-Generation Coatings for Metals*; Hughes, A. E., Mol, J. M. C., Zheludkevich, M. L., Buchheit, R. G., Eds.; Springer Netherlands: Dordrecht, 2016, p 17.



- (41) Stern, M.; Geary, A. L. *J. Electrochem. Soc.* **1957**, *104*, 56.
- (42) Burleigh, T. D.; Rennick, R. C.; Bovard, F. S. *CORROSION* **1993**, *49*, 683.
- (43) ASTM International: 2012.
- (44) Sergiienko, R.; Shibata, E.; Akase, Z.; Suwa, H.; Nakamura, T.; Shindo, D. *Materials Chemistry and Physics* **2006**, *98*, 34.
- (45) Sivasankaran, S.; Sivaprasad, K.; Narayanasamy, R.; Satyanarayana, P. V. *Materials Characterization* **2011**, *62*, 661.
- (46) Mueller, R.; Kammler, H. K.; Wegner, K.; Pratsinis, S. E. *Langmuir* **2003**, *19*, 160.
- (47) Cai, J.; Liu, R. *Energy & Fuels* **2007**, *21*, 3695.
- (48) Scari, A. d. S.; Pockszevnicki, B. C.; Landre, J.; Magalhaes, P. A. A. *Journal of Structures* **2014**, *2014*, 7.
- (49) Hansen, N. *Scripta Materialia* **2004**, *51*, 801.
- (50) Hatch, J. E.; Association, A.; Metals, A. S. *Aluminum: Properties and Physical Metallurgy*; American Society for Metals, 1984.
- (51) Skoog, D. A.; Holler, F. J.; Crouch, S. R. *Principles of instrumental analysis*; 6th ed.; Thomson: Belmont, CA, 2007.
- (52) ASTM International: 2009.